## Title
Emergent patterns in vascular networks and interaction networks: A network-centric approach for studying complex systems.

**Author**
Tekin, Elif

**Publication Date**
2017

UNIVERSITY OF CALIFORNIA

Los Angeles

# Emergent patterns in vascular networks and interaction networks: A network-centric approach for studying complex systems.

A dissertation submitted in partial satisfaction
of the requirements for the degree
Doctor of Philosophy in Biomathematics

by

Elif Tekin

2017

## ABSTRACT OF THE DISSERTATION

### Emergent patterns in vascular networks and interaction networks: A network-centric approach for studying complex systems.

by

Elif Tekin

Doctor of Philosophy in Biomathematics

University of California, Los Angeles, 2017

Professor Van Maurice Savage, Chair

Understanding how and at what scale features emerge from complex natural and social systems has presented daunting challenges for scientists and society. Nevertheless, a unifying approach that spans different systems can offer more comprehensive insights. In this respect, network science provides a common ground and a set of abstractions that has led to important advances in understanding structures, visualizing flows, and establishing predictive models for complex systems. This dissertation studies drug interactions and cardiovascular systems by modeling them as networks to identify and investigate emergent properties. Interaction-based networks play an important role in explaining the characteristics of systems that arise as collective behaviors or responses among different components. Here, we introduce a theoretical framework for the categorization of higher-order interactions built upon the conceptual understanding of net interactions (arising from effects of all levels) and emergent interactions (relative to all lower-order effects). Analyzing and dissecting drug interactions to establish this methodology, we conclude that emergent interactions are common in three-drug combinations, and we observe greater amounts of antagonism with three drugs compared to the pairwise drug combinations. This framework provides promising applications to uncover emergent phenomena into other complex systems with many interacting components such as food webs and social systems. The subsequent parts of this dissertation deal with the vascular system. In particular, we present our recent findings on pervasive asymmetry patterns in cardiovascular branching. Next, we explore the role of optimality principles as well as random branching subject to various spatial constraints from local to intermediate to global in the emergence of these asymmetric patterns. The investigation of spatial scales is important because spatial constraints have been shown to play a key role in the organization of foundationally similar systems such as the distribution of income levels across cities. Overall, this integrative approach focuses on transferring a conceptual framework and knowledge across different fields to help elucidate and predict structures, dynamics, and general behaviors in complex systems.

The dissertation of Elif Tekin is approved.

Elliot M. Landaw

Pamela J. Yeh

Tom Chou

Van Maurice Savage, Committee Chair

University of California, Los Angeles

2017

*To people I love and care...*

# Table of Contents

# List of Figures

# List of Tables

# Acknowledgments

I would like to thank my advisor Van M. Savage for his supervision and continuous support throughout my graduate studies. He always provided me the right feedback and intuition, which I found quite valuable, especially for broadening my understanding of the concepts, and contributing to come up with original ideas. He prioritized my own contributions, and gave me an immense amount of freedom to pursue my ideas. In addition to all these, Professor Savage has always been a kind, caring, and encouraging advisor. I am indebted to him for all his support and guidance throughout my career as a researcher.

I would like to thank Pamela J. Yeh for initiating the collaboration that made it possible to study collectively on exciting research problems, which turned out to be an important part of my thesis. I also would like to acknowledge the discussions with my committee members Elliot M. Landaw, and Tom Chou. I have also enjoyed our discussions with the lab members, in particular, Mauricio Cruz Loya, Daniel Wieczynski, and Tina Manzhu Kang.

Last but not least, I would like to thank my parents for their everlasting love, support and belief in me that has always helped me to walk through the adventures of my life, including the process of research and writing this thesis. I am so blessed to have them. Finally, I would like to express my sincere gratitude to my husband for being a wonderful, caring and thoughtful companion. Thank you for not giving up saying and making me say “That is going to be alright.” whenever I was going through the struggles and challenges.

# Vita

| | |
|---|---|
| 2010-2011 | E.A.P. Fellow at Mathematics Department, UCLA |
| 2011 Summer | Undergraduate Researcher, School of Engineering and Applied Sciences, Harvard University |
| 2011 Fall | Teaching Assistant, Department of Computer Engineering, Bilkent University, Turkey |
| 2012 | B.S. in Mathematics, Bilkent University, Turkey |
| 2014 Fall | Teaching Assistant, Life Sciences, UCLA |
| 2014, 2016 | Carol Newton Travel Award, UCLA |
| 2012-2016 | Research Assistant, Department of Biomathematics, UCLA |
| 2016-2017 | Research Assistant, Department of Ecology and Evolutionary Biology, UCLA |

## Publications

C. Beppler, E. Tekin, Z. Mao, C. White, C. McDiarmid, E. Vargas, J. H. Miller, V. M. Savage, P. J. Yeh, *Uncovering Emergent Interactions in Three-Way Combinations of Stressors* Journal of the Royal Society Interface 13(125) 20160800.

E. Tekin, C. Beppler, C. White, Z. Mao, V. M. Savage, P. J. Yeh, *Enhanced identification of synergistic and antagonistic emergent interactions among three or more drugs* Journal of the Royal Society Interface 13(119), 20160332.

E. Tekin, D. Hunt, M. G. Newberry, V. M. Savage, *Do vascular networks branch optimally or randomly across spatial scales?* PLOS Computational Biology 12(11) e1005223.

E. Tekin, V. M. Savage, P. J. Yeh, *Measuring higher-order drug interactions: A review of current approaches* submitted for publication.

C. Beppler, Z. Mao, E. Tekin, C. White, J. H. Miller, V. M. Savage, P. J. Yeh, *When more antibiotics kill fewer bacteria: emergent suppressive interactions in three-drug combinations* submitted for publication.

# CHAPTER 1

# Introduction and Background

Network science has cultivated the scientific knowledge of many biological and physical systems and has led to important advances in understanding structures, visualizing flows, and establishing predictive models for complex systems [1, 3, 5, 7, 15–20]. The term "network" refers to an abstract model of a set of components via nodes that are connected by links that represent direct associations between these nodes. Such abstraction and common ground has enabled the transfer of knowledge between different fields, although "network" may refer to different concepts depending on the application. Its wide range of applications include 1. gene interaction networks, where gene expression levels primarily result from series of activation or deactivation events mediated by other molecular regulators; 2. ecosystems involving many interacting species via consumer-resource relationships, pollination, and more under fluctuating environmental conditions; 3. drug interaction networks that are often used to provide efficient treatment strategies; 4. neural networks in the brain that are responsible for transmission of synaptic signals to the distant sites of the body; 5. electrical grid networks that transfer the electricity through the engineered power distribution networks; and 6. cardiovascular networks distributing the blood from heart to a whole body through a hierarchical branching network structure.

These and other different biological and physical systems of networks can be categorized based on their functionality and common characteristics. For example, networks representing the interaction between different nodes, such as genes, drugs, or species can be categorized as *interaction networks* (Fig. 1.1a). These interaction networks consist of functionally similar nodes. The exchange of information within such networks are considerably localized and emerge as whole-system behavior. Another type of networks are *flow-transmitting net-*

*works*, which circulate flow through a specialized structure, such as synaptic signals in the neural system, currents in an electrical circuit, or blood flow in the vascular system (Fig. 1.1b). These flow-transmitting networks are often called resource-distribution networks. In contrast to the interaction networks, the flow-transmitting networks are mainly responsible for delivering resources from a central source or several sources out to a whole volume and can either be tree-like or grid-like or a combination of both depending on the physical constraints. We note that the categorization of networks into these two main types is not exclusionary, meaning that some real networks can possess interactions along with some flow through its elements. As an example, the food web type networks exhibit both interactions (via interactions among species within or across different trophic levels) and flow properties (such as flow of mass or energy through trophic levels) [21–23].

Scientists have sought to understand configurations of such diverse set of networks by developing measures to describe and quantify certain structural, flow, or connectivity properties. One of the main challenges in network science is identifying ubiquitous and emergent patterns in real network structures, and whether those patterns can be explained via random formations. In regard to that, Erdös and Rényi have argued that complex networks are all randomly generated and number of links out from a node is well represented by a Poisson distribution [19, 20]. Since then, this methodology has been largely debated and with the emergence of large datasets across wide range of network types, numerous studies [18] have shown that complex systems differ significantly from the predictions attained by randomized networks. This implies that complex systems have strict organizational properties that are governed by essential and generic underlying principles. Indeed, a pairwise drug interaction study by Yeh et al. [3], Segre et al. [16] has shown that interactions are mostly monochromatic—clusters or categories of drugs all interact with other clusters in the same way—signifying a strict functional organization. Moreover, such systematic network schemes offer common advantages across different complex systems, such as resilience of the world-wide web to breakdowns [24] and robustness of damage in leaf vascular networks [25]. Altogether, network science has provided an appropriate framework and unifying approach in understanding and predicting structure and dynamics of various complex phenomena.

**Figure 1.1: Categorizations of networks.** **(a)** Schematic of interaction networks where each node represents a single component in the system and the colored edges between two nodes symbolize the pairwise interaction between them. The schematic representation is followed by examples from gene interactions [1], foodweb [2], and drug interactions [3]. **(b)** A schematic illustration of flow-transmitting networks—some form of flow is transported by the restrained physical structure—that is followed by examples of such networks: neuronal network imaged by spatial light interference microscopy [4], micro-CT image of mouse lung with the cardiovascular structure extracted by our software Angicart [5,6], and power transfer network engineered by IEEE for usage in testing power system reliability issues such as the effects of altering a single edge or node on the flows in the whole network [7].

**(a)** Interaction networks

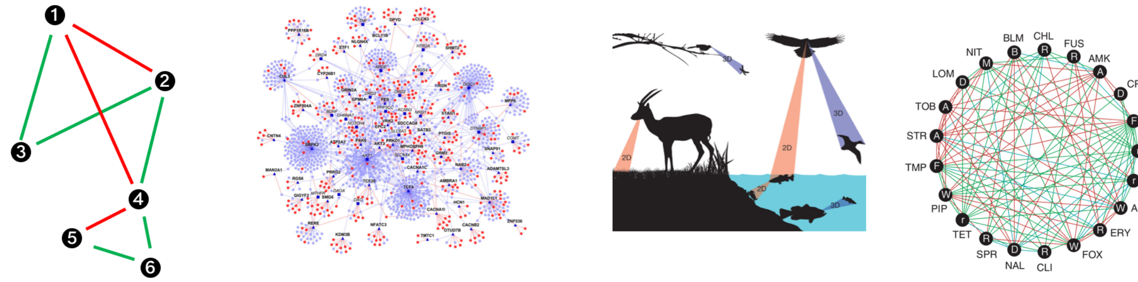

**(b)** Flow-transmitting networks

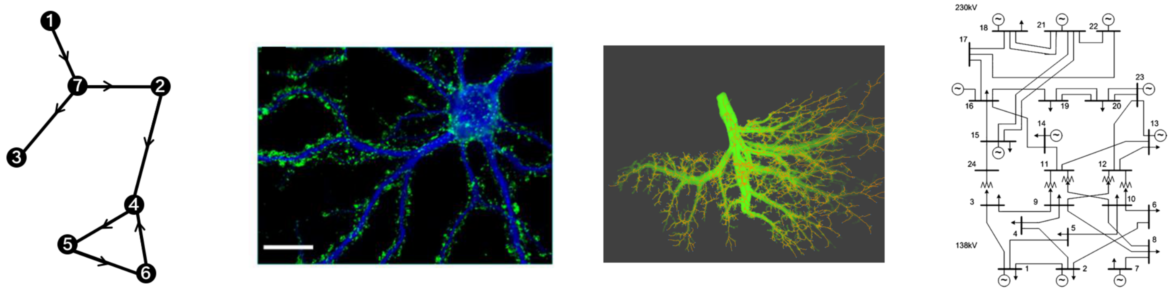

In this dissertation, our study covers one instance from two main network categories described above (Fig. 1.1), where we focus on understanding interactions and optimization properties that span different scales in terms of space, hierarchy, and number of components. In particular, we focus on multiple component interactions arising in the assessment of drug combinations for the interaction networks (Chapter 2 and 3) and the cardiovascular system for flow-transmitting networks (Chapter 4). Leveraging our knowledge on these different phenomena of drug interactions and vascular networks would potentially yield a useful scheme in delivering successful treatment strategies to inhibit and disable the tumor growth that is mainly associated with the abnormal vascularity formed to supply necessary nutrients or oxygen to the tumor site.

This study has been published in three papers, namely "Uncovering emergent interactions in three-way combinations of stressors" [26], "Enhanced identification of synergistic and antagonistic emergent interactions among three or more drugs" [27], both published in *The Journal of Royal Society Interface*, and "Do vascular networks branch optimally or randomly across spatial scales" [6] published in *Public Library of Science Computational Biology*. Chapters 2, 3 and 4 are entirely formed by these papers, each corresponding to the respective chapters. Note that some material from these papers are also incorporated into Chapter 1 and 5 and the supplementary materials referenced in this dissertation can be retrieved through online access of these articles.

## 1.1 Drug Interaction Networks and Multiple Component Interactions

Because of their key role in understanding the dynamics of important biological systems (e.g., cell cycles, food webs), interactions have been extensively studied over time and in a wide range of organisms [28–35]. In this regard, many methods have been developed for defining and categorizing interactions into different classes [28, 29]. In a broad context, for a complex system involving multiple stressors, interactions are determined based on the response phenotypes that can be measured both separately and in combination for each component. For example, in the drug interaction framework where drugs induce stress on the pathogen proliferation, growth rates (or fitnesses) of pathogen exposed to combinations of drugs represent the response phenotype. In a different biological interaction network, such as predator-prey systems, where a certain prey population is encountered with multiple predators, the response phenotype is given by the mortality and consumption rates of prey eaten by combinations of multiple predators. In another ecological setting, physiological rates affected by combinations of ecological stressors can be defined as a response variable. For these and other examples of interaction networks, phenotype measured in response to single and combined effects accompanied with an appropriate interaction classification method provides assessment of interactions between components. Moreover, due to the basic and foundational similarities, the concepts and measures developed for one setting can often be translated and employed into other interaction-based networks (see Chapter 2 and Appendix A).

In general, interactions are classified relative to the case that the single components do not interact at all, hence they are additive. Assignment of interaction types into categories of positive (synergistic) or negative (antagonistic) interactions are determined based on the deviations from this no-interaction (or additive) case. Despite the fact that complex systems involving many components have the potential for higher-order interactions, previous studies have primarily focused on two-way or pairwise interactions. This pairwise approach can cause oversimplification, hence resulting in potentially misleading results when predicting the overall behavior of the complex system. Therefore, a novel approach to identify interactions resulting from different levels of interaction is required to obtain more comprehensive insights into the complex systems research. This raises questions such as: Can we characterize higher-order, emergent interactions that are not predictable from lower-order components? How do emergent interactions differ from the overall, net interaction? Are emergent interactions common in nature? Can we observe patterns in terms of frequencies of emergent interactions or synergism versus antagonism of higher-order interactions?

### 1.1.1 Characterization of two-way (pairwise) drug interactions

In this dissertation, we use an experimental system of the bacteria *E. coli* exposed to different drug combinations as a model system to investigate these basic yet subtle questions about complex, higher-order interaction effects. In the drug interaction framework, the effectiveness of drug therapies is typically determined by a drug's capability of inhibiting the pathogen's growth. Legitimately, the exploration of how drugs affect one another requires measurements of pathogen growth rates in response to single and combined effects of drugs relative to growth in the absence of drugs. This is commonly referred as relative fitness and denoted as $w_D$ for drug combination $D$ and takes values between 0 and 1, corresponding respectively to no-growth (best treatment) and maximum (worst treatment) pathogen growth. In this manner, one can examine drug interactions either at the fixed concentrations for each of the drugs, or across a gradient of concentrations of the combined drugs, where each strategy has its own benefits or caveats. In particular, evaluating drug interactions at fixed concentrations is simple and straightforward, whereas examining drug interactions across different concentrations is burdensome as it requires prohibitive amounts of work to collect a sufficient amount of data but it provides more comprehensive information on analyzing drug interactions.

For pairwise (i.e., two-drug) combinations, there are two common methods to measure and categorize interactions corresponding to each scheme: Bliss Independence [28] and Loewe Additivity [29]. These methods quantitatively define the case of no interaction between two drugs and categorize the interaction type based on the magnitude and direction of deviations from the non-interacting (additive) case. The interaction is referred as synergistic and antagonistic when drugs together are more or less effective than their additive effect, respectively. Moreover, it is also possible to define special cases of synergistic and antagonistic interactions. For example, lethal synergy where the synergistic interaction causes the complete inhibition of the pathogen population represents a special case and defines a relative case for defining the interaction strength [3, 16]. Antagonistic interactions constitute two special cases where one represents a buffering effect, meaning that one drug completely obscure the potency of the other drug. Second, suppression is defined as when the antagonistic effect is even stronger than the buffering scenario, not just masking but actually reversing some of the potency of the other drug [36, 37]. The most suppressive case can be observed when the pathogen growth is fully recovered as there is no drug at all. Importantly, identification of interaction types with these subcategorizations can provide more information about interactions and can be achieved by normalizing the basic metrics as explained below. Now, we review measures introduced for the identification of two-drug interactions.

First, Bliss Independence characterizes drug interactions when drugs are combined at fixed concentrations. It defines additivity such that the percent decrease in the relative fitness of the pathogen when treated with one drug is not impacted by the presence of another drug at previously determined concentrations. Here, individual drug concentrations are typically chosen such that they reduce the pathogen growth to a range of 65-90% as compared to the no-drug (wild type: WT) case. In mathematical terms, the additivity between drugs $X$ and $Y$ corresponds to the relation $w_{XY} = w_X w_Y$ [28]. For example, if drugs $X$ and $Y$ yield fitness measurements of 0.5 each, meaning that they both inhibited the growth by 50%, then it is expected that the combination of drugs $XY$ inhibits the growth by 75% as $w_{XY} = 0.5 * 0.5 = 0.25 = 1 - 0.75$ under the null hypothesis that drugs are not interacting [37]. Note that assuming drug $X$ is additive with itself by Bliss (i.e., $w_{XX} = w_X w_X$) places specific constraints on the fitness measure as a function of drug $X$ concentration. This assumption is empirically verified for many of the antibiotics discussed in this thesis (see Chapter 2.2). By definition, the deviation from additivity (DA) determines the interaction between drugs given by

$$\mathrm{DA}_{X,Y} = w_{XY} - w_X w_Y \tag{1.1.1}$$

Consequently, when this measure is greater than 0 corresponding to the case that the combined effect ($w_{XY}$) is greater than the expectation based on the independent single drug effects ($w_X w_Y$), then it implies synergistically interacting drugs. In contrast, the opposite case implies antagonism between drugs $X$ and $Y$.

An additional challenge for the classification of combination effects is that the existence of interactions is not apparent due to the unimodal form of raw interaction values (DA results) based on empirical data [3, 16]. The definition suggests that the sign of the DA measure can be easily interpreted as drugs are either enhancing or diminishing the effects of each other, however, the magnitude of the interaction is not well represented by the DA measure. Hence, the raw form of the interaction metric leads to a unimodal distribution around 0 (additivity) that does not clearly define boundaries between different interaction types (synergy, additive, antagonism) [3, 16]. Therefore, a refinement of the interaction metric is necessary to evaluate for the actual magnitude of the interaction and thus to make the identification of interactions more accurate. Such a refinement may require rescaling (a normalization) based on the special cases of synergy and antagonism. This ambiguity can be easily seen by the following examples showing that drug combinations with different interaction strengths (such as weak versus strong antagonism) can map onto an identical interaction metric (DA) values. Consequently, interactions specified based on the current form of DA may not be reliable. Now, consider two different drug combination profiles leading to same DA calculation (Fig. 1.2a): i) When single drug fitnesses are given as $w_X = 0.54$, $w_Y = 0.91$, and the double drug fitness is given as $w_{XY} = 0.54$, or ii) setting $w_X = w_Y = 0.7$, and $w_{XY} = 0.54$ yield same DA values (= 0.05). There are two conclusions based on this example along with the same lines of the above arguments. First, it is clear from the fitness values that the pairwise interaction is antagonistic buffering for the first $XY$ combination, however based on the DA calculation, one can conclude that there is no interaction between $X$ and $Y$ since 0.05 is very close to the base line of no-interaction (i.e. DA = 0). Next, the first scenario shows stronger antagonistic behavior than the second one, however, there is no way to distinguish them by inferring conclusions merely based on the raw interaction values as they are identical across these two different instances. A similar example for negative DA values is given in Fig. 1.2a denoted as cases (iii) and (iv), confirming inconsistencies in defining the drug interactions when the DA measure is applied. Consequently, the small white bars—one on the top of other—at the schematic of DA distribution represents cases that need to be distinguished (Fig. 1.2a). Therefore, it is crucial to devise a revision to the

**Figure 1.2: Effect of rescaling the pairwise interaction measure (DA) on the frequency distribution.** **(a)** Unimodal distribution of DA does not result in clear cut-off values, hence does not yield precise regions for distinguishing additive, synergistic, and antagonistic interactions. In addition, it does not help differentiate cases that yield identical interaction values but show distinct interaction behaviors as shown by comparisons of (i) and (ii), as well as (iii) and (iv). **(b)** Rescaled DA measure successfully delineates boundaries and tease apart synergistic, additive and antagonistic interactions via the resulting trimodal distribution with peaks around $-1$ (lethal synergy), 0 (additivity), and 1 (antagonistic buffering). The new rescaled interaction metric also separates case (i) from (ii) and case (iii) from (iv), and hence reveals the actual magnitude of interaction and correctly identifies the interaction type corresponding to each of the four cases.

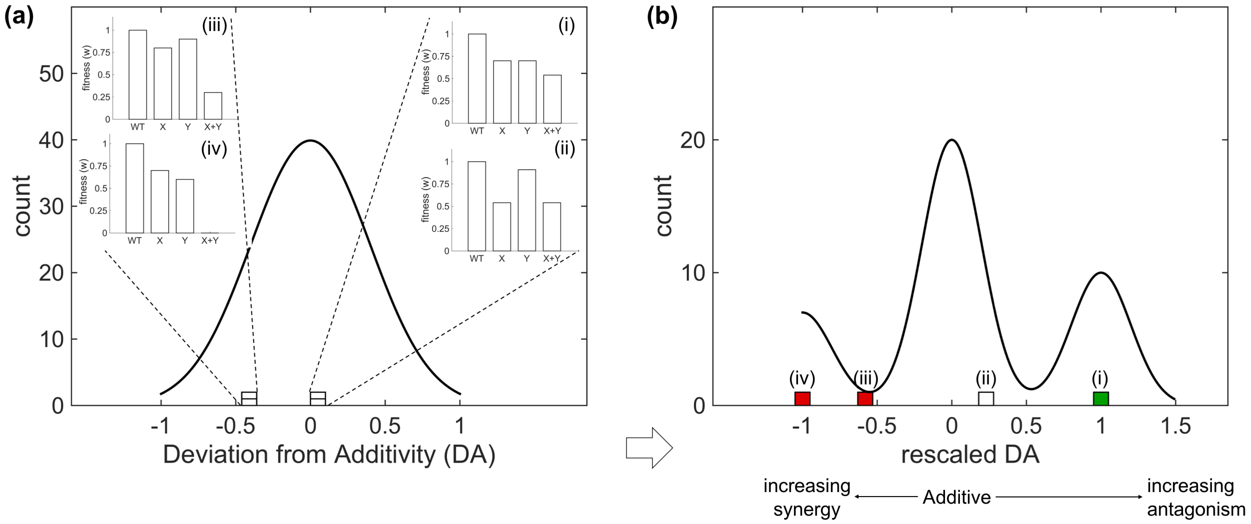

interaction metric that eventually provides enhanced identification of interactions.

In regards to this, previous studies on two-way interactions [3,16] have shown that applying a rescaling method to the pairwise interaction measure (DA) enhances the classification of synergies and antagonisms. Two reference cases are taken as a basis for the two-drug rescaling corresponding to negative and positive values of DA: 1) lethal synergy meaning that the combined effect deteriorates the pathogen growth at a full capacity ($w_{XY} = 0$), 2) complete buffering indicating that the combined effect is the same as the strongest individual effect ($w_{XY} = \min(w_X, w_Y)$). This rescaled DA measure yields a tri-modal distribution with peaks at these reference cases (see a schematic representation of rescaling in Fig. 1.2b) leading to a clear separation among synergistic, antagonistic, and additive interactions [3, 16]. For the above cases of (i) and (ii) provided to exemplify the necessity of improvement in the classification of interactions, the rescaled DA metric successfully distinguish the interaction types as the calculation yields 0.23 in case (i), and 1 in case (ii), where one of the drugs buffers the effect of the other drug in the pairwise combination. The similar conclusion is achieved for cases (iii) and (iv) with negative DA values since the degree of interactions is reflected by the new rescaled metric.

Overall, Bliss Independence—or equivalently the DA measure—offers a feasible way to classify interactions and has been applied to a wide range of diseases to determine the drug combination potency, including bacterial infections [3, 13, 37–42], fungal diseases [43–48], types of cancer [49–54], HIV [55–59], and plant diseases [60, 61]. Moreover, gene epistasis studies directly and reliably measure the interactions in terms of DA by using growth rates of single and double knockout mutants as the fitness parameters [16, 62–66] .

On the other hand, Loewe additivity [29, 37] characterizes the interaction based on the growth response of pathogen (i.e. the relative fitness $w_D$) to a range of drug concentrations that are varied simultaneously. In that respect, drugs are defined as additive (non-interacting) if the total inhibitory concentration of the combination—the sum of individual drug concentrations relative to each drug's Minimum Inhibitory Concentration (MIC)—is independent of the relative fractions of each drug. A natural example follows from combining a drug with itself, where any fraction of MIC (say $c = 0.75$) of the drug would be complemented by the ($1 - c = 0.25$) MIC of the same drug, meaning that the drug is additive with itself. Rephrasing this statement in terms of two different drugs with the given fraction of MIC of the drug $X$, one can infer that if the drug $X$ is complemented by the 0.25 MIC of another drug $Y$, then $X$ and $Y$ are additive. For any value of c, this is equivalent to saying that drugs do not interact when the combination of drug $X$ at a concentration $C_X = c * C_{X,\mathrm{MIC}}$ with the drug $Y$ at a concentration $C_Y = (1 - c) * C_{Y,\ \mathrm{MIC}}$ yields full inhibition of the growth. Thus, the additive relation by Loewe measure corresponds to the expression

$$\frac{C_X}{C_{X,\mathrm{MIC}}} + \frac{C_Y}{C_{Y,\mathrm{MIC}}} = 1 \tag{1.1.2}$$

where the effective concentration terms correspond to the normalized concentration of $X$ and

$Y$ relative to their MIC, respectively. Thus, two drugs are additive if the inhibitory effect is attained along a straight line in concentration space defined by the equation above (Fig. 1.3). On the contrary, if the normalized curve at the inhibitory level (isobologram) is concave, this implies that a lower effective concentration is enough to inhibit the pathogen, and the drug interaction is recognized as synergistic. Finally, a convex MIC profile for a drug combination corresponds to an antagonistic interaction because it indicates that increased drug dosage is needed to achieve the full pathogen inhibition. Note that the interaction between drugs can be defined analogously for other response levels that is different than the inhibitory profile of the pathogen. This can be done by simply normalizing the concentrations relative to concentrations producing the bacterial inhibition at the level of interest. As an example, one can determine drug interactions at 50% inhibition of pathogen ($IC_{50}$) by analyzing the isobologram at this level, where the MIC terms in the Loewe equation for additivity are simply replaced by the $IC_{50}$ terms for each drug.

### 1.1.2 Higher-order drug interactions

Despite the fact that higher-order drug combinations are becoming more prevalent in the clinic such as recent therapies for treating patients with complex diseases such as HIV [67] or *Mycobacterium tuberculosis* infections [68], a rigorous understanding of how to quantify and characterize higher-order drug interactions has not yet been fully achieved. This is mainly because several difficulties arise when the complexity of the system increases—such as going from two-drug interactions to three-drug combinations. First, for the simplest case where there are only two drugs in the environment, only two-way interaction relative to the single drug effects can be observed. However, when there are more than two drugs in the system, any lower-order mixture of drugs can have an effect on the higher-order drug interaction (Fig. 1.4). This brings out a possibility that an $N$-way interaction may come from an interaction of just some subset of the drugs in the combination. For example, a synergistic three-way interaction may solely arise from a synergy of just two of the drugs, hence would not be a novel therapeutic option. Indeed, in such a case, the third drug could be irrelevant in terms of pathogen killing, and thus likely should not be used to decrease the toxic side effects to

**Figure 1.3: Loewe Additivity.** *Adapted from Chait et al. 2007* [8]. Lines of equal bacterial response (growth) profile with drug combinations are shown in the right panel. Loewe classifies drugs $X$ and $Y$ as additive if their combined effect is identical to the linear effect from the two individual drug outcomes (i.e. when Eq. (1.1.2) is satisfied) as represented by the dash-dotted curve. When the isobole at the level of interest shows downward (concave) deviation from the linear behavior, then drugs are synergistic. On the contrary, antagonistic drug pairs are identified by the upward deviation from the additivity line as they show weaker effect together (dotted curve). The extreme form of antagonism is shown by the solid curve.

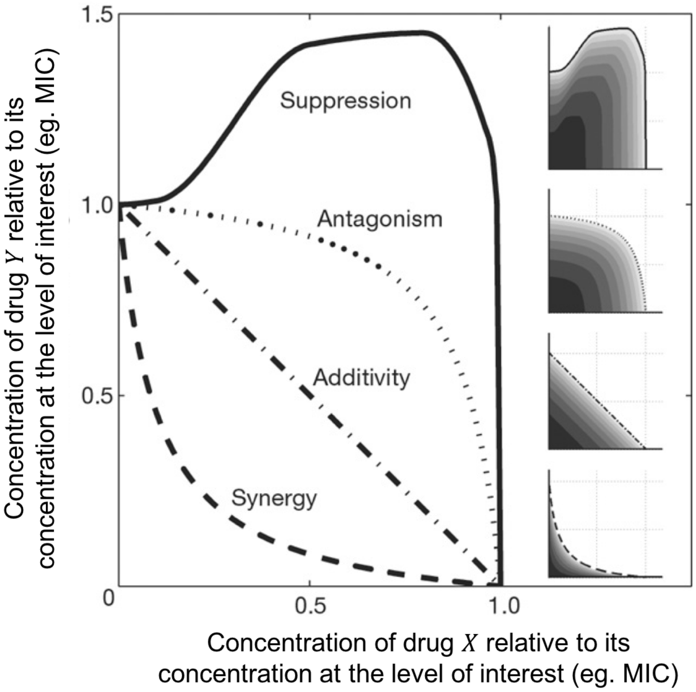

**Figure 1.4: Conceptual and experimental framework for testing $N$-drug interactions.** When $N = 2$, a pairwise interaction is the only type of interaction that one can observe. To test for pairwise interactions, we need pathogen response measurements in the presence of each single drug alone and the pairwise combination of drugs. On the other hand, when there are three components in the system ($N = 3$), there are two different categorizations of interactions: 1. net interaction defined as the total interaction resulting from all the lower-order effects; 2. emergent interaction defined as the higher-order effects that are not predictable from the lower-order interactions. To quantify three-way interactions, pathogen response measurements for all possible subsets of drug combinations are required.

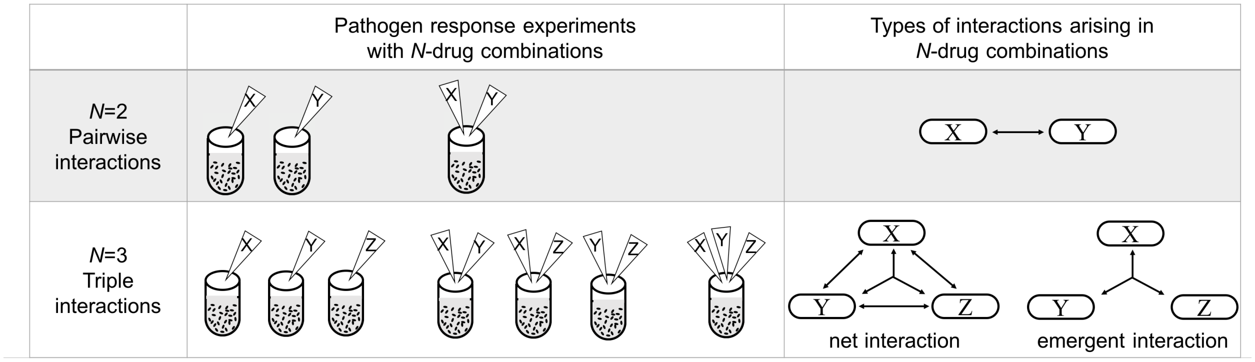

the patient that might arise from the addition of ineffective third drug. On the other hand, an emergent three-way interaction represents a truly novel effect that could potentially be an excellent therapeutic option. Therefore, it is crucial to distinguish net—arising from effects of all levels—and emergent interactions—that only emerge when all drugs are present—by developing a rigorous and explicit conceptual and theoretical framework. There have been attempts to extend the mathematical framework introduced for pairwise drug interactions—Bliss Independence and Loewe Additivity—to higher-order combinations as done by Sanjuan et al. [62,69], Otto-Hanson et al. [61], Berenbaum et al. [70]. However, these previous studies do not give information about emergent behavior as those measures merely compare the $N$-drug combo effect with the single-drug effects. Such an approach without the consideration of other lower-order effects fails to fully grasp higher-order interactions. Thus, establishing a measure to quantify emergent interactions requires more thought.

Next, as in the case of two-drug interactions, higher-order interaction metric should also be accompanied with an appropriate rescaling method to reflect the magnitude of the interaction and to provide a clear distinction among different interaction types. This is a crucial step as interactions may be missed if the unscaled metric results are used to infer the interaction type. On the other hand, defining rescaling methods for higher-order interactions adds an extra layer of difficulty as there may be several choices of baselines for the rescaling when there are more than two drugs. In particular, it is important to address whether antagonistic buffering mean three-drug effect is equal to the strongest individual (as done in Sanjuan et al. [62]), or to couple, or interaction effect due to two interacting drugs.

Finally, to distinguish the lower-order effects from the $N$-drug interaction, one should obtain pathogen response measurements in the presence of all possible subsets of drug combinations. For example, quantifying emergent three-way interaction among drugs $X$, $Y$, and $Z$ requires 8 relative fitness measurements—for all singles $(w_X, w_Y, w_Z)$, all doubles $(w_{XY}, w_{XZ}, w_{YZ})$, and a triple $(w_{XYZ})$—whereas an assessment of pairwise drug interaction requires only 3 measurements per drug combo (Fig. 1.4). When the number of drugs tested for higher-order combinations $(K)$ increases, the total number of measurements $(\mathrm{E}_{\mathrm{total}})$ necessary to quantify $N$-drug interactions increases as well, given by $\mathrm{E}_{\mathrm{total}} = \sum_{i=1}^{N} \binom{K}{i}$ , resulting in increasing experimental complexity. In other words, collecting this extensive amount of detailed data requires putting a substantial effort into performing experiments, which may not always be feasible. Note that all the concepts and issues raised here on higher-order (three or more) drug interactions are applicable to higher-order interactions in other complex systems.

Recent studies on higher-order drug interactions have made significant contributions toward examining interactions that are beyond the pairwise effects. Particularly, a recent study by Wood et al. [13] employed maximum entropy method to quantify three-way interactions that could not be predicted from two-way interactions. Using six triple-antibiotic combinations that are varied across different concentrations, they recognized that their maximum entropy method result in similar conclusions when a simple algebraic formula, known as Isserlis theorem, is utilized. Then, they suggested that Isserlis formula can be used to determine higher-order effects beyond pairwise combination effects. Note, however, that when there are more than three components in the system, one should distinguish the higher-order effects from effects from all lower-order combinations not just from pairwise combinations.

Another study by Zimmer et al. [71] used a mathematical framework by applying Bliss Independence to growth curves defined by Hill functions at the effective dosages of drugs, which are determined based on the pairwise interactions with other drugs in the combination. The studies reviewed here (i.e. Wood et al. [13] and Zimmer et al. [71]) both concluded that for most of the cases pairwise combinations are sufficient to identify the higher-order effects, meaning that there is no emergent interaction.

In studies of multi-way stressor interactions, especially predator-prey systems and sometimes epistasis, full factorial design of ANOVA has been used to infer higher-order interactions between stressors [30,72,73]. For instance, Chen and colleagues analyzed effects of three stressors on zooplankton and amphibians using three-way ANOVA [73]. However, ANOVA has a few limitations that are related with the above points raised about the identification of higher-order interactions [74]. First, ANOVA only identifies the existence of an interaction, but does not yield an indication of the direction or a classification as synergy or antagonism. Second, it is unclear how to rescale a three-way ANOVA, making it more challenging to identify interactions [16]. Third, ANOVA tests for significance by comparing variances that assume Gaussian or parametric distributions, which require significant amounts of data for each response variable in the system (singles, doubles, triples etc.), which does not exist in the literature to the best of our knowledge. Finally, pseudo-variance argument (or commonly referred as hidden replication)—used to provide statistical power even with a limited replication—only works when there is no interaction, which is not necessarily true and would not be a reasonable assumption as we aim for identifying a deviation from the no-interaction scenario [75]. All these potential shortcomings about ANOVA that is frequently used in multi-stressor interaction studies should be reviewed in depth and the framework of ANOVA should be further contrasted with other interaction-classification methods analytically and conceptually.

In this dissertation, we study multiple-drug interactions at fixed concentrations—as in the definition of Bliss Independence [28]—where the experimental data consists of growth rates of bacteria in all single, pairwise, and triple combinations of antibiotics, allowing a setup with the necessary information for the characterization of three-way interactions. In doing so, we use an interaction metric by extending Bliss Independence (DA) to bacterial systems exposed to more than 2 drugs to quantify whether any net interaction exists at all relative to the single-component effects. Importantly, we develop a novel and highly informative interaction metric (E3) that quantifies whether there are three-way interactions beyond what is expected from the effects of all pairwise combinations. This is done by building up from the definition of Bliss Independence for drugs in a way that properly weights and subtracts off the pairwise predictions from the net interaction. In that respect, in Chapter 2, we introduce a framework that uncovers emergent three-way interactions by deriving a conceptually clear and computationally straightforward framework with no free parameters. Along with the derivation of 3-way interaction measures, we also establish a generalization of our interaction metrics to systems with four or five components. In short, our DA and E3 measures effectively distinguish between net and emergent interactions, and are derived starting from the definition of no-interaction, and are also easily calculable.

As in the case of two-way interactions, the higher-order interaction metrics also require adapting an appropriate rescaling method to clearly delineate and distinguish the types of interactions. However, adapting the rescaling method established for pairwise interactions to three or more drugs requires a more thorough assessment. In particular, we need to address whether the baselines of synergy or antagonism differ when there are more than two drugs, e.g. whether antagonistic buffering means the three-drug effect is equal to the strongest individual effect, stronger pairwise drug effect, or the interaction effect due to two interacting drugs that combine information from single-drug effects and pairwise interactions? Therefore, in Chapter 3, by taking our conceptual and theoretical framework as a baseline, we propose and test several rescaling methodologies for enhancing the classification of higher-order interactions. Using these new rescaling methods to examine the triple-drug data, we demonstrate that there are many more higher-order emergent interactions than previously identified [13, 71]. By choosing an appropriate rescaling approach and applying it to extensive data from our model system, we see that our new interaction metric accompanied with a more effective rescaling can successfully identify and distinguish among different categories of interactions. Finally, we conclude that emergent interactions are common in three-drug combinations, and we observe greater amounts of antagonism compared to the pairwise drug combinations.

In Appendix A of this dissertation, we also provide a comprehensive review to assess differences between the standard statistical method ANOVA and our drug interaction framework based methods—rescaled Deviation from Additivity (DA) and Emergent Three-way Interaction (E3) metrics. In particular, we present mathematical translation of standard two-way and three-way ANOVA into a measure and recognize that ANOVA applied to the log transformed data for three-way combinations gives conceptually closer terms with our emergent interaction metric (E3). Then, we perform a three-way ANOVA to our drug combination data in both linear and log space, and determined how well our model results and ANOVA results match (Chapter 2).

As presented above, the interaction-based networks (Fig. 1.1a) are one network type that is covered in this dissertation. For that, the following 2 chapters establish a coherent theory for the characterization of higher-order interactions via an experimental system of bacteria exposed to multiple drug combinations. In these chapters, we have also included a discussion of the existing models of interaction categorizations, and contrasted with our framework. As we study different network types, the rest of this chapter introduces the proper background needed to understand our study of the cardiovascular system as an instance of the second category of networks, i.e. flow-transmitting networks (Fig. 1.1b).

## 1.2 Flow-transmitting Cardiovascular Network

It is of a great scientific interest to study the cardiovascular network for understanding how it distributes the resources and oxygen throughout the body, investigating its role in the metabolic activities, and revealing patterns in the structural organization of the network. All these inquiries about the cardiovascular system are relevant in explaining and predicting the empirical observations that metabolic rate ($B$) scales approximately as the 3/4 power of the body mass ($M$),

$$B \propto M^{\frac{3}{4}} \tag{1.2.1}$$

**Figure 1.5: Metabolic rate and body mass relationship.** **(a)** *Adapted from Hemmingsen et al. 1960* [9] Empirical evidence showing that metabolic rate and body mass are related as a power-law with an exponent equal to 3/4. **(b)** *Adapted from Kolokoktrones et al. 2010* [10]. Second-order curvature is detected by an extensive amount of recent data suggesting that the relationship between metabolic rate and body mass is a power-law to leading-order but has a significant and measurable second-order curvature.

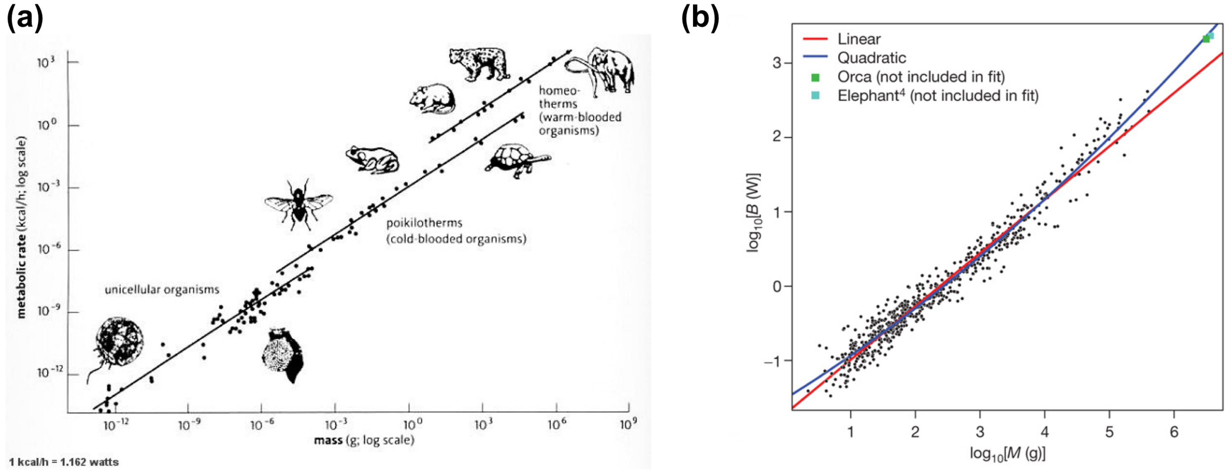

This canonical 3/4 value was first observed by Kleiber in 1947 [76] based on data from 13 animal species and later termed as metabolic scaling theory or allometric scaling law since it is preserved as body shapes change with size [11, 77–79]. Eq. (1.2.1) can equivalently be expressed by a line with a slope of 3/4 in log-log space (Fig. 1.5a). Recent theories for the cardiovascular system [79–83] that rely on series of assumptions about its structure and flow properties have ultimately been able to predict this power-law relationship between metabolic rate and the body mass.

Specifically, West, Brown, and Enquist (WBE Model [79]) modeled the vascular system as a hierarchical branching structure constrained by several physical and biological principles. Here, the hierarchy of the vascular network is represented by a successive arrangement of branching vessels that start from the main vessel, i.e. heart. Therefore, in this model the branching levels are computed as the hierarchical distance (Fig. 1.6)—defined as the number of branching junctions away from the heart (level 0). An alternative labeling scheme introduced by Horton-Strahler [84, 85] computes the branching degree starting from the most downstream branch of the network, i.e. the capillaries. When proceeding from one branching level to the next, Horton-Strahler increments the labeling by 1 (such as $k$ to

$k+1$) if the vessel has two or more children that are labeled by Horton-Strahler number $k$. Otherwise, (i.e. if one child is labeled as $k$, but all other children are labeled less than $k$) the Horton-Strahler number for the current vessel stays at $k$. This essentially means that Horton-Strahler assigns higher values to branches with larger number of downstream vessels in the network, whereas such distinction is not apparent in the case of the hierarchical ordering of vessels. Labeling of the vessel based on some metric distance to the most upstream vessel has provided a computational framework for the study of hierarchical branching networks including the cardiovascular system.

WBE assume that the vascular network is symmetric in the sense that sibling vessels, as defined by flow coming into them from a shared upstream parent vessel, are identical in terms of their structural and flow properties such as radius, length, flow rate, and pressure [11,79]. Next, from the observation of fractal-like structures—pattern that is held across large and small scales—in the cardiovascular system, WBE assume a constant value for the number of vessels branching out from a single parent vessel, which is called the branching ratio, $n$. Here, self-similarity is a direct consequence of the fractal assumption and suggests scale-free properties in the branching structure that are characterized by power-law relationships. Assuming that vessels within the same level of the hierarchy are identical leads to a characterization of the overall network structure via the length and radius ratios between parent and daughter vessels, which are commonly referred to as scaling ratios$\beta_k$ and $\gamma_k$

$$\beta_k = \frac{r_{k+1}}{r_k} = n^{-a_k}, \qquad \gamma_k = \frac{l_{k+1}}{l_k} = n^{-b_k} \tag{1.2.2}$$

with the scaling exponents $a_k$ and $b_k$ [11, 79]. Again, the self-similarity of the branching network may indeed yield level-independent scaling ratios or equivalently scaling exponents as it means that the properties are conserved across all branching generations. In that case, we can simply drop the subscript for these parameters, and use the generic scale-free ratios $\beta$, $\gamma$, and exponents $a$, $b$. That is, at any location of the network, the scaling relationships between parent vessel to their daughter vessels remain constant and characterized by a power-law relationship with the branching ratio $n$.

**Figure 1.6: Symmetrical vessel branching and labeling schematic for bifurcating network.** *Adapted from Savage et al. 2008* [11]. A parent vessel at level $k$ with radius $r_k$ and length $l_k$ branches into two identical daughter vessels with radius $r_{k+1}$ and length $l_{k+1}$. Branching level starts at 0 at the heart and successively increases by 1 as the vascular system branches into the next level.

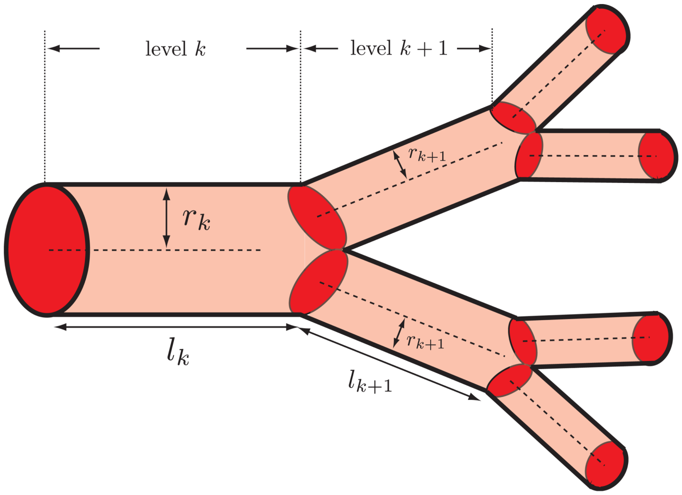

Imposing several more assumptions on the vascular system has eventually led to the predictions of radius and length scaling exponents. Essentially, WBE posit that to deliver blood to all the cells at the capillary level, the network should have a space-filling geometry, meaning that capillaries must be close enough to all cells to supply them with oxygen, and branching levels upstream from the capillaries must be distributed in such a way to allow downstream vessels like the capillaries to span the body [11,86]. This latter part implies the total volume serviced is conserved from one level to the next. Denoting the service volume of a vessel at level $k$ by $v_k$ and the number of vessels at a level $k$ by $N_k$ ($= n^k$, where n represents the branching ratio for a network), the space-filling property of the network can be expressed as $v_{net} := N_k v_k$ for all $k$. Thus, service volume ratio between the parent and child vessels (i.e. $v_{k+1}/v_k$) are simply given by $N_k/N_{k+1} = n^{-1}$. Now, the main question is how the volume serviced by each vessel is related to their vessel size. Specifically, what is the geometry of the volume serviced, and how do its dimensions depend on the radius and length of the vessels, and does this change across hierarchical levels of the network? In regards to this, WBE assume the service volume of a vessel is related to the volume of a sphere with a diameter proportional to the length of the vessel, hence the service volume for

**Figure 1.7: Illustration of space-filling in two dimensions.** *Adapted from Etienne et al. 2006* [12]. The total service volume at level $k$ defined by circles with the diameter equal to the length of the vessels is conserved at the next branching level $k+1$. ($k = 4$ in the figure). In three dimensions, service volumes are defined by spheres, hence total service volume at level $k$ is given by $N_k l_k^3$.

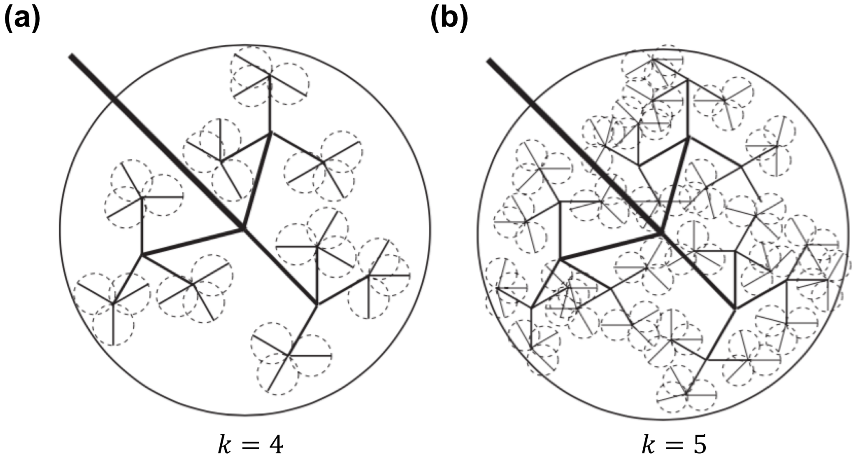

a vessel at level $k$ can be written as $v_k \propto {l_k}^3$ (Fig. 1.7). Substituting this into Eq. (1.2.2) leads to a length-scaling exponent ($b$) that is independent of level $k$

$$\gamma = \frac{l_{k+1}}{l_k} = \left(\frac{N_k}{N_{k+1}}\right)^{1/3} = n^{-1/3} \tag{1.2.3}$$

Next, the minimization of power-loss for the blood flow leads to a radius ratio that is independent of level $k$ but depends on two regions corresponding to large and small vessels [11, 79]. This is because power loss is dominated by different processes based on the size of the vessel radius. First, blood flow through large vessels exhibits pulsatile flow with an elastic wall and boundary, so the flow and pressure generate wave reflections at the branching junctions that ultimately cause power loss. Hence, minimizing the power loss due to the wave reflections is simply done by setting the pressure of the wave reflection at a branching point equal to zero. Eliminating wave reflections leads to impedance matching of pulsatile flow [87, 88]—where the impedance ($Z$) is inversely proportional with the square of the vessel radius [87]—in successive branching levels. Consequently, applying impedance matching at a branching junction from level $k$ to $k+1$, hence compensating for the impedance of a parent vessel at level $k$ with the total impedance coming from the n parallel daughter vessels at level $k+1$, yields a radius scaling ratio in the case of large vessels as

$$\beta^{>} = \frac{r_{k+1}}{r_k} = \left(\frac{N_k}{N_{k+1}}\right)^{1/2} = n^{-1/2} \tag{1.2.4}$$

[11, 79]. In other words, the cross-sectional area of a parent vessel ($\pi r_k^2$) is equal to the sum of the cross-sectional area of its daughter vessels ($n\pi r_k^2$), so large vessels can be described as area-preserving vessels, which is also known as Da Vinci's rule.

In contrast, power dissipation through vessels with small radius is largely dominated by viscous forces between the blood and vessel walls that cannot be eliminated. To minimize power loss—given by $\dot{Q}_0^{\,2} Z_{net}$ where $\dot{Q}_0$ is the blood volume flow rate and $Z_{net}$ is the total impedance of the blood—the method of Lagrange multipliers is implemented under three constraints that the network is: (i) of fixed size, (ii) contained within a fixed body mass, and (iii) space-filling [11, 79]. Assuming incompressible laminar flow, i.e. Poiseuille flow, results in

$$\beta^{<} = \frac{r_{k+1}}{r_k} = \left(\frac{N_k}{N_{k+1}}\right)^{1/3} = n^{-1/3} \tag{1.2.5}$$

or equivalently $r_k^3 = \sum r_{k+1}^3$. In contrast to the pulsatile flow regime, this last equation states that the total cross-sectional area of daughter vessels exceeds the cross-sectional area of their parent vessel, so vessels with this property have been referred to as area-increasing. The notion of relating the parent vessel radius as a sum of cubic powers of daughter vessel radii was first introduced by Murray [89] through an optimization scheme at a local branching junction based on two assumptions: (i) fluid is conserved at a branching junction and (ii) the sum of the power loss of blood flow and the power cost of the blood volume for a single vessel are jointly minimized. Overall, these two flow regimes (pulsatile and dissipation) characterize the dominant form of the radius scaling exponents where $a = 1/2$ for large vessels and $a = 1/3$ for small vessels [11, 79].

Now, to relate metabolic rate with the body mass, WBE make the following two observations. First, under the assumption that capillaries are the only units of the network responsible for exchanging materials, one can simply write the total metabolic rate as $B = N_{cap}B_{cap}$, where $N_{cap}$ denotes number of capillaries, and $B_{cap}$ denotes the metabolic rate of a single capillary. Assuming identical anatomical and physiological capillary characteristics across different organisms and species, such as invariance of capillary length, radius, and metabolic rate ($B_{cap}$) for the capillary, then whole-body metabolic rate is proportional to the number of capillaries of an organism, i.e. $B \propto N_{cap}$. Next, as blood vessels fill the body, body mass is proportional to total blood volume [11], so $M \propto V_{net}$. By these proportionality relations, arriving at a general relationship between the metabolic rate and body mass is equivalent to attaining a mathematical formula describing how number of capillaries and total volume of the network are related. Here, the invariance of capillary characteristics allows the capillary level to serve as a reference unit that sets the scale in the derivation of $V_{net}$ (or equivalently $M$) as a function of number of capillaries, hence a function of metabolic rate ($B$). Following Krogh's model that regards vessels as cylinders [90], $V_{net}$ can be written as the sum of cylindrical blood volumes from the level of the heart to the capillary level. Considering two distinct branching flow regimes—corresponding to area-preserving and area-increasing vessel characteristics—that are separated by a branching level that does not depend on body mass, and assuming the number of capillaries are infinitely large, yields metabolic rate $B$ being proportional to $M^{3/4}$ (Eq. (1.2.1)), supporting the empirical data evidence of the metabolic scaling relationship (Fig. 1.5).

Overall, WBE has proposed a highly predictive, network-centric approach to explain the empirical observations of metabolic rate and body mass by considering the vascular system as a main driver whose properties can be derived by implementation of network science methods as well as imposing biological and physical constraints on the architectural design and blood flow properties of the vascular system. This framework has been shown to be useful for studying the large-scale complex structure of the cardiovascular system. However, it has also led to several controversies about assumptions that simplify the dynamics and structure of the network. The debates mostly arise about the validity of the assumptions about the vascular networks that are included in the model. For example, it is unclear if real vascular networks satisfy the assumptions of the structural properties, such as the symmetric branching between sibling vessels, scale-free branching ratios of radius and length across branching junctions, or assumptions about the flow properties such as instantaneous change of flow regimes. Moreover, using extensive data that include more than 600 mammalian species and 64 plant species, it has been shown that the relationship between the metabolic rate and body mass can be better elucidated by a convex curve in log-log space [91–94] (Fig. 1.5b). This evidence further necessitates the need of revising the WBE model by revisiting and altering the underlying assumptions behind the theory. As shown by Savage et al. [11], allowing a finite number of capillaries results in the inclusion of higher-order terms to the approximation that relates metabolic rate and body mass, and combining this with more accurate fluid dynamic relations results in a curvature in the opposite direction as the empirical data. This suggests that revisiting the assumptions behind the existing models is valuable and may lead to promising results in regards to explaining the mismatch between the current allometric scaling theories and the empirical data.

Testing foundations of the allometric scaling theory and accordingly providing a foundation for a revised allometric scaling theory requires access to high quality vascular data. Most of the vascular network data collected to this date is from plasticene casts or dyeing methods of real vasculature and obtained by manual vessel measurements that were time-consuming and labor-intensive [95, 95–97]. However, these methods are error prone as there is a high potential of measurement bias and because the process of casting may damage or alter the shape of vessels. Moreover, manual measurements limit the size of the vessels that can be studied, and hence do not provide sufficiently extensive and detailed data to test the assumptions on the vascular system. To overcome with this lack of vascular data problem, Newberry et al. [5] has recently developed a novel software package, Angicart, that allows automated extraction of vascular network data from angiographic images. In short, given the aligned stacks of three-dimensional images, Angicart extracts the topology of the vascular network with the individual vessel measurements such as branching junctions (nodes of the network) coordinates, radius, length, and volume. By using Angicart on angiographic images, we have access to vast amounts of highly detailed vascular data that is crucial for examining the validity of current models as well as establishing and testing new models [5, 98]. The amount and quality of data collected through Angicart is mainly determined by different imaging techniques as they affect the resolution and the spatial scales that they can identify [5]. In this dissertation, we use Angicart to analyze the cardiovascular structure from micro-CT images of mouse lung (with vessel sizes $> 10$ microns) as well as the MRI of 18 different subject images of human head and torso (with vessel sizes $>1$ mm).

Using Angicart, recent studies by Newberry et al. [5] and Hunt et al. [98] have analyzed the assumptions on the properties of vessel sizes that are commonly accepted by allometric scaling theories. These studies have demonstrated that the empirical data measurements of radius support the model predictions and assumptions, whereas vessel length scaling and asymmetries do not. For testing the symmetry assumption, the ratios of sibling vessel radii or length has been used, and referred to as asymmetry ratios $\lambda_r$ and $\lambda_l$, respectively.

$$\lambda_r = \frac{r_{sibling,1}}{r_{sibling,2}} \ , \qquad \lambda_l = \frac{l_{sibling,1}}{l_{sibling,2}} \tag{1.2.6}$$

where the smaller value (either radius or length) is divided by the larger value. This allows the asymmetry measure to range in between 0 and 1 [99]. By definition, siblings are symmetric if and only if $\lambda_r$ and $\lambda_l$ are equal to 1 (Fig. 1.6), whereas deviation from 1 indicates the deviation from the symmetry (see more detailed discussion in Chapter 4). Intriguingly, the symmetry assumption that sibling vessels have identical characteristics such as radius or length has been shown to fail for vessel length, whereas it provides a reasonably good approximation for the radius for both mouse lung and human head and torso data. In other words, the asymmetry measures $\lambda_r$ and $\lambda_l$—characterizing degree of asymmetry—exhibit systematic features of asymmetry across these two-distinct datasets. Moreover, these findings are consistent with asymmetry patterns observed in plant vascular system [100–102]. As the symmetric branching does not realistically represent the real vasculature, incorporating asymmetry into the model provides a practical direction for revising the modern allometric scaling theories. Indeed, a recent study by Brummer et al. [103] has relaxed the symmetry assumption by introducing a perturbation from the symmetric case and has shown that asymmetry can lead to a variation in the metabolic scaling exponent. This suggests that incorporating asymmetry into the model could eventually help explain the deviation from the pure power-law. Moreover, evidence of systematic asymmetry patterns is suggestive of the role of shared developmental processes and evolutionary principles on the vascular branching.

Developmental processes such as those driven by the metabolic demands of growing tissue and Vascular Endothelial Growth Factor (VEGF) signaling has been shown to be effective in the formation of vascular branching [104]. However, these processes could potentially introduce some stochasticity in the branching geometry especially at the local spatial scale as the curvature of the branching vessel may affect the branching location. Moreover, as the architecture of vascular networks must balance complex demands to efficiently deliver oxygen and resources throughout the entire body, it has been proposed that evolutionary pressures to fulfill these demands must constrain the possible forms of vasculature. In regards to these constraints, two different principles have been posited to play a key role in the determination and optimization of vessel branching: 1. Minimization of material cost required for the construction and maintenance of the vascular system, 2. Minimization of power cost for providing efficient blood flow mechanism, which are referred to as material-cost (MC) optimization and power-cost (PC) optimization, respectively [89,105,106]. These evolutionary constraints are hypothesized to generate deterministic branching organization, and in principle these principles may act at different spatial scales that range from local (junction-level) to global (whole network) with some form of intermediate spatial scale in between local and global.

In Chapter 4 of this dissertation, we first test the validity of the symmetry assumption about vascular branching that is widely used in allometric scaling theories. In addition to the metrics defined for the radius and length for characterizing asymmetry (i.e. $\lambda_r$ and $\lambda_l$ as denoted above), we introduce a similar metric for characterizing branching angle asymmetry represented by $\lambda_\theta$ (see Fig. 4.1c on the schematic illustration of asymmetric branching). Using high-quality vascular network data of mouse lung and human head and torso—obtained via our software Angicart—we identify novel, systematic patterns of asymmetry in vascular branching, potentially explaining previously documented mismatches between predictions (power-law or concave curvature) and observed empirical data (convex curvature) for the allometric scaling of metabolic rate. To examine why these systematic asymmetries in vascular branching might arise, we construct a mathematical framework to derive predictions based on local, junction-level optimality principles that have been proposed to be favored in the course of natural selection and development, i.e. MC and PC optimizations. To quantify the degree of spatial scales as well as stochasticity of the branching process, we further explore random branching that is constrained at spatial scales that vary from local to global. Subsequently, we compare our predictions and random simulations of branching with real data and identify differences in vascular branching of mouse lung and human head and torso. Providing a comprehensive evaluation of these different branching schemes help us to better understand how the structure of vascular system is constrained by important biological and physical principles as well as the spatial scales.

Overall, in this research, we examine two distinct networks—drug interaction networks and cardiovascular networks—by addressing several shortcomings of previous studies and offering advanced understanding of these networks with the help of our comprehensive data analysis and rigorous mathematical framework. Via our network-centric approach, we identify emergent patterns in higher-order drug interactions and vascular networks and subsequently argue that integration of our knowledge across these network systems are especially valuable towards analyzing and forecasting the emergent properties in other complex systems.

# CHAPTER 2

# Uncovering Emergent Interactions in Three-Way Combinations of Stressors

## 2.1 Introduction

Drugs are now a pervasive part of our everyday environment and have both helpful and harmful effects on biological systems from the molecular up to the individual, population, and whole ecosystem level [107]. In the clinic, drugs are used to combat pathogens but resistance to drugs such as antibiotics is becoming more common, largely because these drugs are used so pervasively throughout our environment, from hand soaps to agriculture. One strategy for countering antibiotic resistance is to use drugs in combination to more effectively kill pathogens, to combat drug-resistant strains, and to help slow the evolution of resistance [28, 29, 37, 108]. Ideally, this strategy would be used in tandem with the development of new drugs, but pharmaceutical companies are not investing heavily in antibiotics [109]. Thus, there is a compelling case for the critical importance of devising effective antibiotic combinations for use in the clinic. Past work has largely focused on two-drug interactions [28, 29, 110, 111], but multi-drug therapies in the clinic are increasingly moving in the direction of higher-order combinations (those involving three or more drugs). Indeed, some of the best-known drug treatments, including HIV drug cocktails [112] and treatments for *Mycobacterium tuberculosis* infections [68], involve three-drug combinations.

To find effective higher-order drug combinations, one of the key challenges is to correctly identify the type and magnitude of drug interactions because combining non-interacting drugs does not leverage the benefits of certain interaction types. A useful categorization when two drugs are combined is: 1. Synergistic—the interaction of the two drugs enhances the effect expected based on each drug alone with no interactions; 2. Antagonistic—the interaction reduces the expected effects; or 3. Additive—there is no interaction and the combined effect matches the expected effect. Synergistic drug combinations are useful because they kill bacteria more effectively and are advantageous for individual patients, while antagonistic drug combinations are useful because they may be able to help slow the evolution of antibiotic resistance [37, 38, 113]. In this paper, we extend ideas about these categorizations to higher-order interactions, including both net (arising from either pairwise or three-way combinations) and emergent (not arising solely from pairwise combinations) interactions.

Empirical studies of ecotoxicology and ecological disturbances have examined the nature of interactions in the lab [114–116] and in the wild [117, 118]. Both synergistic [119–126] and antagonistic [124, 127–129] interactions have been uncovered in a wide range of organisms, environments, and systems that range from gene epistasis [130–132] to predator-prey interactions [74]. Nevertheless, higher-order interactions that involve more than two stressors are still poorly understood. Moreover, because three-drug combinations have received substantially less attention than two-drug combinations, there are many basic questions about three-way and higher-order interactions that remain, such as: Are there emergent properties that arise in three-drug combinations that cannot be predicted from the pairwise parts? As we increase the number of drugs, do we increase the proportion of synergistic or antagonistic interactions?

This lack of understanding and answers for three-way and higher-order interactions is partly due to the difficulty of obtaining measurements for the effects of all single, pairwise, and higher-order combinations and partly due to the lack of a rigorous quantitative and conceptual framework that distinguishes between net and emergent interactions. Here we help address both issues by using a tractable, empirical lab system in which *Escherichia coli* is exposed to environments of antibiotic combinations that allows measurements of effects of all subsets of drug combinations, and by developing an explicit and rigorous theoretical framework that encompasses both net and emergent higher-order interactions.

Empirically, as a model system for studying and addressing outstanding questions about interactions among stressors, antibiotics and bacteria offer several advantages: i) the control of levels of the drugs in the environment and of fluctuations in concentration across time and space; ii) the use of a specific ordered set or randomized set of antibiotics; and iii) knowledge about the mechanisms of action for the antibiotics used in this study, allowing the selection of specific pathways in the bacteria that we want to disrupt. Moreover, the use of well-designed experiments in highly simplified microbial systems can make even complex problems tractable [133].

We also develop a novel theoretical framework to understand and to quantify which higher-order combinations of stressors produce emergent interactions, meaning that the interaction does not arise from single and pairwise interactions alone. For example, in the system of drugs as stressors, a three-drug synergy or antagonism may not actually be the result of all three drugs in combination. Instead, such interactions may come from an interaction of just two of the drugs. On the other hand, it may be possible that synergy can arise in a three-drug combination in which no two-drug interactions show synergy, i.e. an emergent synergy. This is an important distinction because true synergies—those that only emerge with all three drugs—could provide novel treatments, whereas a three-way synergy that merely arises from a synergistic pairwise interaction would not be particularly novel. Such superficial three-drug synergies may be detrimental to the patient because additional drugs might be added that are in actuality not needed for increased pathogen killing efficiency. As a result, it is challenging to determine which specific drug combinations are most clinically relevant [3, 28, 108].

Key advances were made in the few previous studies that focused on three (or more) drug interactions. In particular, Wood et al. [13] applied Maximum Entropy methods to six combinations of three antibiotics that varied across a range of concentrations. In this way, they searched for three-way interactions that could not be predicted from pairwise interactions. As part of this study, they discovered a simple and highly informative algebraic metric related to the one for emergent interactions we derive below. More recently, Zimmer et al. [71] used a framework that incorporates interaction coefficients as part of a model based on Hill functions to show how to increase predictive power for three-way interactions based on limited information about pairwise interactions across a range of drug concentrations.

Our work shares some core goals and similarities with these previous approaches. Although our study is currently more limited with regard to understanding ranges of drug concentrations as studied in Wood et al. [13] and Zimmer et al. [71], there are a few central contributions represented by our approach. First, our study provides a clear conceptual derivation for the simple algebraic measures presented below, and in so doing, further reveals a way to differentiate between the emergent interaction (an interaction that only exists when all three drugs are present) and the net interaction (the overall interaction in comparison to single drug effects). Second, in contrast to other higher-order interaction studies, we also rescale the raw magnitude of our metrics in order to compare information and categories that correspond to baselines for synergistic and antagonistic interactions, as previously done by Segre and colleagues for pairwise interactions [16]. Third, we consider a much larger set of three-antibiotic combinations (20 as opposed to 6 [13]), though we only take measurements at fixed concentrations for these combinations. We also identify higher levels of net and emergent three-way interactions, including both synergy and antagonism, than previous studies on higher-order interactions, as explained in the Discussion section. As we will demonstrate below, the distinction between net versus emergent interaction provides compelling results, especially in the case of antagonistic interactions for combinations of antibiotics.

More generally, for any system involving more than two stressors, it is not obvious *a priori* whether the higher-order combination will interact in ways that are easily predictable from their single or pairwise effects. Although the theory and experiments in this paper have been developed using antibiotics and bacteria as an example, we suggest the terms and concepts developed here could be usefully translated, at least as a starting point, to think about other stressors and systems. For instance, studies of how multiple predators affect prey population dynamics may provide a strong correspondence because the survival rates of prey species are analogous to the growth rates of bacteria in multiple drug environments (for example, see [127]) and appear in the Multiple Predator Effects (MPE) metrics in the same exact form as in our metrics for net interactions (i.e., the deviation from additivity measure) below. Notably, MPE methods do not differentiate between net and truly emergent interactions or rescale the magnitude of their metrics to assess the information about interactions, which is why we think our framework might also be generalized to resolve questions about MPEs. In the Discussion, we provide more details on how the framework with drugs as stressors can be applied to MPEs and other systems that cover similar concepts to those described in this paper.

In the remainder of the paper, we explain our approach for quantifying and understanding higher-order interactions. In doing so, we create a framework to classify higher-order combinations of stressors by examining net three-drug interactions and comparing them with all three pairwise interactions for each three-drug combination. Next, we use this framework to uncover interactions among a set of six antibiotics by examining systematically all 20 of the possible three-drug combinations. In experiments with wild-type *E. coli*, we measure growth rates of bacteria in single, pairwise, and three-drug combinations, and we identify emergent three-drug combinations that require all three antibiotics to yield synergistic or antagonistic interactions.

## 2.2 Materials and Methods

### 2.2.1 Experimental data

***Escherichia coli* strain and growth conditions.**The strain of *E. coli* used in these experiments is BW25113, the wild-type strain (lacI$^q$ rrnB$_{T14}$ $\Delta$lacZ$_{WJ16}$ hsdR514 $\Delta$araBAD$_{AH33}$ $\Delta$rhaBAD$_{LD78}$) [134] derived from the strain W1485 background [135]. All experiments were conducted using LB media (10 g/l tryptone, 5 g/l yeast extract, and 10 g/l NaCl). Frozen glycerol cultures, stored at -80°C, were made by inoculating from a culture made from a single colony. Experiments were started by inoculating from a resuspension of this glycerol culture in MC buffer stored at 4°C and grown for 5 hours in a 37°C incubator before being used to seed overnight cultures. Overnight cultures were seeded by inoculating 975 $\mu$l cultures with 25 $\mu$l of a $10^{-4}$ dilution of the over-day culture. After 18 hours of incubation at 37°C in a shaker at 215 rpm, the optical density at 600 nm (OD$_{600}$) was measured.

**Antibiotics.** Antibiotics included in this survey were chosen to cover a broad range of biochemical classifications [136]. Drugs included are clindamycin hydrochloride (Sigma C-5269), ciprofloxacin hydrochloride (MP Biomedicals 199020), tobramycin sulfate (Sigma T-1783), streptomycin sulfate (Sigma Aldrich S-6501), cefoxitin sodium salt (Fluka C4786), and erythromycin (Sigma Aldrich E-6376). Mechanisms of action, abbreviations, and dosage are listed in Table 2.1.

| Drug | Abbreviation | Dose Range ($\mu$ g ml$^{-1}$) | Main Mechanism(s) of Action |
|---|---|---|---|
| Clindamycin | CLI | 17.5-31.5 | Protein synthesis, 50S |
| Ciprofloxacin | CPR | 0.009-0.013 | DNA gyrase |
| Tobramycin | TOB | 0.5-1.3 | Aminoglycoside, protein synthesis, 30S |
| Streptomycin | STR | 1.0-5.0 | Aminoglycoside, protein synthesis, 30S |
| Cefoxitin | FOX | 0.90-1.16 | Cell wall |
| Erythromycin | ERY | 12-30 | Protein synthesis, 50S |

**Table 2.1:** List of all antibiotics used in the study, abbreviation, dose range, and mechanism of action.

**Growth measurements of no drug and single, double, and triple antibiotic combinations.** A range of concentrations was first tested for each individual drug to determine the appropriate non-lethal concentration required to reduce growth by 15-35% compared to the no drug-control (LB). We choose this amount of reduction in growth rate because larger reductions would yield lethality in two-drug combinations, making three-drug effects irrelevant, and also because smaller reductions may make it difficult to tease apart additivity and antagonism. The range from 15-35% was necessitated by the variability in antibiotic sensitivity of single-drug treatments in our empirical system, representing a limit to our ability to choose the exact same reduction in growth rate across all drugs and experiments. We use an additive design, meaning that we test bacterial response to a set concentration of $X$ (denoted [X]), a set concentration of $Y$ (denoted [Y]), a set concentration of $Z$ (denoted [Z]), and all pairwise combinations, [X]+[Y], [Y]+[Z], and [X]+[Z], and the triple combination [X]+[Y]+[Z]. This additive design is standard in the field of drug interactions [28], and we use the additive design to standardize with other drug interaction studies.

To measure the effect of the triple combination of drugs versus the pairwise and individual effects, each experiment was performed using a no-drug control, a control for each individual drug at the previously determined concentration, pairwise combinations of the three drugs, and a triple-drug combination (Supplementary Table 1). We also examine dose-dependence for ten different drugs, including the six drugs used in the triple combination experiments. For each drug, we measure effects of concentrations [X], [2X], and [3X] (Supplementary Table 2) according to the metrics defined here (Equations (2.2.2) and (2.2.4)). These data show that our methods usually classify drugs as additive with themselves, meaning that the growth rates predicted by$w_X w_X$ or $w_X w_X w_X$ based on concentration [X] matches with the measured effects from drug concentrations of [2X] and [3X], respectively.

In all cases, drugs were added to appropriate concentrations in 1 ml LB (inoculated as described above), and 100 $\mu$l was aliquoted into 4 to 6 wells of a 96-well plate. Cell densities were then determined after 18 hours of incubation (as described above) using optical density analysis at 600 nm. Optical density readings were used to calculate growth percentages as compared to the no-drug control. Each three-drug combination experiment was repeated at least three times, but due to minor changes in drug concentrations across different experiments, the number of replicates reported for each specific concentration of drugs may be two in some cases. Data are represented as median, minimum, and maximum for repeated three-drug combination experiments. Graphs of triple-antibiotic interactions were produced using MATLAB version R2013a.

### 2.2.2 Theoretical framework

**Pairwise Interaction Measure.** In previous work on pairwise interactions of drugs [3] and metabolic genes [16], drug interactions have often been classified using the definition of Bliss Independence (BI) [28]. BI defines drugs to be independent (or additive) when the percent change in bacterial fitness in the presence of one drug ($X$) does not depend upon the presence or absence of the other drug ($Y$) (see Eq. 2.2.1 below). The percent change in fitness can be measured by the relative fitness, defined as the ratio of growth of the bacteria in the presence of a drug relative to the growth when no drug is present. For instance, in the presence of drug $X$, the bacteria has relative fitness, $w_X = e^{-s_X}$, where $s_X$

is the selection coefficient that measures how a specific drug concentration of $X$ affects the bacterial fitness. We follow the same notation for other drugs $Y$ or $Z$ or any combination of drugs. According to BI, in the presence of two non-interacting drugs, the fitness of the bacteria is $w_{XY} = w_X w_Y = e^{-(s_X+s_Y)}$, where the $XY$ subscript denotes a combination of drugs $X$ and $Y$ (denoted by $X+Y$ in our figures) and is consistent with previous notation.

This non-interacting case is called additive because the selection coefficients add together, $s_X + s_Y$. Consequently,

$$\mathrm{DA}_{X,Y} = w_{XY} - w_X w_Y \tag{2.2.1}$$

measures the deviation from additivity (DA). By definition, this measure is zero when $X$ and $Y$ are additive. When this measure is positive and sufficiently large in magnitude (see below), the interaction is called antagonistic because the drugs are working against each other such that the bacterial growth is higher than would be expected based on the two single-drug effects and no interactions between the drugs (i.e., additivity). When this measure is negative and sufficiently large in magnitude, the interaction is synergistic because the drugs are working together such that the bacterial growth rate is lower than would be expected based on the two single-drug effects and no drug interactions. The additive range defined below in terms of the rescaled measure is based on conservative values described by Yeh et al. [3]. When considering pairwise combinations of $X$ and $Y$ with a third drug, $Z$, there are two more pairwise DA measures that describe $X$ interacting with $Z$, $\mathrm{DA}_{X,Z} = w_{XZ} - w_X w_Z$, and $Y$ interacting with $Z$, $\mathrm{DA}_{Y,Z} = w_{YZ} - w_Y w_Z$.

**Three-Way interaction measures.** We now develop two interaction measures for three-drug combinations. The first is the direct extension of the DA measure for two drugs in Eq. (2.2.1) [13,62,69]. When the drugs do not interact, the fitness of the bacteria exposed to the three-drug combination should be equal to the product of the fitnesses of bacteria exposed to each single drug alone, i.e., $w_{XYZ} = w_X w_Y w_Z$. Therefore, deviation from additivity (DA), which measures the net interaction, is given by

$$\mathrm{DA}_{X,Y,Z} = w_{XYZ} - w_X w_Y w_Z \tag{2.2.2}$$

To characterize emergent interactions that arise when all three drugs are combined, we need to assess how much of the three-drug interaction does not originate from pairwise interactions. To measure how much of the interaction arises from a single pairwise interaction, we recognize that a single pairwise interaction creates the entire three-drug interaction when the third drug is additive with the other two drugs. That is, the interaction between drugs $X$, $Y$, and $Z$ is due solely to the interaction between drugs $X$ and $Y$ when drug $Z$ is additive with their combination (e.g., $w_{XYZ} = w_{XY}w_Z$). For this special case, $\mathrm{DA}_{X,Y,Z} = w_{XY}w_Z - w_X w_Y w_Z = w_Z(w_{XY} - w_X w_Y) = w_Z \mathrm{DA}_{X,Y}$ based on Eqs. (1-2). By identical reasoning, the contribution coming solely from the interaction of drugs $Y$ and $Z$ is $w_X \mathrm{DA}_{Y,Z}$ and from the interaction of drugs $X$ and $Z$ is $w_Y \mathrm{DA}_{X,Z}$. For three drugs, these three terms represent all three of the possible pairwise interactions among single drugs. Therefore, all three of these pairwise contributions need to be subtracted from the overall three-drug interaction (Supplementary Fig. 1) in order to introduce a new measure that we term the emergent three-way (E3) interaction

$$\mathrm{E3} = \mathrm{DA}_{X,Y,Z} - w_X \mathrm{DA}_{Y,Z} - w_Y \mathrm{DA}_{X,Z} - w_Z \mathrm{DA}_{X,Y} \tag{2.2.3}$$

When all of the pairwise interactions are additive (i.e., $w_{XY} = w_X w_Y$, etc.), no part of the three-way interaction could possibly originate from pairwise interactions, and the E3 measure reduces to the DA measure ($\mathrm{E3} = \mathrm{DA}_{X,Y,Z}$), as it must. Substituting Eqs. (2.2.1) and (2.2.2) into Eq. (2.2.3) allows the E3 measure to be expressed purely in terms of relative fitnesses

$$\mathrm{E3} = w_{XYZ} - w_X w_{YZ} - w_Y w_{XZ} - w_Z w_{XY} + 2 w_X w_Y w_Z \tag{2.2.4}$$

In summary, by construction our new E3 measure provides a simple calculation for capturing the part of the three-drug interaction that is emergent and not due to pairwise interactions, while the DA measure captures whether there is an interaction at all.

**Re-scaled three-way interaction measures.** Following Segre et al. [16] we rescaled both of our interaction measures, $\mathrm{DA}_{X,Y,Z}$ in Eq. (2.2.2) and E3 in Eq. (2.2.4), by dividing them by the absolute value of the same functional form as the unscaled metrics, but with $w_{XYZ}$ replaced by 0 when the unscaled metric is negative (synergistic) and by the minimum value of the single-drug fitness, $\min(w_X, w_Y, w_Z)$, when the unscaled metric is positive (antagonistic) [62, 69]. Effectively, this rescaling allows us to characterize the degree of synergy relative to the extreme lethal synergy case—when the combination of drugs completely kills the bacteria so that fitness ($w_{XYZ}$) is 0, even though no single drug completely killed the bacteria. All positive interactions are rescaled by the case of buffering antagonism—when drugs combine to have the same effect as the single drug with the strongest effect.

Our re-scaled E3 measure is similar to a term introduced by Darroch [137] and Kroonenberg and Andersen [138] who considered regression models and interaction terms. Importantly, our measure differs from these regression models because we assume non-linear exponential fitness functions rather than linear approximations implied by linear dependencies for single-drug effects in these previous regression models. This linear approximation will be especially problematic for drug interactions that push growth rates more towards lethality (often synergy) or wild type (often antagonism) and correspond to the exact regions where this linear approximation must break down. Moreover, these previous studies always re-scale according to our synergistic case, meaning they are using the wrong baseline or scale bar for antagonistic interactions. Finally, they either assume or hypothesize that their measure is always zero, meaning they assume there is no interaction before even comparing with data.

**Cut-off values for determining three-way interaction types.** Because of the variability between different interaction measures, and between fractional inhibitory concentration index data [139], cut-off values for determining three-way interaction types must be chosen cautiously. Our method for determining the type of three-way interaction follows previous work [3, 16]. To calculate our rescaled three-way interaction measures, we use the median of replicate measurements for each experiment at a single antibiotic concentration. We then use the conservative cut-off values of rescaled $\mathrm{DA}_{X,Y,Z}$ (or rescaled E3) $> 0.5$ for antagonism and rescaled $\mathrm{DA}_{X,Y,Z}$ (or rescaled E3) $< -0.5$ for synergy. Note that rescaled interaction measures tend to range from values of $-1$ (synergistic lethality) to 1 (complete antagonistic buffering). Hence, any value between −0.5 and 0.5 represents an additive interaction. These cut-off values are also based on natural breaks in the histogram distribution for the rescaled epsilon value and are consistent with the conservative values described for pairwise interactions in Yeh et al. [3].

## 2.3 Results

### 2.3.1 Identification of triple-drug interactions

Comparing the two distinct interaction measures, as depicted using schematics with idealized data (Figs 2.1 and 2.2) and explained above we found that three-drug combinations can in principle have several distinct effects—additive according to either or both measures, synergistic according to either or both measures, and antagonistic according to either or both measures (Supplementary Fig. 2 and Supplementary Table 1). Experimental data are shown in triple-drug combination figures for examples of both synergistic (Fig. 2.3a) and antagonistic (Fig. 2.3b) interactions according to our emergent three-way (E3) interaction measure, which captures three-drug interactions that do not arise from pairwise interactions.

Overall, examination of all 20 of our three-drug combinations revealed that 35% exhibit emergent, higher-order interactions, including two emergent synergistic interactions (Fig. 2.3a and Supplementary Fig. 2) and five emergent antagonistic interactions (Fig. 2.3b and Supplementary Fig. 2).

### 2.3.2 Deviation from additivity (DA) versus emergent three-way (E3) interactions

Our data show that when we categorized interaction types according to the DA measure, the distribution of interactions was skewed towards synergistic effects (Fig. 2.4a, skewness = 0.71). Conversely, when we used the E3 measure, the distribution skewed towards antagonistic effects (Fig. 2.4a, skewness = -0.98). We also compared the number of synergistic and antagonistic interactions according to each method (Figs 2.4b and 2.4c). We found

**Figure 2.1: Schematic of triple-drug combination effects according to deviation from additivity (DA).** Relative growth rates for bacteria populations in one-drug, two-drug, and three-drug combinations are shown as increasing from 0% growth in the center to 100% growth (no-drug control) at the largest outer circle of the polar graph. Growth rate is shown for single-drug (black bars), two-drug (blue bars with corresponding single-drug treatments adjacent), and triple-drug combinations (radius of inner circle). Shading of the inner circle indicates nature of pairwise interactions (red: synergistic, green: antagonistic, no shading for additive). Outline coloring of inner circle indicates measure of DA (black: additive, red: synergistic, green: antagonistic). Three possible triple-drug combination effects are depicted schematically for theoretical drugs $X$, $Y$, and $Z$ according to measures of DA. (**a**) Strictly additive interactions of all pairwise combinations and three-drug combination. (**b**) Synergy of three drugs according to DA. (**c**) Antagonistic interaction of three drugs according to DA.

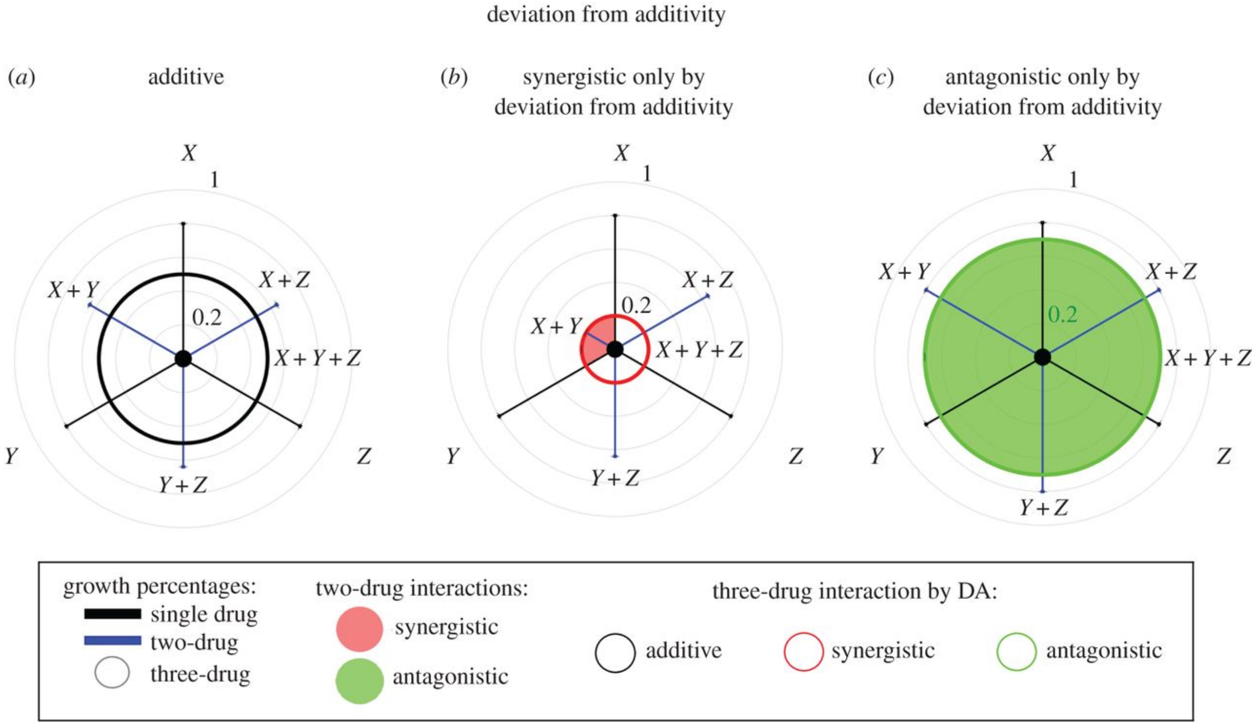

**Figure 2.2: Schematic of triple-drug combination effects according to emergent three-way (E3) interactions.** Relative growth rates for bacteria populations in one-drug, two-drug, and three-drug combinations are shown as increasing from 0% growth in the center to 100% growth (no-drug control) at the largest outer circle of the polar graph. For the E3 interaction measure, the single, two-drug, and triple-drug combination growth rates, as well as pairwise interactions, are shown with the same color coding as used for the DA measure (Fig. 2.1), but with outline coloring of the inner circle indicating measure of E3 (black: additive, red: synergistic, green: antagonistic). Three possible triple-drug combination effects are depicted schematically for theoretical drugs $X$, $Y$, and $Z$ according to measures of E3. (**a**) Interactions combine additively according to E3, even though several pairwise interactions are synergistic. (**b**) Emergent synergy of three drugs according to E3. (**c**) Emergent antagonism of three drugs according to E3.

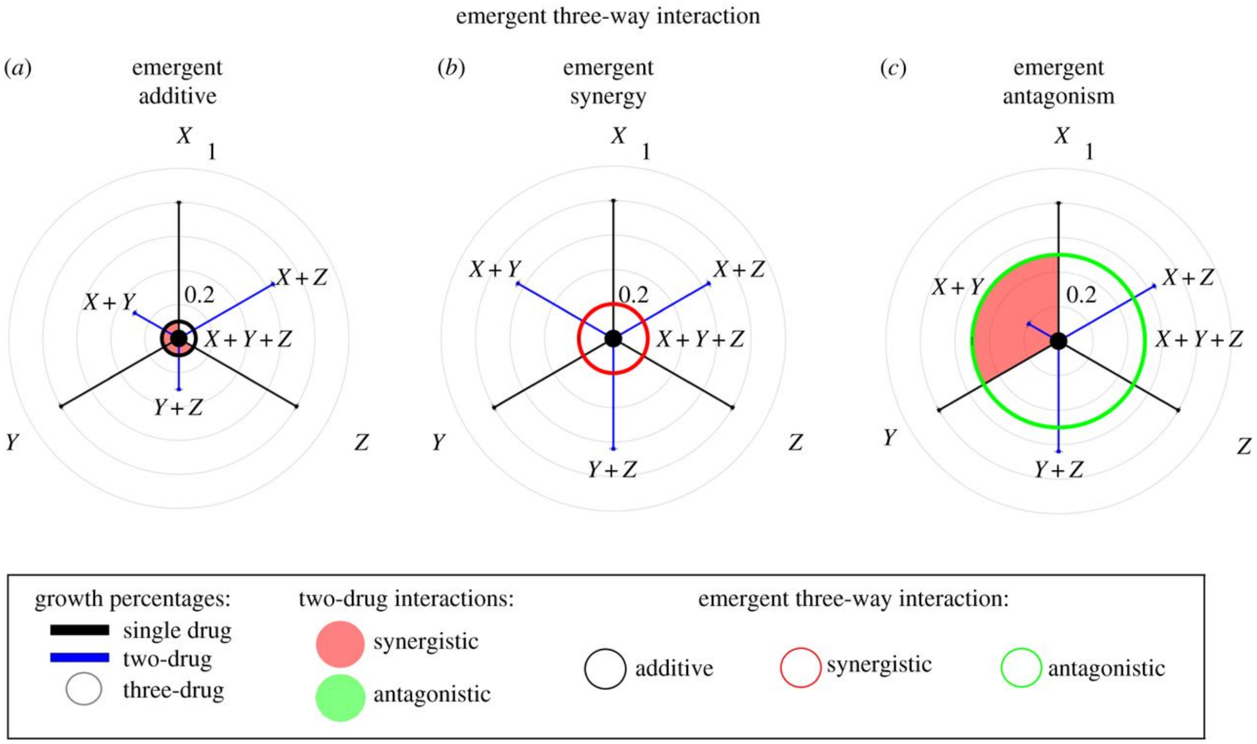

**Figure 2.3: Emergent synergistic and antagonistic interactions in triple antibiotic combinations.** Data for triple-antibiotic figures are shown according to emergent three-way (E3) interaction measures. Figures are presented as described in Figs 2.1 and 2.2. Data are represented as median ± minimum/maximum. (**a**) The combination of ciprofloxacin 0.013 g/ml (CPR), clindamycin 31.5 g/ml (CLI), and erythromycin 14 g/ml (ERY) interacts synergistically in three-drug combinations according to both deviation from additivity (DA) and emergent (E3) measures. (**b**) The combination of erythromycin 14 g/ml (ERY), cefoxitin 1.16 g/ml (FOX), and tobramycin 1.3 g/ml (TOB) interacts antagonistically in three-drug combinations according to the E3 measure and additively according to the DA measure. Only data for one concentration of each antibiotic is shown, although each three-drug combination was tested in a minimum of three independent experiments (see 2.2 Materials and Methods).

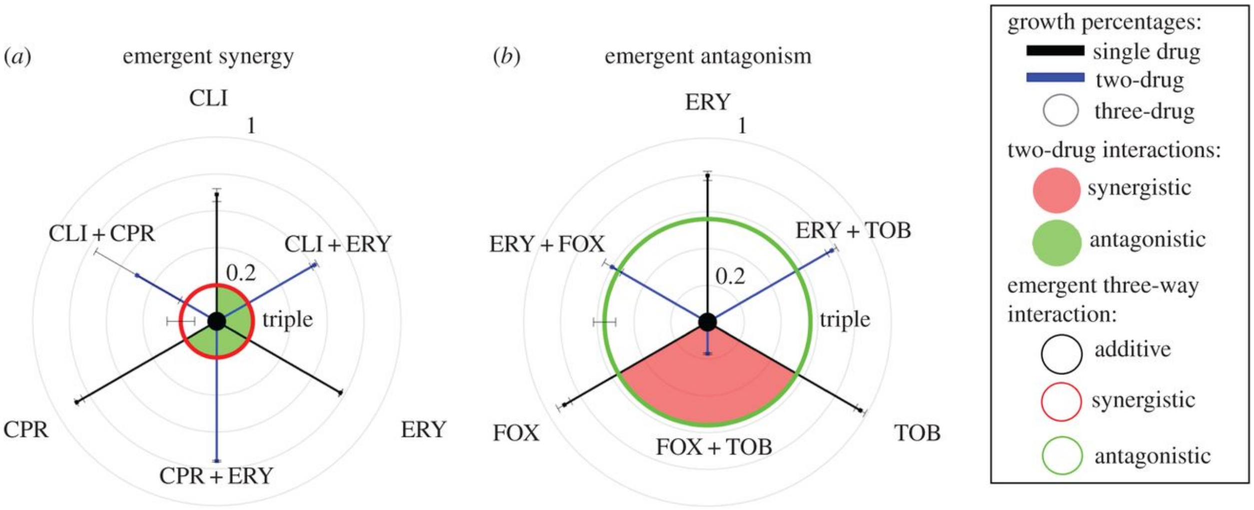

9 of 20 cases to be synergistic according to the DA measure. That is, the growth of the triple combination was often lower than the expected growth based on single-drug effects. However, only two of these cases were synergistic according to the E3 measure. Because the E3 measure leads to fewer synergistic classifications than the DA measure, the synergistic effects measured by DA are often the result of synergistic pairwise interactions, rather than an emergent interaction of the three drugs. Conversely, only three of 20 combinations were antagonistic according to the DA measure whereas five of 20 cases were found to be antagonistic according to the E3 measure, meaning that the growth of bacteria under triple-drug combinations was considerably higher than the expected growth based on pairwise interactions. Frequency of specific antibiotics involved in emergent synergistic and antagonistic three-drug interactions are given in Supplementary Fig. 3.

**Figure 2.4: Comparing interaction measures for triple-drug combinations.** Comparison of measures of deviation from additivity (DA) and emergent three-way (E3) interactions are based on 20 triple-drug combination experiments. Of the 20 combinations, E3 is non-applicable in four cases because of both two-drug and three-drug lethality. Thus, it is impossible to see the effect of the third drug. DA is applicable in all cases because this measure ignores two-drug effects. (**a**) Overlapping histograms for measures of DA (white bars) and E3 interactions (black bars) with bin size of 0.1. (**b**) Venn diagram comparing overlap between synergistic three-drug interactions according to measures of DA and E3 interactions. (**c**) Venn diagram comparing overlap between antagonistic three-drug interactions according to measures of DA and E3 interactions. In both (**b**) and (**c**), the shaded area indicates the combinations which are fully synergistic or antagonistic, that is, synergistic in both DA and E3 measurements, or antagonistic in both measurements.

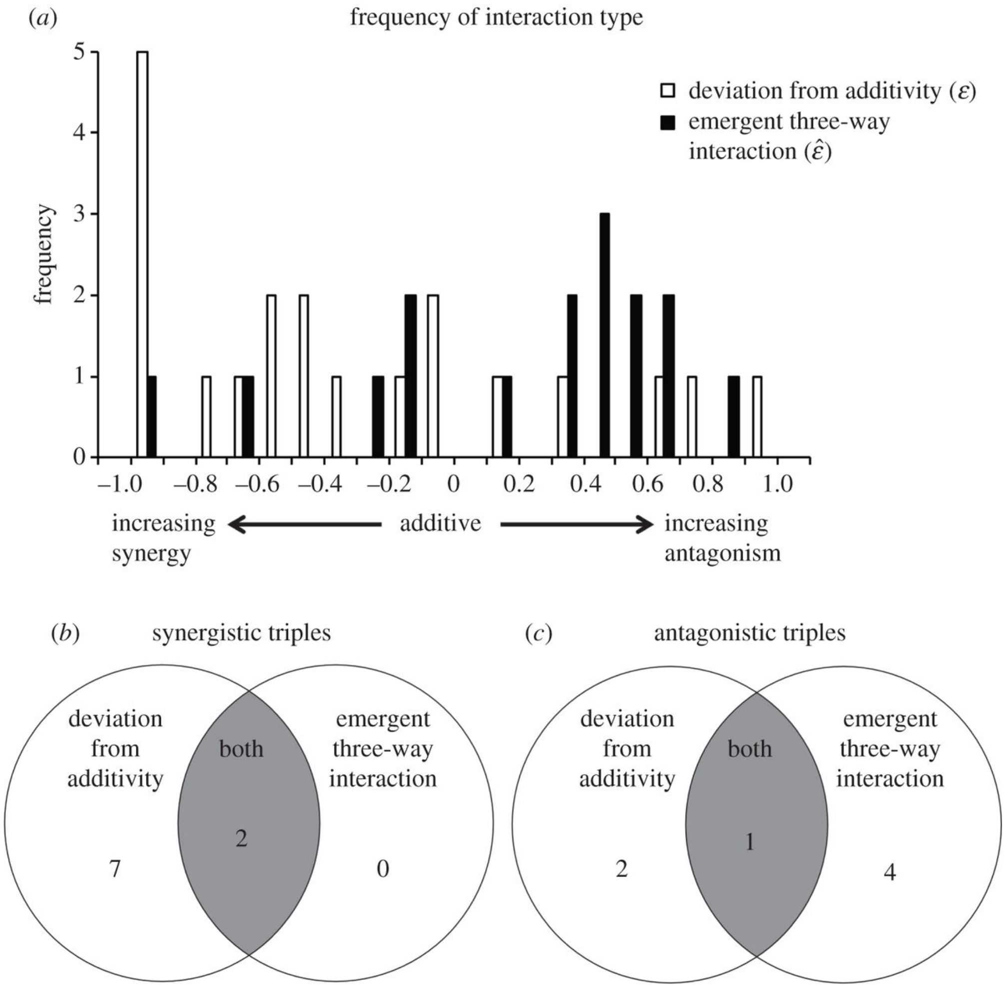

In the case of synergies, every emergent synergy was also considered synergistic as measured by DA (Fig. 2.4b). This was not true for antagonism, where most emergent antagonistic combinations (four out of five as measured by E3) were not also antagonistic by the DA measure (Fig. 2.4c). In addition, there were only two triple-drug combinations that were antagonistic solely from the DA measure, compared to seven triple-drug combinations that were synergistic solely from the DA measure.

## 2.4 Discussion

In this paper, we have conducted comprehensive experiments to measure all single, pairwise, and three-way interactions for a set of 6 antibiotics. We also developed a metric to quantify whether there are interactions that arise only when all three drugs are present and are not simply a result of pairwise combinations, and we refer to this type of interaction as an emergent three-way interaction. Using these experiments and theory, we systematically investigated three-drug interactions for our set of 6 antibiotics and showed that our new emergent three-way (E3) measure is conceptually distinct and yields considerably different results from the default method for analyzing interactions according to the deviation from additivity (DA) measure. As we explained, this DA measures quantifies net three-way interactions that could be arising from interactions among either drug pairs or all three drugs. Thus, the E3 measure can be used to identify three-component interactions that have emergent properties—whether synergistic or antagonistic.

Notably, we find higher levels of emergent drug interactions than previous work, including an impressive study by Wood et al. [13] that involved 6 three-way antibiotic combinations at a range of concentrations (in contrast to our 20 three-way combinations at fixed concentrations). Interactions in these data were searched for by Wood et al. [13] using Maximum Entropy methods and more recently by Zimmer et al. [71] using a model based on Hill functions and interaction coefficients. Those studies concluded that the vast majority of three-way interactions are additive or can be predicted from pairwise interactions. This important difference in results and conclusions is likely because neither of these previous studies performed a rescaling based on Maximum Entropy or other methods to set a baseline expectation for synergy or antagonism as done here or in previous pairwise studies [3,16]. Indeed, some of us recently re-analyzed Wood et al.'s data using a few rescaling methods and did find the existence of several higher-order emergent interactions [6].

In addition, these previous studies did not explicitly distinguish between net interactions and emergent interactions as done here, and thus did not look for patterns that we find, such as emergent (E3) higher-order interactions tending to be more antagonistic than net (DA) higher-order interactions. Indeed, our results suggest emergent synergies in three-drug combinations are infrequent but do exist. Before further investigation of these emergent synergies, however, it is important to note that there are cases of emergent synergies that may not be clinically advantageous. From a clinical standpoint, designing the most effective drug treatments requires using three-drug combinations that have a net interaction—producing more effect than expected based on single drugs—and that have an emergent interaction—all three drugs produce more effect than expected based on pairwise interactions. Otherwise, there is little to be gained by using the three-drug combination because more drugs would be used than may really be necessary. Consequently, the optimal three-drug combinations are likely those that show the same type of interaction according to both the DA and E3 measures, corresponding to the shaded intersection region in the Venn diagrams in Figs. 4b and 4c. We see there are two such fully synergistic interactions (and one such fully antagonistic interaction) among the 20 combinations we studied.

This relative paucity of synergistic interactions can be better understood by taking a wider perspective and by looking at the entire histogram of the E3 measure that reveals the overall distribution of interaction types. Our study shows that when taking into account pairwise (as opposed to single-drug) effects, the amount of antagonism increases, as seen by the rightward shift of the distribution in Fig. 2.4a. According to the DA measure, it may appear that the addition of more drugs leads to greater synergism. However, when we look for emergent properties of three-component interactions according to the E3 measure, we find that emergent interactions are in fact more often antagonistic. Natural populations, such as soil environments, often have many different species, including multi-drug resistant strains that produce many different antibiotics [140, 141]. It therefore seems likely that in the wild the outcome of many interacting antibiotics would be antagonistic to attenuate the effects suffered by natural bacteria. Given that synergistic and antagonistic interactions are roughly equally represented among pairwise interactions [3], there is no obvious explanation for this potential paradox.

Interestingly, within the drug literature, synergistic interactions appear to garner more attention and research than antagonistic ones. In the clinic, the goal is to use the synergy as a positive to eradicate the entire population of harmful bacteria due to the greater killing efficiency of synergistic drugs. However, from a basic rather than applied perspective, there is no reason to place primacy on synergism because the percentage of antagonistic interactions, in both drug-drug and ecological-driver effects, are roughly equal to the percentage of synergistic interactions. (In drug studies, 26% were found to be synergistic and 37% antagonistic [3]; in terrestrial systems, 35% synergistic and 42% antagonistic [127]; and in marine systems, 36% synergistic and 38% antagonistic [72]). Moreover, our study suggests that antagonism becomes more frequent than synergism when searching for emergent higher-order interactions. Furthermore, antagonism itself is relevant and interesting when examining drug combinations, given that that antagonistic drug combinations may be better at slowing down the evolution of resistance [38] and decreasing the likelihood of resistance evolving [113].

A natural extension of the methods and results in this paper would be to allow stressors to be adjusted across a large gradient by changing drug concentrations, thereby covering cases like those studied by others Wood et al. and Zimmer et al. [13,71], to determine if our findings about the prevalence of synergistic and antagonistic interactions still hold. Dose-dependent interactions with three or more drugs [56, 70, 71, 142] have been studied by extending the Loewe Additivity measure that classifies two-drug interactions based on lines of equivalent growth rates (isobolograms) across a range of concentrations of the combined drugs. In this regard, a study by Jonker et al. [143] utilizes Loewe Additivity and provides a model that can test whether the interaction type is independent of the absolute concentrations of the combined drugs or dependent only upon the dose-ratios of the drugs. Further work is required to extend our framework in order to identify emergent interactions when there is a gradient of drug concentrations.

Another possibility to consider for combinations of drugs is that stressors can occur in sequence, rather than simultaneously, and with different timings [117]. If drug interactions depend on the sequence and timing with which the drugs are administered, these factors could be optimized for pathogen treatments for patients. Therefore, sequential multi-stressor interactions are a topic that could be explored in the future by using and extending our new framework on emergent interactions.

This framework could also be generalized to other systems with three or more component interactions that require quantitative analysis. As an example of our framework applied to more than three components, we derive the emergent four-way interaction measure in Supplementary Text 1. Although our experiments were carried out in a bacteria-antibiotics system, the questions addressed here about interactions are also relevant to larger scale systems in terms of ecological drivers and survival of populations, species, and biodiversity. Most of the core questions in ecology revolve around how species interact with each other and the environment. Although several meta-analyses of ecological two-stressor interactions have been conducted, three-stressor interactions have been examined much less frequently (but see [72, 73]). Crain and colleagues conducted a comprehensive review of how a third stressor affects two-stressor interactions in marine systems. In their paper, they quantified the pairwise interactions in the presence and absence of the third stressor, and they found that the addition of a third stressor often caused the interaction between the first two stressors to become more synergistic [72]. Similarly, Chen and colleagues used three-way ANOVA to analyze an empirical study with three stressors on zooplankton and amphibians. They found that the three-stressor combination had synergistic effects that harmed survival and reproduction of the two study species [73]. However, in these studies, it is difficult to determine what is an emergent interaction because the effects of the three-stressors combined together are not explicitly compared with all single and all pairwise stressor interactions. More discussion on the comparison of three-way ANOVA and our emergent three-way interaction measure can be found in Appendix A and Supplementary Text 2.

Within the field of ecology, analogous to the idea of emergent properties from three-drug combinations is the idea of emergent effects from multiple predators, known as multiple predator effects (MPEs). There are very few empirical studies that examine higher-order interactions that result from three or more predators, and even fewer that examine the entire factorial of combinations (single predator effects, all pairwise effects, and a three-predator effect). Indeed, we could find only three such studies, and these studies involved a single prey species [144–146]. In MPE studies that look for interactions among three predators, multiplicative models are typically used and are equivalent to the deviation from additivity (DA) measure, where the fitness parameters are survival rates [144–147]. However, as discussed throughout this paper, DA is not capable of distinguishing truly emergent interactions that require all three predators and do not arise from pairwise interactions. Moreover, these studies have no equivalent method to our E3 measure for quantifying and identifying emergent interactions. In this sense, the generalized emergent measure (E3) we propose here should be highly informative in deciding whether complex predator-prey relationships are actually a result of subsets of simpler interactions (with less components). Indeed, recent work by Cheng et al. [148] shows the importance of subsets of three-way interactions for understanding emergence in a five species predator-prey model and suggests similar approaches may be fruitful.

Applying these ideas to ecological systems, however, will also require additional considerations. For example, Barrios-O'Neill and colleagues examined how multiple predators affect prey when the predators are of different trophic levels and are allowed to evolve [35]. They found that when there is a secondary predator one trophic level up, MPEs behave differently when involving native versus invasive predators, demonstrating how predator-prey systems and food web dynamics are often more complex than the interactions presented here using drugs and bacteria. We recognize this as a limitation of our system being applied to ecological questions that involve multiple species and trophic levels because our study involves only one species and one trophic level of "predator" (antibiotics). Furthermore, antibiotics do not evolve in the ways predators do, thus simplifying our system but also limiting its generality. Nevertheless, we suggest that the measure derived here could aid in the quantification of interactions among large numbers of species, but careful reasoning needs to be applied to interpret the results for macro-organism studies on predator-prey interactions that contain a larger variety of behaviors and responses.

Although applying this framework across other systems will require further work, we can already identify intriguing connections between the E3 measure developed here and formulas from other fields. It is analogous to theoretical physics concepts such as the 3-point connected correlation or Ursell function in quantum field theory, and the third joint cumulant in statistical physics and statistics [149, 150]. However, our measure differs from these because it is not defined with respect to expectation values, and the combination of two variables is through addition and not multiplication. In the previously mentioned work by Wood et al. [13], they insightfully noticed that their maximum entropy calculations for determining interaction type were well described by a simple algebraic formula that they identified as the Isserlis theorem. In the case of three-way interactions, this formula can be re-expressed to show its equivalence to our emergent interaction measure E3. However, these two approaches yield substantially different interaction metrics for characterizing four-way (or higher) interactions since our method naturally includes all possible lower-order effects in the metric, whereas Wood and colleagues considered only pairwise and single drug effects (see Supplementary Text 1). Importantly, Wood et al. found this formula phenomenologically by using a computational Maximum Entropy method [13] but did not provide a general derivation as above. Lastly, based on our starting definition of no interaction (i.e., Bliss independence), standard three-way ANOVA (even when log transformed) is not equivalent to our correct measure of emergent interactions (see Supplementary Text 2 and Supplementary Table 3).

In summary, we provide a tool for defining emergent interactions of multiple stressors. In the past, statistical methods, such as ANOVA and Maximum Entropy [13, 30, 144, 151], have been used to search for interactions. The advantage of our approach to understand higher-order emergent interactions by deriving a simple algebraic formula is that it: i) explicitly distinguishes between net and emergent interactions, ii) decomposes the interaction into its natural component pieces with exactly specified and empirically measurable coefficients (e.g., single drug fitnesses) instead of an increasing number of free parameters that require fitting, iii) greatly simplifies calculations, helping to avoid technical mistakes and rounding errors while also taking less time computationally, iv) leads to re-scaling that allows consistency with previous pairwise analyses [16] and clearer identification of interactions, and v) naturally generalizes to higher-order interactions in a way that unambiguously incorporates the effects of all combinations of subsets of components. In conclusion, using our framework to analyze higher-order interactions may be important for revealing emergent properties in medical, environmental, and ecological systems.

## 2.5 Acknowledgements

We thank Tina Manzhu Kang and Borna Shirvani for assistance in the lab, and Alex Hall, Daniel Barrios-O'Neill and three anonymous reviewers through Axios Review for comments on the manuscript.

# CHAPTER 3

# Enhanced Identification of Synergistic and Antagonistic Emergent Interactions Among Three or More Drugs

## 3.1 Introduction

Multi-drug treatments are an important tool [68, 112, 152–154], in particular for combatting bacteria that are highly resistant to the individual use of traditional antibiotics [3, 28, 108, 155–157]. The efficacy and efficiency of these combination therapies is substantially affected by how the specific drugs interact. Thus, a useful categorization scheme for interactions is needed that uses the additive case [28, 29, 110]—drugs do not interact at all—as a baseline. Along with this is the concept of emergence—effects of drug combinations that cannot be predicted from lower-order interactions among subsets of the drugs [26]. Relative to these baselines, interactions are generally categorized as a type of synergy if the combination kills more efficiently than is expected from the additive case or from lower-order interactions (Fig. 3.1). Conversely, when the drug interaction reduces the effect of each drug, the interaction is called antagonistic (Fig. 3.1), which itself contains special cases: i) buffering, in which one drug completely masks the effect of the other drug, and ii) suppression, in which the effectiveness of the drugs in combination is weaker than at least one drug by itself [3, 37, 158]

**Figure 3.1: Schematic illustration of triple-drug interactions.** Interactions are determined based on measurements of bacterial growth and interactions of all components: single drugs of $X$, $Y$, $Z$, pairwise combinations of $XY$, $YZ$, and $XZ$, and triple-drug combination of $XYZ$. Pairwise interactions of synergistic ($XY$), additive ($YZ$), and antagonistic ($XZ$) are marked with red, black, and green respectively, while the triple interaction is colored as dashed gray to depict the uncertainty of the interaction.

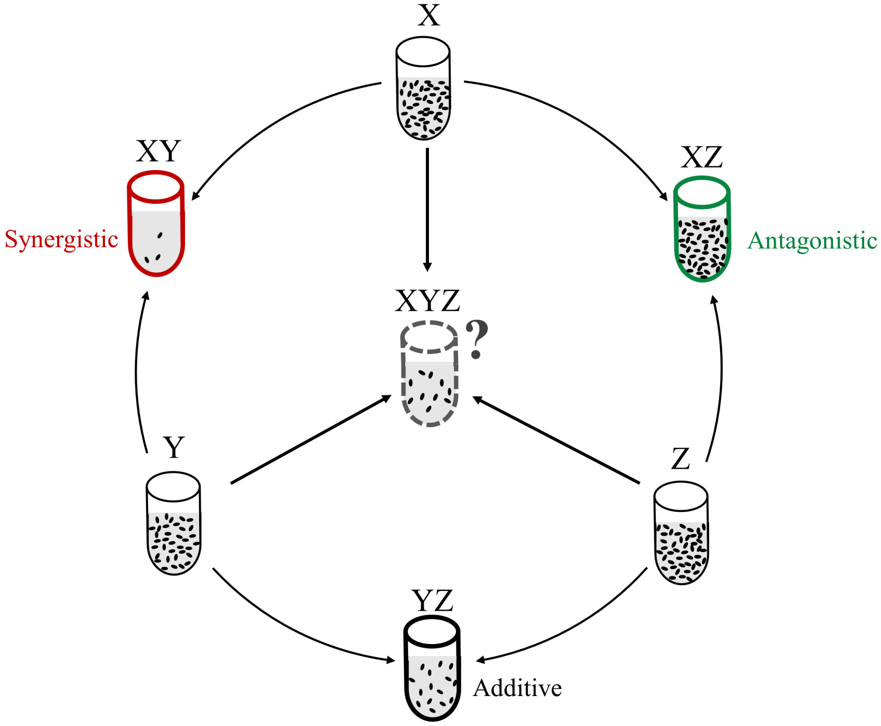

Multi-drug treatments are an important tool [68, 112, 152–154], in particular for combatting bacteria that are highly resistant to the individual use of traditional antibiotics [3, 28, 108, 155–157]. The efficacy and efficiency of these combination therapies is substantially affected by how the specific drugs interact. Thus, a useful categorization scheme for interactions is needed that uses the additive case [28, 29, 110]—drugs do not interact at all—as a baseline. Along with this is the concept of emergence—effects of drug combinations that cannot be predicted from lower-order interactions among subsets of the drugs [26]. Relative to these baselines, interactions are generally categorized as a type of synergy if the combination kills more efficiently than is expected from the additive case or from lower-order interactions (Fig. 3.1). Conversely, when the drug interaction reduces the effect of each drug, the interaction is called antagonistic (Fig. 3.1), which itself contains special cases: i) buffering, in which one drug completely masks the effect of the other drug, and ii) suppression, in which the effectiveness of the drugs in combination is weaker than at least one drug by itself [3,36,37,158].

It is a challenge to quantify interactions with a metric that has clear boundaries between these cases and effectively identifies and distinguishes between interaction types. Overcoming this challenge often requires a rescaling or normalization of basic metrics, and for pairwise interactions, some effective methods have been discovered [3,16,65,159]. Rescaling for combinations of more than two drugs has previously been done using the most straightforward generalization of the pairwise method [26,62], but unlike the pairwise case, there are several possibilities for rescaling metrics for higher-order interactions, even among three drugs. Here, we explore these possible rescalings and identify the one that is best at categorizing and thus distinguishing among three-drug interactions. Importantly, this particular rescaling method is different than the rescaling previously used in the literature by ourselves and others. Consequently, this could reveal new insights for interactions among three or more drugs, as well as other objects such as proteins [31] and predators [30,144–146,160], and some existing results may need to be revisited and revised [13,26].

For the case of two drugs, there are two common methods to analyze and categorize interactions. First, Loewe Additivity categorizes the interaction based on the strength of inhibition on bacterial growth when drug concentrations are varied simultaneously [29]. When the same effective concentration (relative to each drug's Minimum Inhibitory Concentration) of the two drugs kill bacteria at a rate that is independent of the relative fractions of each drug, the interaction is regarded as additive. This Loewe measure is motivated by the simplest case in which a drug does not interact with itself. Depending on the direction of the divergence from this additive case, the relationship is considered as either synergy or antagonism.

Second, Bliss Independence (BI) defines additivity to be the case when the presence of one drug does not affect another drug's percent reduction of bacterial growth rate [28]. This definition breaks down if one of the drugs and the pairwise combination are both lethal such that bacteria cannot grow. Interactions are antagonistic according to BI when the deviation from this additive (DA) case is positive and are synergistic when DA is negative [3,16]. Bliss Independence offers a simple measurement of the epistatic interactions because it relies on less data and its results are more easily calculable and interpretable [37].

DA measures yield a unimodal distribution around the additive case for drug interactions. Because of the unimodal shape, it is challenging to delineate boundaries and tease apart synergistic, additive, and antagonistic cases. To overcome this hurdle, a rescaling method of the DA measure was proposed in Segre et al. [16] for pairwise interactions. The rescaling normalizes DA with respect to the pairwise drug fitness for two reference cases: lethal synergy and complete buffering (i.e., the combined two drugs have the same effect as the strongest single drug alone). This rescaled form of DA leads to an interaction distribution that exhibits three dominant peaks, with clear spacing between them, hereafter referred to as a trimodal distribution. For both simulated and empirical results, these peaks enable a straightforward separation among synergistic, antagonistic, and additive interactions [3, 16, 65, 159]. These peaks are observed at the exact location expected theoretically.

Given that higher-order ($> 2$) drug combinations are increasingly being used to combat drug-resistant pathogens, it is important to have similarly effective, though not necessarily similar in form, rescaled measures for higher-order interactions within a complex environment. This is a complicated task, because effects at all levels—single drug, pairwise combination, triple combination, etc.—may need to be taken into account (Fig. 3.1). For example, a three-drug combination could have interactions arising from the three different pairwise combinations as well as an interaction that only emerges when all three drugs are present. Recently, a novel method to characterize and quantify emergent interactions in three-drug combinations has been introduced. Beppler et al. [26] present a framework that compares the higher-order interaction with expectations based on its lower-order component interactions. First, the direct extension of the DA metric allows identification of three-drug interaction compared solely to the single-drug effects [26, 62, 69]. Next, the new emergent three-way interaction (E3) incorporates the pairwise interactions in the model and determines the effect of three-drug interaction that is beyond the effects from all two-drug combinations. The generalization of the interaction formulas for combinations of more than three drugs are followed by the conceptual derivation of each metric, and the special case with four drugs is provided in Beppler et al. [26]. Moreover, a recent numerical model by Wood et al. [13] used maximum entropy estimation to predict the higher-order effects relative to single and pairwise drug effects for any number of drug combinations. They showed that their numerical estimation is consistent with an algebraic expression that is equivalent to E3 for three-drug combinations. However, our emergent $N$-way interaction metric differs from Wood et al.'s model in the sense that it quantifies the deviations from the expectations from all lower-order effects, not just pairwise effects, so for more than four drugs, our model and Wood et al.'s model will differ.

In this paper, we show that there are several choices for rescaling emergent interactions and that the specific choice of rescaling plays a crucial role in identifying interactions among drugs. We analyze the previously defined rescaling method—direct extension of the two-drug rescaling—of the emergent three-way measure and establish new rescaling methods that greatly improve the characterization of emergent properties. These methods are defined by exploring possible reference cases of synergy and antagonism that arise with higher-order drug combinations. Lethality always serves the reference case for synergies since it offers the most extreme case of synergism regardless of number of drugs in the environment. Therefore, there is only one simple extension of the rescaling method for two-drug combinations for synergies. However, for antagonistically interacting drugs, the definition for the reference case of complete buffering could vary based on the drug system and also the interaction metric (DA versus E3). Because DA quantifies the overall interaction with respect to individual drug effects, the strongest single-drug effect defines the complete buffering case as in the two-drug system. However, for the emergent interaction, it matters whether the buffering is defined relative to some subset or to all of the lower-order drug combinations (single drug, two drug, or some combination). Our new rescaling methods cover the possibilities for the definition of the antagonistic buffering, and our evaluation of these possibilities eventually leads to enhanced classification of the emergent interaction.

To empirically study whether these different scaling methods effectively separate the histogram for the metric into a trimodal distribution, making it straightforward to separate synergy, additivity, and antagonism, we selected 14 antibiotics and systematically investigated the effects of three-drug combinations on the growth rate of a bacteria, wild-type *Escherichia coli*. These data allow us to apply several rescaling methods and hence to identify which method is best at distinguishing among interactions for three-drug combinations and emergent interactions. We further apply our rescaling analysis to the three-antibiotic combination data presented in Wood et al. [13]. We compare the original analysis in the Wood et al. paper [13] with the new analysis from our rescaling method. Finally, we present a straightforward generalization of our new rescaling methods to emergent interactions that involve more than three drugs.

## 3.2 Materials and Methods

### 3.2.1 Experimental details

**Bacteria.** The bacteria used in these experiments was the *E. coli* strain BW25113, the wild-type strain ($lacI^q$ $rrnB_{T14}$ $\Delta lacZ_{WJ16}$ $hsdR514$ $\Delta araBAD_{AH33}$ $\Delta rhaBAD_{LD78}$) [134] derived from the strain W1485 background [135]. A single colony was used to inoculate cultures for glycerol stocks stored at -80°C. A single colony from this glycerol culture was used to inoculate cultures in LB media (10 g/l tryptone, 5 g/l yeast extract, and 10 g/l NaCl). These cultures were resuspended in MC buffer and stored at 4°C. Bacteria for experiments were grown by inoculating 20 $\mu$l of the MC stock into 2 ml LB daily and growing for 5 hours at 37°C. 25 $\mu$l of a $10^{-4}$ dilution of this culture in LB was used to inoculate into 975 $\mu$l cultures for experiments.

**Antibiotics.** Antibiotics used include clindamycin hydrochloride (Sigma C-5269), chloramphenicol succinate sodium salt (Sigma C3787), fusidic acid sodium salt (Sigma F0881), erythromycin (Sigma Aldrich E-6376), ciprofloxacin hydrochloride (MP Biomedicals 199020), cefoxitin sodium salt (Fluka C4786), ampicillin (Sigma A9518), nitrofurantoin (Sigma N7878), trimethoprim (Sigma T7883), tobramycin sulfate (Sigma T-1783), streptomycin sulfate (Sigma Aldrich S-6501), gentamicin sulfate salt (Sigma G1264), vancomycin hydrochloride (Sigma

| Drug | Abbreviation | Dose Range ($\mu$ g ml$^{-1}$) | Main Mechanism(s) of Action |
|---|---|---|---|
| Clindamycin | CLI | 17.5-31.5 | Protein synthesis, 50S |
| Chloramphenicol | CHL | 38-70 | Protein synthesis, 50S |
| Fusidic Acid | FUS | 75-110 | Protein synthesis, 50S |
| Erythromycin | ERY | 12-30 | Protein synthesis, 50S |
| Ciprofloxacin | CPR | 0.009-0.013 | DNA gyrase |
| Cefoxitin | FOX | 0.90-1.16 | Cell wall |
| Ampicillin | AMP | 0.9-1.3 | Cell wall |
| Nitrofurantoin | NTR | 1-3 | Multiple Mechanisms |
| Trimethoprim | TMP | 0.06-0.08 | Folic acid biosynthesis |
| Tobramycin | TOB | 0.5-1.3 | Aminoglycoside, protein synthesis, 30S |
| Streptomycin | STR | 1.0-5.0 | Aminoglycoside, protein synthesis, 30S |
| Gentamicin | GEN | 0.04-0.40 | Protein synthesis, 30S |
| Vancomycin | VAN | 35-75 | Protein synthesis, 30S |
| Doxycycline | DOX | 0.40-0.65 | Protein synthesis, 30S |

**Table 3.1:** List of all antibiotics used in the study, abbreviation, dose range, and mechanism of action.

V2002), and doxycycline hyclate (Sigma D9891). The dosage, mechanism of action, and abbreviations of these antibiotics are given in Table 3.1.

**Growth experiments.** Antibiotic concentrations were chosen to reduce growth by 15-35% as compared to the no-drug control (LB). These sub-lethal dosages were first determined by testing a range of concentrations for each antibiotic and were then used in all single-drug, two-drug, and three-drug conditions. Each triple-drug experiment included a no-drug control, three single-drug conditions, three two-drug conditions, and the three-drug combination. In all cases, antibiotics were added to the previously determined sub-lethal concentrations in 1 ml LB and inoculated as described above. 100 $\mu$l was aliquoted into 4-6 wells for each condition in a 96-well plate. These cultures were grown overnight for 18 hours at 215 rpm and 37°C. Optical density readings at 600 nm ($OD_{600}$) at 18 hr were used to calculate growth rates as compared to the no-drug control at 18 hr by taking their ratios at this time point. This procedure has been previously used by us [161] and others [162, 163]. Each three-drug experiment was repeated at least three times. Data are represented as median ± maximum/minimum.

Growth experiment data were also obtained from Wood et al. [13], and methods for those empirical measurements are detailed in that paper. Here, the Wood et al. triple-drug combination data (with non-zero concentration for each drug in the combination) are analyzed using the exact same analytical DA and E3 measures, calculations, and cutoffs for significance (all these methods are explained in the subsequent sections) as for our empirical data.

**Definition of lethal.** Lethal antibiotic concentrations are all concentrations above which no bacterial growth can be measured. Experiments were performed to determine the maximum $OD_{600}$ measurements with error that represent the lethal case. Bacteria for these experiments were grown and inoculated in 96-well plates in the same manner as described above. Three conditions were tested: LB only (no cells), LB + cells, and LB + streptomycin (STR) 9.2 g/ml + cells. STR 9.2 g/ml was chosen as an extremely high antibiotic concentration that would ensure no bacterial growth, even when the populations were re-inoculated in no-drug environments. Thus, the LB only (no cells) and the LB + STR 9.2 g/ml + cells conditions could be used to determine the error in $OD_{600}$ measurements that represent no bacterial growth. The LB + cells condition was used as the positive control and 100% growth reference point. The LB only and LB + cells conditions were each replicated in 16 wells. The LB + STR 9.2 g/ml + cells condition was replicated in 64 wells. After 18 hours of growth at 37°C and 215 rpm, the $OD_{600}$ measurements were gathered. From these extremely high drug concentrations as well as populations with no bacterial at all, we obtained mean $OD_{600}$ measurements of 0.044 with an error of 0.003. In addition, we further tested bacteria populations at low OD, but above 0.047, to confirm that those populations continued to grow (Supplementary Fig. 1). Thus, all growth measurements below 0.047 represent lethal cases.

Based on the analysis of the emergent three-way measure (E3), we find that when the three-drug combination and one of the pairwise combinations are both lethal, the rescaled E3 measure identifies the emergent interaction as either antagonistic buffering or lethal synergy. This situation is consistent with both definitions. However, unless the three-drug combination is chosen to be non-lethal, the effect of the third drug on the outcome is not obvious as the pairwise combination already represents lethality. For this reason, we identified all such cases as inconclusive, which is consistent with previous work on large drug interaction networks (e.g. Yeh et al. [3]).

**Cutoff values for the rescaled emergent interaction measure.** Based on previous work [3, 26] and the analysis of the resulting distributions of $[\mathrm{E3}]_{\mathrm{R2}}$ over all the drug triples (see Model Framework and Results), the interaction is identified as synergistic when rescaled E3 is less than $-0.5$, antagonistic if it is greater than 0.5, and additive otherwise. For antagonistically identified triples, we further choose 1.3 as the cut-off between the special cases of buffering and suppression.

### 3.2.2 Model framework

**Three-way interaction measures.** In general, a measure of the efficacy of a treatment is how much it inhibits bacterial growth rate relative to growth in the absence of drugs. This measure is equivalent to a relative fitness for the bacteria that is typically denoted by $w_D$, where D stands for a single drug or a mixture of several drugs. Here, the fitness measures are symmetric in the ordering of drug indices, for example $w_{XY} = w_{YX}$ for drugs X and Y. As discussed in the Introduction, Bliss Independence is when the percent reduction in growth rate by a single drug is independent of the presence of other drugs and is expressed in an equation as $w_{XY} = w_X w_Y$ [28]. Accordingly, the deviation from additivity (DA) is defined by $\mathrm{DA}_{X,Y} \equiv w_{XY} - w_X w_Y$, with the general interpretation that a large enough negative value of $\mathrm{DA}_{X,Y}$ implies synergy between drugs, such that the combined effect is greater than would be predicted based on the single effects. Conversely, a large enough positive $\mathrm{DA}_{X,Y}$ means that the drugs are acting antagonistically.

Identifying the existence of some type of interaction among more than two drugs can be defined analogously (i.e., via generalization of DA). For three drugs, the DA measure becomes: $\mathrm{DA}_{X,Y,Z} \equiv w_{XYZ} - w_X w_Y w_Z$, quantifying interactions at any level that contribute to the overall interaction [13, 26, 62, 69]. With more sophisticated modeling and measures, it is also possible to identify true emergence—the overall interaction is not just a result of interactions among subsets of the drugs. That is, it is important to distinguish between effects that arise from lower-order interactions (such as pairwise interactions that yield an apparent three-way effect) and those that arise from emergent interactions that require all of the drugs to be present to manifest their unified effect in killing bacteria. A recent model that is capable of making this distinction was introduced [26] and was termed the E3 measure.

The logic of the E3 measure is that all possible pairwise contributions are correctly weighted and subtracted from the overall interaction; hence it quantifies any triple-drug interaction that does not originate from the pairwise interactions. The weighting is determined based on the expected three-way effect when only two drugs (pairwise interaction $X$ and $Y$) interact and the third drug ($Z$) is additive with them. Based on the three-way DA measure, this would give an effect of $w_Z \mathrm{DA}_{X,Y}$ because $w_Z$ would factor from all terms and the remaining terms are just the definition of the pairwise DA measure. For three drugs, there are three pairwise combinations, so subtracting all possible pairwise combinations yields:

$$\mathrm{E3} = \mathrm{DA}_{X,Y,Z} - w_X \mathrm{DA}_{Y,Z} - w_Y \mathrm{DA}_{X,Z} - w_Z \mathrm{DA}_{X,Y} \tag{3.2.1}$$

Rewriting this equation solely in terms of the relative fitness gives

$$\mathrm{E3} = w_{XYZ} - w_X w_{YZ} - w_Y w_{XZ} - w_Z w_{XY} + 2 w_X w_Y w_Z \tag{3.2.2}$$

Notably, this E3 measure includes every possible relative fitness in the three-drug system. Both the E3 and DA measures are symmetric in drugs $X$, $Y$, and $Z$ and can be easily adapted to higher-order interactions that involve more than three drugs. More detailed discussion of the derivation of higher-order interaction metrics can be found in Beppler et al. [26].

**Rescaling three-way interaction measures.**

To easily quantify the interaction strength and the separation of interaction classes, the interaction measure must be rescaled. For pairwise interactions, Segre et al. [16] established a rescaling method that greatly enhances the discovery of antagonism. Their normalization is based on two limiting reference cases for the synergistically and antagonistically interacting drug pairs. The normalization factor for synergy is defined by substituting the lethal case into the DA measure (i.e., DA $= |0 - w_X w_Y| = w_X w_Y$), whereas the antagonistic interaction is rescaled by the complete buffering case in which the two-drug effect is the same as the fitness of the single drug with the stronger effect (i.e., DA $= |\min(w_X, w_Y) - w_X w_Y|$). With this rescaling the pairwise interactions yield a trimodal distribution centered on these reference cases (modes at $-1$, 0, and 1 as expected theoretically) and provides a clear cutoff between synergistic, additive, and antagonistic interactions [3, 16, 65, 164].

To classify interactions among three-drug combinations, we also need to establish an appropriate rescaling or normalization. In particular, the reference cases for negative and positive measures must be properly defined for each triple-drug interaction measure. It is expected that there is a biologically- and empirically-grounded choice of rescaling that will provide a clear distinction between the interaction classes, as in the case with two drugs. Moreover, as our rescaling measures are based on special cases of the DA or E3 measures, they are symmetric by construction.

The case of lethality is uniquely defined for each three-way interaction measure. On the other hand, buffering can be defined in several different ways, and the choice of definition may depend on the type of interaction measure (emergent versus overall) being considered. Because DA quantifies the deviations from the case that all single-drug effects are combined additively, it is practical to define buffering with respect to the effect of the strongest individual drug. However, the definition of buffering for the emergent three-way interaction (E3) is not unique because E3 captures the effect of the three-drug combination relative to all lower-order effects. Hence, buffering could be defined relative to the strongest individual drug, the strongest pairwise effect, or the strongest of all of these. As a result of this ambiguity, the choice of rescaling might cause misidentification of antagonism. In the subsequent sections, we first present the extension of the two-drug rescaling method to three-way interaction measures, and then construct new rescaling factors that will help to more comprehensively evaluate and characterize the emergent properties of drug combinations.

**Extension of two-drug rescaling method (termed "Rescale 0") .**

Beppler et al. [26] and Sanjuan et al. [62] introduced a rescaling that directly extends the method of Segre et al. [16]. Negative measures are scaled relative to extreme lethal synergy such that the triple-drug combination kills off the bacteria, i.e. $w_{XYZ} = 0$. When the interaction measure is positive, it is scaled with respect to the buffering case defined to be when the fitness of bacteria exposed to the triple-drug combination is the same as when exposed to just the single drug with the strongest efficacy, i.e. $w_{XYZ} = \min(w_X, w_Y, w_Z)$ . Hence, the normalization factor (Scale 0, denoted by S0) for the positive E3 measure is defined by

$$\mathrm{S0} = |\min(w_X, w_Y, w_Z) - w_X w_{YZ} - w_Y w_{XZ} - w_Z w_{XY} + 2 w_X w_Y w_Z|$$

Then, the rescaled E3 measure with S0 (Rescale 0) takes the form

$$[\mathrm{E3}]_{\mathrm{R0}} = \frac{w_{XYZ} - w_X w_{YZ} - w_Y w_{XZ} - w_Z w_{XY} + 2 w_X w_Y w_Z}{|\min(w_X, w_Y, w_Z) - w_X w_{YZ} - w_Y w_{XZ} - w_Z w_{XY} + 2 w_X w_Y w_Z|}$$

Based on the discussion above, the current published rescaling method [16, 26, 62] is the most appropriate way of characterizing interaction type based on the DA measure and the synergistic emergent interactions.

### New rescaling methods for emergent three-way interaction (E3).

To explore alternative rescaling methods that may lead to a clearer identification of antagonistic interactions, we revisit the possible definitions of buffering. Based on the buffering definition, the antagonistic buffering cases would be mapped to 1 via the corresponding rescaled metric. Note that the synergistic interactions are characterized by the previously defined rescaling method; hence rescaling methods presented here map the lethal synergies to $-1$. All of the different rescaling methods are summarized in Table 2.

### Rescale 1—Buffering relative to pairwise drug effects.

Higher-order combination therapies of $N$ drugs are analyzed relative to the lower-order combinations (i.e., $N-1$, $N-2$, etc.) of subsets of the drugs. Therefore, another type of buffering is when the effect of all three drugs combined is exactly the same as that of the most powerful pairwise combination (i.e., the lowest relative fitness in the presence of any pairwise combination of drugs). Consequently, for antagonistically interacting drugs (i.e., E3> 0), we introduce the normalization factor S1 by substituting the minimum of all pairwise drug fitnesses for the triple-drug fitness in E3 (Table 2).

$$\mathrm{S1} = |\min\left(w_{XY}, w_{XZ}, w_{YZ}\right) - w_X w_{YZ} - w_Y w_{XZ} - w_Z w_{XY} + 2 w_X w_Y w_Z|$$

Hence, the rescaled E3 measure (Rescale 1) is

$$[\mathrm{E3}]_{\mathrm{R1}} = \frac{w_{XYZ} - w_X w_{YZ} - w_Y w_{XZ} - w_Z w_{XY} + 2 w_X w_Y w_Z}{|\min\left(w_{XY}, w_{XZ}, w_{YZ}\right) - w_X w_{YZ} - w_Y w_{XZ} - w_Z w_{XY} + 2 w_X w_Y w_Z|}$$

In this way, we can assess if any of the pairwise drug combinations disguise the effect of the cooperation and antagonism of the remaining drug in the triple-drug combination.

**Rescale 2—Buffering relative to single and pairwise drug effects.**

In this section, we propose a generalization of the above S1-rescaling scheme that accounts for *all* lower-order drug components. This generalization allows for the possibility that a single-drug therapy might be more powerful and offer more effective treatment than any pairwise combination (i.e., the lowest relative fitness in the presence of a single drug is lower than the relative fitness in the presence of any pairwise combination). This extension defines the E3 measure relative to the minimum of the fitness values attained by any single or pairwise components as

$$\mathrm{S2} = |\min\left(w_{XY}, w_{XZ}, w_{YZ}, w_{XY}, w_{XZ}, w_{YZ}\right) - w_X w_{YZ} - w_Y w_{XZ} - w_Z w_{XY} + 2 w_X w_Y w_Z|$$

(Table 2). Thus, the new rescaled E3 measure (Rescale 2) takes the form

$$[\mathrm{E3}]_{\mathrm{R2}} = \frac{w_{XYZ} - w_X w_{YZ} - w_Y w_{XZ} - w_Z w_{XY} + 2 w_X w_Y w_Z}{|\min\left(w_{XY}, w_{XZ}, w_{YZ}, w_{XY}, w_{XZ}, w_{YZ}\right) - w_X w_{YZ} - w_Y w_{XZ} - w_Z w_{XY} + 2 w_X w_Y w_Z|}$$

Rescale 1 and 2 yield the same results if the minimum of the pairwise drug fitnesses is less than the minimum of the single-drug fitnesses, which is frequently the case. Notably, Unscaled metric

$$\text{E3} \; = \; \text{DA}_{X,Y,Z} \; - \; w_X \text{DA}_{Y,Z} \; - \; w_Y \text{DA}_{X,Z} \; - \; w_Z \text{DA}_{X,Y}$$

or

$$\text{E3} \; = \; w_{XYZ} \; - \; w_{XY} \; - \; w_{XZ} \; - \; w_{YZ} \; + \; 2 w_X w_Y w_Z$$

Rescaled metric

$$[\text{E3}]_{Ri} \; = \; \frac{w_{XYZ} - w_{XY} - w_{XZ} - w_{YZ} + 2 w_X w_Y w_Z}{|\widetilde{w}_{XYZ} - w_{XY} - w_{XZ} - w_{YZ} + 2 w_X w_Y w_Z|}$$

| | E3 $\leq 0$<br>rescale with respect to<br>the lethality<br>$[\text{E3}]_{\text{R}i} \sim -1$ | E3$> 0$<br>rescale with respect to<br>the antagonistic buffering<br>$[\text{E3}]_{\text{R}i} \sim 1$ |
|---|---|---|
| Rescale 0 | $\tilde{w}_{XYZ} = 0$ | $\tilde{w}_{XYZ} = min\,(w_X, w_Y, w_Z)$ |
| Rescale 1 | $\tilde{w}_{XYZ} = 0$ | $\tilde{w}_{XYZ} = min\,(w_{XY}, w_{XZ}, w_{YZ})$ |
| Rescale 2 | $\tilde{w}_{XYZ} = 0$ | $\tilde{w}_{XYZ} = min\,(w_X, w_Y, w_Z, w_{XY}, w_{XZ}, w_{YZ})$ |
| Rescale 3 | $\tilde{w}_{XYZ} = 0$ | $\tilde{w}_{XYZ} = min\,(w_X w_{YZ}, w_Y w_{XZ}, w_Z w_{XY})$ |

**Table 3.2:** Unscaled and rescaled definitions of emergent three-way interaction (E3)

Rescale 2 spans a broader set of circumstances than Rescale 1.

We further note that it is straightforward to generalize Rescale 2 when emergent properties with more than three drugs are analyzed. For the case of N drugs, the scaling factor S2 is given by calculating the emergent measure by replacing the N-drug fitness by the minimum of the bacterial fitness among all possible subsets of the drugs. For instance, 4-drug combinations are rescaled relative to the case when $w_{XYZT} = \min(w_X, w_Y, w_Z, w_T, w_{XY}, w_{XZ}, w_{XT}, w_{YZ}, w_{YT}, w_{ZT}, w_{XYZ}, w_{XYT}, w_{XZT}, w_{YZT})$.

**Rescale 3—Buffering relative to effects from pairwise interactions.**

Because the E3 measure captures the emergent triple-drug interaction that cannot be explained by the pairwise effects, we consider another definition of buffering to be relative to the expected pairwise contribution to the overall three-way interaction (DA). Note that based on the DA and E3 measures, this is not the same as the relative fitness in the presence of a pairwise drug combination because each of those relative fitness is multiplied by the proper weighting (i.e., the relative fitness in the presence of the remaining single drug). Replacing the DA term ($\mathrm{DA}_{X,Y,Z}$) in the E3 expression (3.2.1) by the minimum of pairwise interaction contributions defines our last scaling method, S3, via

$$\mathrm{S3} = \left|\min\left(w_X \mathrm{DA}_{Y,Z}, w_Y \mathrm{DA}_{X,Z}, w_Z \mathrm{DA}_{X,Y}\right) - w_X \mathrm{DA}_{Y,Z} - w_Y \mathrm{DA}_{X,Z} - w_Z \mathrm{DA}_{X,Y}\right|$$

Substituting the pairwise fitness measures into the minimized quantity in S3, we obtain

$$\min\left(w_X \mathrm{DA}_{Y,Z}, w_Y \mathrm{DA}_{X,Z}, w_Z \mathrm{DA}_{X,Y}\right) = \min\left(w_X w_{YZ},\; w_Y w_{XZ}, w_Z w_{XY}\right) - w_X w_Y w_Z$$

which is a symmetric expression in terms of the pairwise contributions. S3 can be expressed purely in terms of the fitness parameters as

$$\mathrm{S3} = \left|\min\left(w_X w_{YZ},\; w_Y w_{XZ}, w_Z w_{XY}\right) - w_X w_{YZ} - w_Y w_{XZ} - w_Z w_{XY} + 2 w_X w_Y w_Z\right|$$

so when the unscaled E3 measure is positive, we rescale the E3 measure (Rescale 3) as

$$[\mathrm{E3}]_{\mathrm{R3}} = \frac{w_{XYZ} - w_X w_{YZ} - w_Y w_{XZ} - w_Z w_{XY} + 2 w_X w_Y w_Z}{\left|\min\left(w_X w_{YZ},\; w_Y w_{XZ}, w_Z w_{XY}\right) - w_X w_{YZ} - w_Y w_{XZ} - w_Z w_{XY} + 2 w_X w_Y w_Z\right|}$$

(Table 2). Because experimental concentrations of individual drugs are chosen such that each reduces the growth about 15-35%, we expect somewhat similar results as in the Rescale 1 because we are simply multiplying $w_{XYZ} = \min\left(w_{XY}, w_{XZ}, w_{YZ}\right)$ by a number between 0.6 and 0.9 (relative fitness of a single drug).

## 3.3 Results

To distinguish different types of interactions manifested in triple-drug combination therapies, we utilize a newly proposed emergent three-way measure [26]. To include as much information as possible, we show all data in the histogram results (Fig. 3.2). We observe that the unscaled version of the emergent measure yields a unimodal distribution around the additive case (Fig. 3.2a). We find that Rescale 0 which defines buffering based on the comparison of triple drug combination with the single drug effects (previously used method in [26, 62]) results in a distribution with modes at $-1$ and 0, hence identifying emergent synergies. Yet, Rescale 0 does not result in a clear distinction for the antagonistic triples (Fig. 3.2c).

**Figure 3.2: The histogram of the unscaled emergent three-way measure (E3) over all triple-drug combinations.** The stacked bars with different colors on the histogram represent synergistic (red), additive (black), antagonistic buffering (green), and antagonistic suppression (blue) triples identified via Rescale 2. **(b)** The histogram of the scaled emergent three-way measure via Rescale 2, i.e. $[\mathrm{E3}]_{\mathrm{R2}}$. The plot shows a multi-modal distribution with modes at synergistic, additive, and antagonistic buffering. Cutoffs can be placed between these modes to categorize interactions. **(c-d-e)** The histogram of the scaled emergent three-way measure via Rescale 0, 1 and 3, i.e. $[\mathrm{E3}]_{\mathrm{R0}}$, $[\mathrm{E3}]_{\mathrm{R1}}$ and $[\mathrm{E3}]_{\mathrm{R3}}$.

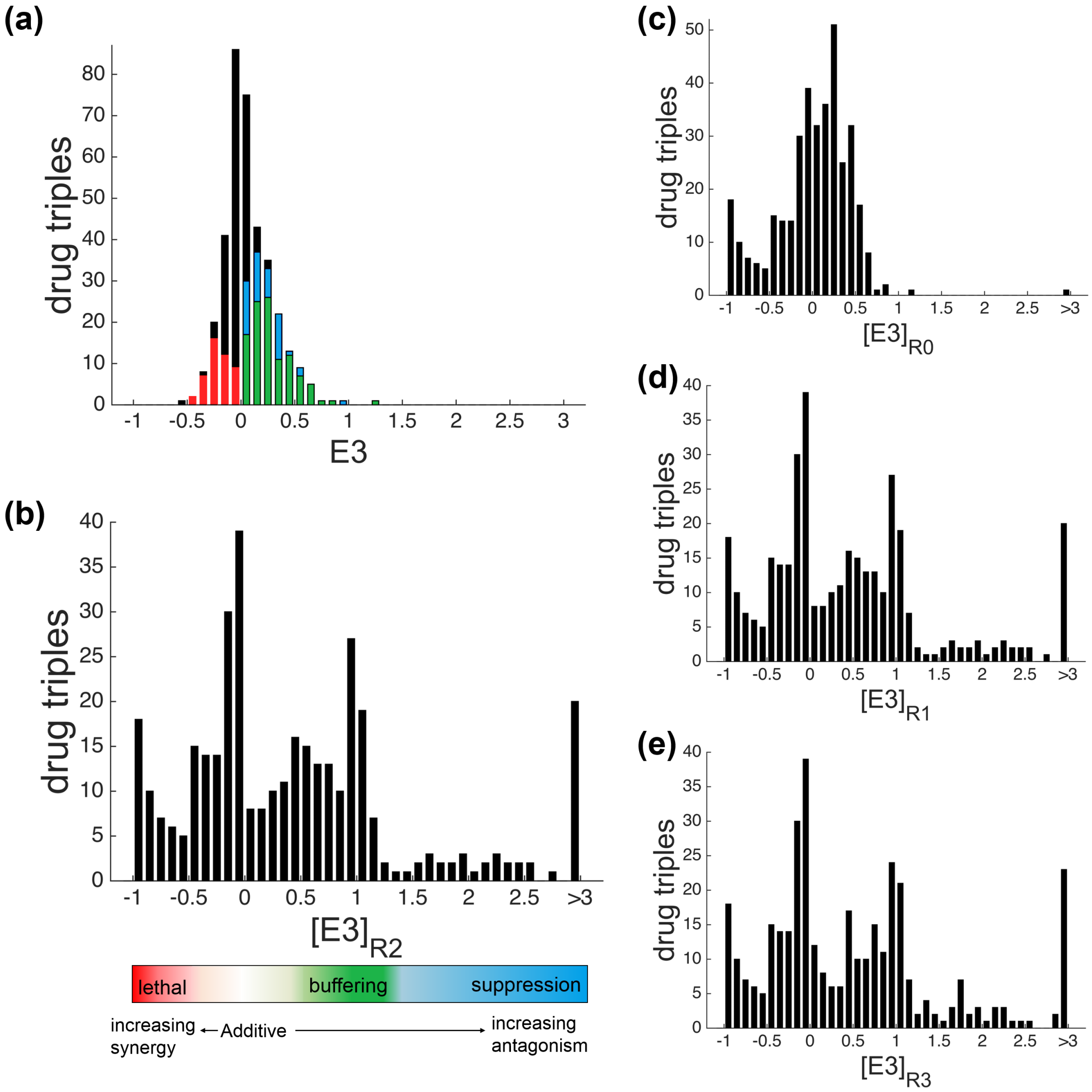

Importantly, using the new rescaling methods we propose here, we see that Rescale 2, which defines antagonistic buffering relative to the single or pairwise drug effects, successfully maps (Fig. 3.2b) lethal synergies to $-1$, additive interactions to 0, and the antagonistic buffering interactions to 1. Consequently, the resulting distribution from Rescale 2 leads to a multimodal distribution with three dominant peaks (see Silverman test results for multimodality in Supplementary Table 1, Supplementary Fig. 2). The distribution of Rescale 2 without the inconclusive cases—when one of the pairwise combinations and triple combination are lethal—is given in Supplementary Fig. 3. Although the peak at 1 is diminished when the inconclusive cases are excluded, our main result still holds as the identification of synergistic and antagonistic interactions is enhanced. Note that the same result is obtained by Rescale 1 where the triple combination is only compared to the most effective pairwise combination (Fig. 3.2d). This is because the pairwise components in the analyzed data are always stronger than individual drugs. Moreover, in agreement with theoretical predictions, Rescale 3, which defines antagonistic buffering relative to the most powerful pairwise interaction, yields similar results as in both Rescale 1 and Rescale 2. Notably, Rescale 3 leads to cleaner separation between the different modes than the other choices of rescaling (Fig. 3.2e).

Via Rescale 2, we find 38 synergistic, 78 antagonistic buffering, and 47 antagonistic suppressive emergent interactions from 364 different triple-drug combination experiments. Of the remaining combinations, 165 are additive and 36 are inconclusive due to lethality to the pairwise and triple combination. Interaction classifications found via each of the rescaling methods is summarized in the Supplementary Table 2. In Fig. 3.3, we provide a comparison between the existing rescaling method (Rescale 0) and the newly proposed method Rescale 2 in terms of the identification by each of the synergistic or antagonistic triples. We find that the majority of emergent antagonisms (90%) are either classified as additive or underestimated (buffering versus suppression) according to Rescale 0. A comparison of emergent interaction types obtained via the other rescaling methods is given in Supplementary Table 3.

**Figure 3.3: Comparison of Rescale 0 and Rescale 2.** Emergent three-way interactions identified by the old rescaling method ($[\mathrm{E3}]_{\mathrm{R0}}$) are contrasted with the new rescaling method ($[\mathrm{E3}]_{\mathrm{R2}}$) for the synergistic, antagonistic buffering, and antagonistic suppression triples. For each interaction type identified by Rescale 2, the frequency of each interaction type resulting from Rescale 0 is represented in separate charts.

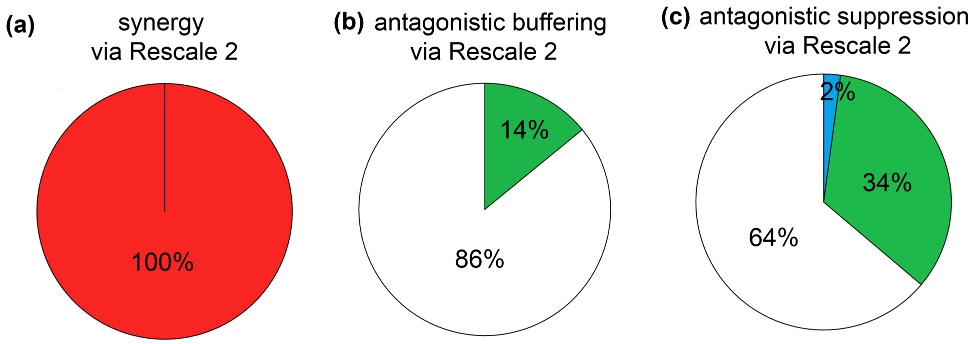

Synergistic interactions from Rescale 2 are identified as 100% synergistic by Rescale 0

Buffering interactions from Rescale 2 are identified as 14% buffering and 86% additive by Rescale 0

Suppressive interactions from Rescale 2 are identified as 2% suppressive, 34% buffering, and 64% additive by Rescale 0

We additionally give two examples of highly synergistic and highly suppressive emergent interactions. First, a triple-drug combination of ciprofloxacin + clindamycin + streptomycin yields emergent lethal synergy (Fig. 3.4a) according to all rescale methods studied here, whereas such an interaction is not apparent with the unscaled version of E3. Next, the drug combination with erythromycin + cefoxitin + tobramycin shows highly suppressive emergent interaction (Fig. 3.4b) according to rescaling methods 1-3, while it is barely identified as antagonistic according to Rescale 0 (previously used method) and is not even identified as antagonistic with the unscaled version.

To see if we obtain similar results (e.g. unimodal distribution from unscaled data, multimodal distribution using scaled methods) with other datasets, we also analyzed the data from Wood et al. [13]. We find that the unscaled measure for this dataset also yields a unimodal distribution (Fig. 3.5 inset), seeming to imply that almost no emergent interactions exist. However, when we apply rescaling methods to this dataset, we observe multi-modal distributions (Fig. 3.5, Supplementary Fig. 4) that are similar to the results from the analysis of our own data. The peak at $-1$ (corresponding to lethal synergies by definition) is not visible for this data. This is due to the fact that the vast majority of the data (93%) are

**Figure 3.4: Examples of highly synergistic and antagonistic emergent interactions among antibiotics.** The bars represent measured growth rates (fitness) under certain drug combinations: no drug (WT), single drugs, pairwise combinations, and triple combination. **(a)** The combination of ciprofloxacin (CPR), clindamycin (CLI), and streptomycin (STR) shows emergent lethal synergy. **(b)** The combination of tobramycin (TOB), cefoxitin (FOX), and erythromycin (ERY) shows a highly suppressive emergent interaction.

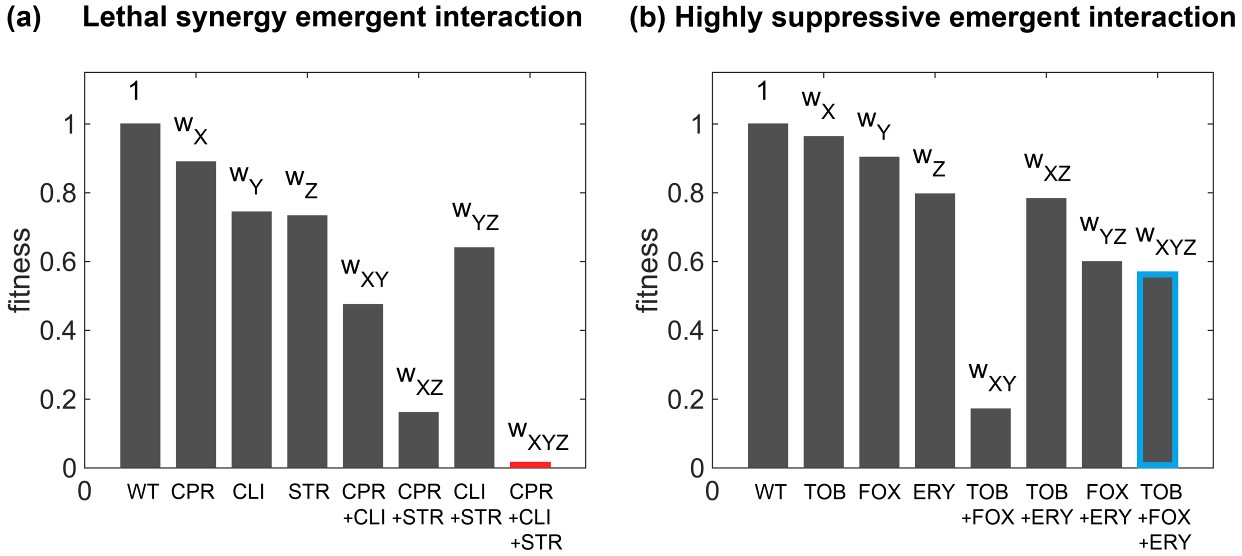
(a) Lethal synergy emergent interaction
(b) Highly suppressive emergent interaction

coming from just 6 combinations of three drugs that are varied in their concentrations to create a larger set of data. These particular combinations and the range of concentrations used result in either emergent antagonism or emergent additivity for almost all experiments. These results are consistent with previous reports that different drug concentrations do not change a drug interaction from antagonistic to synergistic [3]. Therefore, the data in this study mainly represent the effect of varying drug dosages for a small set of drug combinations, whereas our study measures a much larger set of drug combinations and thus analyzes a much larger set of potential interactions and classifications. Even for the limited set of drug combinations studied in Wood et al. [13], we find our rescaling methods greatly enhance the identification of interactions. Specifically, we find only 53% of the measurements are additive with the remaining measurements being synergistic (3%) or antagonistic (44%) emergent interactions, as opposed to $>$ 97% additivity reported by Wood et al. [13]. That is, the choice of rescaling leads to dramatically different conclusions about the presence and overall prevalence of emergent interactions. Moreover, our new analysis reveals that the

Wood et al. [13] data also frequently exhibit emergent interactions and that these interactions tend to be much more antagonistic, but using our new rescale, different datasets yield the same conclusions. Consequently, applying our new rescaling methods to different datasets (ours and Wood et al.'s [13]) yields similar conclusions about an increase in antagonism for higher-order emergent interactions, suggesting the generality of our findings and the need for rescaling.

**Figure 3.5: Analysis of the data from Wood et al. [13].** The histogram of the unscaled emergent three-way measure via Rescale 2 ($[E3]_{R2}$) applied to Wood et al. data. The inset figure shows the histogram of unscaled E3.

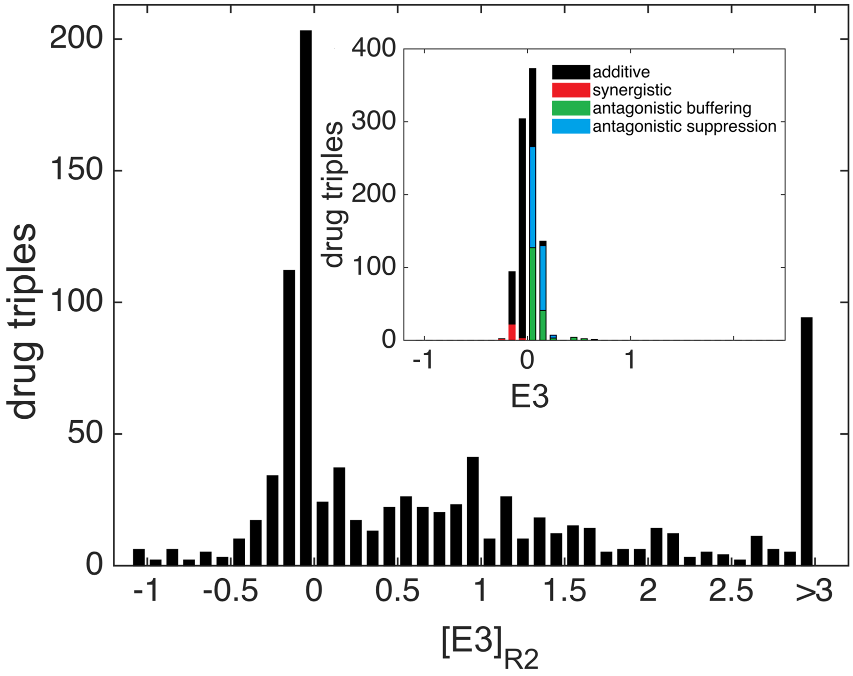

## 3.4 Discussion

Through a systematic analysis of relative growth rates of bacteria exposed to single, pairwise, and triple-drug combinations, we introduced rescaling methods for clearly delineating and categorizing types of interactions among multiple drugs. Due to its unimodal shape, we concluded that the unscaled emergent measure is not useful for identifying and distinguishing among drug interactions. We overcame this problem by constructing new rescaling methods relative to natural reference frames of synergistic and antagonistic cases. As a result, our rescaling methods of the emergent measure allow us to clearly distinguish interaction types via multi-modal characteristics of the E3 distribution.

We have shown that defining antagonistic buffering as the masking effect by the pairwise combinations (Rescale 1) or by all possible lower-order combinations (Rescale 2) lead to nearly identical results. Intriguingly, Rescale 3, where buffering occurs when the overall interaction effect is masked by the strongest pairwise interaction, is somewhat similar to Rescale 1 and 2 but yields important differences for categorizing interactions. The consistency of all three new Rescaling results gives confidence that the identification of the emergent properties is well established. Among these methods, we identify Rescale 2 and Rescale 3 as the best at categorizing emergent interactions based on the distributions they produce. Rescale 2 may be more widely adopted because of ease of interpreting from the fitness measurements, hence comparing through standard bar graphs. On the other hand, Rescale 3 may be desirable because it is more naturally connected to the underlying formulation of E3 itself.

There are three baselines for rescaling: $-1$ (lethal synergy), 0 (additivity), and 1 (antagonistic buffering). Performing a test of multimodality for the distribution of E3 with Rescale 2, we find at least four modes, with three dominant ones occurring at $-1$, 0, 1 (Supplementary Table 1). These modes suggest that our empirical data do segregate into the three extreme cases upon which our rescaling metrics are designed. Intriguingly, there may be a fourth peak that could be a weaker form of antagonism (see multimodal Silverman test in Supplementary Fig. 2). This mode is consistent with features of the pairwise distribution of interactions although that limited dataset makes it difficult to see the peak [3]. As we obtain more empirical data, this fourth peak and other characteristic features of this distribution will be explored in more detail.

Applying the rescaling methods we proposed here substantially changes the existing results for the multidrug interactions from Wood et al. [13]. They suggest that most of the interactions in the multidrug environment can be explained by pairwise and single-drug effects. However, via the use of our rescaling methods, we identify substantial numbers of non-additive interactions from the same dataset. Hence, we conclude that for many combinations the higher-order effects are not simply the result of lower-order effects. These conclusions further strengthen the importance of the choice of an appropriate rescaling method when identifying higher-order emergent interactions.

Our rescaling method enhances the mode for emergent synergy (at $-1$) even more than the Segre et al. [16] rescaling method enhances the mode for synergy for pairwise interactions in a yeast epistasis study. This can be explained by considering the differences of the fitness ranges for yeast knockouts and drug combinations. The fitness of the single knockout is typically very close to the wild type fitness ($= 1$) [16]. Since interaction type is determined based on the comparison between single and double mutants, lethal synergies (when fitness of double knockout is close to 0) are obvious even with the unscaled measure. However, drugs at most useful concentrations lead to lower fitnesses than those that result from single-gene knockouts. Because of this reduced difference between lethality and the single effects, lethal drug synergies are not as obvious with the unscaled measure as they were in the gene epistasis studies. Intriguingly, the rescaling of the emergent interaction measure helps uncover the strength of the synergistic interaction. Moreover, in addition to the modes expected for synergistic, additive, and antagonistic buffering interactions, the rescaling for emergent drug measures yields a substantial number of suppressive triples, thus yielding even more useful information for classifying drug interactions. Taken together, our new rescaling method offers a strong and robust identification and categorization scheme for three-drug interactions and very possibly higher-order interactions in general.

The identification of highly synergistic and suppressive emergent interactions that we established in this study could be especially important for antibiotic research. This importance and clinical relevance is because highly synergistic triple-drug combinations are of utmost importance due to the high efficacy of the treatment compared with pairwise interactions [67, 112, 165–168]. On the other hand, identifying suppressive interactions may be especially valuable because it has been shown that, counterintuitively, these interactions may slow and thus suppress the evolution of antibiotic resistance [3, 8, 36–38, 113]. That is, there may be a trade-off between killing efficiency and the evolution of resistance. Synergistic combinations may be especially good at killing bacteria but may also increase the likelihood and rate of evolution of resistance [37, 38, 113, 169]. Thus, this trade-off can also be seen as balancing the good of an individual with the good of the public.

We note that it can be very important clinically whether three-drug interactions are different from the expectations based on all two-drug interactions. This is because an emergent synergistic interaction would be a potentially novel therapeutic option, whereas a three-way synergy that just resulted from a pairwise synergy would not gain much benefit by adding the third drug. Indeed, in such a case, the third drug could be irrelevant in terms of killing bacteria, and thus likely should not be used in order to decrease the toxic side effects to the patient. This rescaling method will allow us to determine if an additional third drug gives a real benefit. Second, as mentioned above, drug interactions can change the topography of fitness landscapes, and this is important because ultimately, it would be very useful to design landscapes such that the bacteria would have a difficult time reaching maximal fitness peaks with multi-drug resistance. Emergent interactions, as opposed to DA interactions, could change the shape of the fitness landscape more dramatically.

One caveat is that the empirical data are for fixed drug concentrations, so that Bliss Independence is used to determine interaction type. Bliss Independence is a much simpler and straightforward way of measuring interactions than Loewe Additivity, which requires examination of interactions across a gradient of concentrations for each of the drugs. Although Loewe integrates more information about interactions, the ease of measurement and calculation of Bliss Independence has led to its use in a huge number of studies [3, 26, 39, 42, 49, 51, 56, 62, 69], including our present one.

Methods developed here for capturing the higher-order interactions are applicable to other complex systems. These systems include, for example, protein and gene interaction networks (e.g. [31]), food webs (e.g. [30, 144, 146]), and transportation networks (e.g. [170]). Hence, our rescaled emergent measure offers a systematic and straightforward method for uncovering the complex interactions that occur in a wide range of systems.

In summary, we have shown that our new rescaling methods lead to a clear distinction between different categories—synergistic, additive, antagonistic buffering, and antagonistic suppressive—of interactions, and that these distinctions do not exist when looking at results for the unscaled measure or the previously used rescaling method (i.e. Rescale 0). Therefore, our new rescaling methods are required to accurately characterize cases of emergent interactions among multiple drugs. In particular, Rescale 2 and Rescale 3—synergy defined relative to lethality for both cases and antagonistic buffering relative to the strongest lower-order effect (Rescale 2) or interaction (Rescale 3)—offer a direct and more distinct measurement of epistasis that is straightforward to generalize to higher-order interactions. Therefore, we propose that Rescale 2 and 3 could be a useful tool in future studies that examine complex drug interactions or other complex systems with interacting components.

## 3.5 Acknowledgements

We thank Eliot Landaw and Tom Chou for discussion, and Tina Manzhu Kang, Emily Vargas, Borna Shirvani, and Gabriel Ting for assistance in the lab.

# CHAPTER 4

# Do Vascular Networks Branch Optimally or Randomly across Spatial Scales?

## 4.1 Introduction

The cardiovascular system is responsible for the vital processes of delivering oxygen and nutrients to cells, as well as clearing waste products, via blood flow from heart to capillaries. Accomplishing these processes requires highly complex structures because nearly all the cells throughout the body are fed by capillaries—the terminal tips of the cardiovascular system.

These linkages explain why the cardiovascular system plays a critical role in most modern allometric scaling theories that relate metabolic rate and body mass via a power law with the scaling exponent 3/4 [9, 11, 77–79, 171, 172]. Recent analyses of allometric scaling relationships using extensive data (more than 600 mammalian species and 64 plant species) yield second-order curvature in log-log space that represent deviations from this pure power law [10, 91–94]. Attempts to account for this observed curvature, via including higher-order approximations and more accurate fluid dynamic relations, lead to curvature in the opposite direction (convex versus concave) of the empirical data [11]. This and other recent results [173] suggest the need to revisit the assumptions behind the existing models. In this paper, we show the ways in which current assumptions are insufficient to capture the patterns in empirical vascular data, and we propose new assumptions for vascular branching that could help eventually provide the foundation for a revised allometric scaling theory.

Current theories for allometric scaling, such as those proposed by West, Brown, and Enquist (WBE) [79], Banavar et al. [80, 81] , Dodds [82], and Huo and Kassab [83] rely on mathematical models that encompass the architectural design of the cardiovascular system to different degrees of detail and accuracy. Within these models, the cardiovascular system is typically idealized as a hierarchical branching network that is constrained by a few core physical and biological principles. These principles lead to derivations for fractal-like, self-similar properties—having a pattern that repeats itself across large and small scales—for the overall structure of the network [86, 99, 174]. Previous models also often assume that branching is symmetric such that sibling vessels—daughter vessels branching from the same parent—are identical in terms of their radius, length, flow rate, and pressure.

Although many models presume perfect symmetry between siblings [10, 79, 83, 175], inspections of vessel casts and images reveal that some regions have highly asymmetric branching [176–179]. Such asymmetric branching patterns were empirically quantified by Zamir who showed there are differing degrees of asymmetry across levels of the coronary arteries [87]. Moreover, a recent paper by Hunt et al. [98] shows that there is a high degree of asymmetry in vessel lengths within the mouse lung (micro-CT images) and human head and torso (MRI), demonstrating that symmetric branching is not an accurate representation of the cardiovascular system. Nevertheless, if the degree of asymmetry is repeated across branching junctions, this would still represent a modified version of self-similarity.

Given the evidence for asymmetric branching, we propose to investigate patterns of asymmetry in vascular branching. Because vessel radii exhibit relatively little asymmetry and are consistent with existing models [5], we focus on asymmetries in vessel lengths and branching angles. Through the identification and investigation of these new, systematic patterns, an explanation might eventually be obtained for the mismatch between theoretical predictions from scaling theory and empirical data [10]. Conversely, the consistency of the empirical scaling relationships across different species and taxa [9–11, 92, 93] suggests that shared developmental processes and evolutionary pressures powerfully constrain the degree of asymmetric branching within the vascular system, possibly corresponding to core, yet unidentified, biological and physical principles.

Developmental processes are known to play a key role in vascular branching, and these processes likely introduce stochasticity and randomness into patterns of asymmetry in lengths of sibling vessels. For example, at local to intermediate spatial scales, vessel branching is often initiated by the metabolic demands of growing tissue as signaled by expression and concentration levels of Vascular Endothelial Growth Factor (VEGF) [104]. In addition, at even more local scales, branching location is primarily affected by the shear-stress gradient between the fluid and vessel wall, related to the curvature of the branching vessel [180,181].

In terms of evolutionary pressures, it has been proposed that the architecture of the cardiovascular system is governed by optimization principles such as minimization of the construction materials (i.e., material cost (MC)) or of power loss (i.e., power cost (PC)) across the network to provide efficient flow [89,105,106,176]. These principles lead to largely deterministic outcomes that could constrain the branching structure locally (individual branching junction), globally (whole network), or through some intermediate spatial scale. Indeed, at the global scale, vascular branching likely requires more deterministic or programmed processes due to the necessity of distributing blood to the extremities such as hands, feet, and the brain.

The local optimization of MC and PC at each branching junction—where a parent vessel branches into daughter vessels—has been studied by Murray and Zamir for the case that the radii of vessels are fixed [105,106,182,183]. These optimization problems were used to derive predictions for branching angles of sibling vessels relative to the parent vessel (Fig. 4.1c, d). Although not explicitly considered in previous studies, length asymmetry is directly tied to branching angles because both are completely determined by the position of the branching junction relative to the other endpoints of the vessels. Furthermore, these previous studies used a fluid-dynamically incorrect linear summation of each vessel's individual power loss to calculate total power loss for the branching junction [106]. This approach works for construction material but does not for power loss because it ignores different rules for how to combine resistances (impedances) of vessels in parallel versus in series. Moreover, even for minimization of material cost, these studies [105,106] did not examine the full solution space for the optimal position of the branching junction, resulting in misleading solutions for some cases. In this paper, we address these problems and clarify the confusion in the literature on optimal branching geometries. In so doing, we provide a connection between optimal branching angles, optimal ratios and asymmetries for sibling vessel lengths, and observed asymmetry in branching patterns.

**Figure 4.1: Cardiovascular data and schematic illustration of vascular branching** **(a)** Mouse lung micro-CT images processed by Angicart. **(b)** Human head and torso MRI images processed by Angicart.**(c)** Schematic illustration of the asymmetric branching geometry and labeling. Parent vessel with radius $r_0$ and length $l_0$ branches into two daughter vessels with radius $r_i$ and length $l_i$ with subscript $i = 1$ or 2. Branching angles, $\theta_i$, are defined by the angle between the sides defined by the endpoints of the vessel pairs. Here, subscripts are determined by the non-adjacent vessel. (see 4.5 Materials and Methods) **(d)** Optimization of local branching on a plane finds the optimal location of the branching junction $j$ when the unshared endpoints ($V_i$) and the radii ($r_i$) are fixed (see 4.2.1 General framework for branching angle optimization and asymmetry).

**(a)** Mouse lung

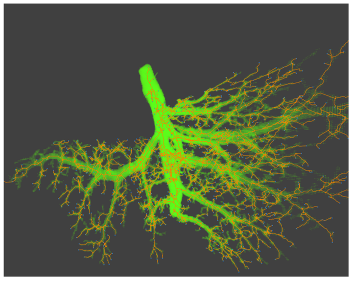

**(b)** Human head & torso

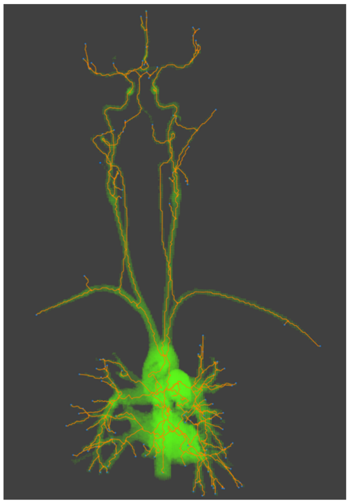

**(c)** Asymmetric branching

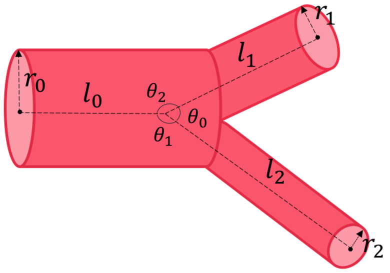

**(d)** Optimization of local branching

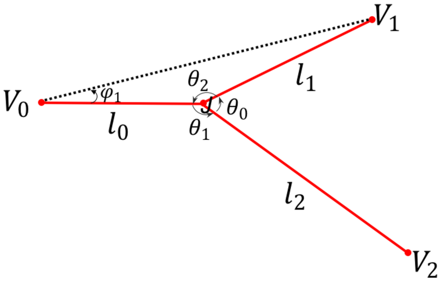

Although there are substantial theoretical predictions for the vascular system, those predictions have rarely been tested on an extensive set of data. Most vascular data have been collected via casting or dyeing methods [95, 95–97] that do not produce sufficiently detailed data or large enough amounts of data due to the challenges of manually measuring branching angles. Recently, a novel software package, Angicart, was developed to extract three-dimensional vascular networks from the aligned stacks of high quality angiographic images [5]. In this paper, we employ Angicart to analyze characteristics of the cardiovascular structure from micro-CT images of healthy mouse lung (Fig. 4.1a) (micro-CT imaging is described in [184]) as well as the MRI of human head and torso in 18 different subjects (Fig. 4.1b) [5, 98]. Consequently, we have collected detailed data for vascular networks that include asymmetry ratios at each junction (see 4.3.1 Analysis of asymmetry patterns in vascular data) and measures of vessel radii, lengths, and branching angles (see 4.5 Materials and Methods).

Here, we present patterns that hold across the entire network for the degree of asymmetry in vessel radius, length, and branching angle between sibling vessels. Then, we investigate the validity of the previously proposed branching angle optimizations at the local level. As part of this, we propose an alternate method for solving these minimization problems, including the full solution of the MC optimization that considers both total surface area and total volume. Next, we introduce an optimization scheme for minimizing power loss (i.e., PC optimization) that correctly implements the flow dynamics for a bifurcating structure and can also incorporate downstream impedances and power loss. We note that several of these optimization schemes result in network-level patterns of asymmetry similar to those observed in the real data. Next, as a stronger test of which optimization principles, if any, lead to the asymmetric branching patterns in real systems, we compute theoretical predictions for each branching junction in a comprehensive set of vascular data from mouse and human subjects and compare whether our predictions match the real data at the junction-level. Finally, we explore how random branching is constrained at different spatial scales, ranging from local to intermediate to global, affects the network-level characteristics of the empirical data via simulations of the branching structure. Overall, we compare our carefully constructed mathematical frameworks for optimal and random processes of vascular branching to new analyses of recent empirical data that enables us to improve our understanding of how structural properties of the vascular system are constrained by core biological and physical principles.

## 4.2 Optimal models and random simulations for vascular branching

### 4.2.1 General framework for branching angle optimization and asymmetry

Systematic patterns in branching angles or asymmetric ratios [98, 100–102] (see 4.3 Results, 4.3.1 Analysis of asymmetry patterns in vascular data) suggest that a constraint that likely arises through natural selection, the nature of the growth process, or both. Most hypotheses about the force of natural selection on vasculature have focused on principles that reduce the cost of materials and growth while also providing efficient flow mechanisms [87,89,105,106,176]. These biological principles could apply at each branching junction (locally) during growth or across the whole network (globally) through some larger bauplan. In this study, we initially focus on the local optimization aspects of these principles. Then, we consider applying different spatial (regional) constraints on the branching structure, including simulating networks that have random branching within constraints that range from intermediate to global spatial levels of the network.

For the local optimization of bifurcating branching geometry, following a similar approach as in the previous studies by Zamir and Murray [105,106], we assume that the radius ($r_i$) and the unshared endpoints of the vessels, i.e., the vertices ($V_i$), are fixed, whereas the branching junction at the shared endpoint ($j$) varies (Fig. 4.1c, d). In this framework, we derive the optimal placement of the branching junction ($j$) by constructing and minimizing a cost function based on each biological principle that is hypothesized to increase the fitness. In all our derivations, we follow Krogh's model that regards blood vessels as cylinders [90]. In addition, both human and mouse data provide evidence that all of the vessels involved in a branching junction lie within a single plane (S1 Fig.). Thus, for our derivations of optimal branching geometry, we assume that the branching junction lies in the plane determined by the unshared endpoints of all vessels.

To try to elucidate the cause of the high degree of length asymmetry observed in data (see 4.3 Results), we also take a new approach and derive the length asymmetry from the solutions of these optimization principles. That is, by finding optimal branching angle solutions, we determine the location of the branching junction that in turn uniquely determines vessel lengths and leads to predictions for optimal length asymmetry. The formula that associates the length asymmetry with the optimal branching angles is introduced in the Appendix B.

As mentioned above, we consider two general principles. First, because construction and maintenance can be expensive to the body, minimizing total material is a potential driving factor for the structure of the vascular system. Such a principle will be referred to as *material-cost optimization* (MC optimization). The total material cost across the bifurcation is the linear sum of the material cost for each vessel because material cost is an additive quantity over different vessels.

Next, a viable design for the vascular system requires efficient flow mechanisms—such as minimal power loss—to transport nutrients and oxygen to cells. This scheme will be called *power-cost optimization* (PC optimization). In order to establish a cost function that represents the total power loss across a bifurcation, we need to use appropriate fluid-dynamical concepts. Because the effective impedance is not a linearly additive quantity for combining vessels at a branching junction, PC optimization requires a more complicated cost function than MC optimization. In this respect, our derivation differs from and corrects previous branching angle optimizations by Zamir [106]. As another new element to our approach, we further propose an optimization scheme that can incorporate the power cost due to the downstream impedances beyond just a single branching junction.

In the following sections, we first introduce the branching angle optimization solutions for the MC and PC optimizations for a local branching junction. Next, we explain a new scheme for the PC optimization that incorporates information about the flow properties of the downstream vessels. Lastly, we relax the optimization principles and present simulations of random branching to explore how constraints—local to intermediate to global—can alone affect the characteristics of the vascular network.

### 4.2.2 Material-cost (MC) optimizations

There are two types of material that are needed for the vascular system, blood vessels (endothelial cells) and blood (plasma and white and red blood cells). The amount of material necessary for vessel construction primarily depends on the surface-area of the vessel $2\pi rl$. In contrast, the material devoted to the blood is proportional to the blood volume ($\pi r^2 l$). MC optimizations can be built upon these two different characteristics (surface-area (MC-SA) or volume (MC-V)). We consider both cases here.

To consider total surface-area and volume as distinct structural constraints that need to be minimized to conserve construction material, as in Murray and Zamir [105, 106], we form a generic cost function $H$ in which lengths are weighted according to the corresponding optimization. Explicitly, $H = \sum_i h_i l_i$ where $h_i = 2\pi r_i$ for surface-area and $h_i = \pi {r_i}^2$ for volume. In general, the constant geometric factors like $2\pi$ can be ignored because they cancel from every term when the derivative of $H$ is set equal to zero. As introduced above, we assume that the radius and the unshared endpoints for each vessel are fixed when performing the optimization calculation. For fixed radii (or equivalently for fixed cost terms $h_i$) and the vertices, the MC optimization problem is equivalent to the weighted Fermat Problem introduced by Greenberg and Robertello [185–187].

To solve these minimization problems, we present a different method than that used to obtain Zamir and Murray's solutions. Our method relies on distance metrics without invoking a coordinate system (Appendix C) and is therefore simpler and more general. The method is straightforward when one realizes that the location of the branching junction is uniquely defined by the parent vessel length ($l_0$) and the angle ($\varphi_1$) between the parent vessel and the edge determined by the unshared endpoints of itself ($V_0$) and one of its daughter vessels ($V_1$) (see Fig. 4.1d). Based on this, we obtain the full solution of optimal branching angles by finding the stationary and singular points of $H$ with respect to $l_0$ and $\varphi_1$ throughout the entire space.

In this framework, we recognize that the first order derivatives of $H$ are discontinuous and thus undefined at the unshared endpoints ($V_0, V_1, V_2$). Hence, singularities (values of infinity) are attained at these endpoints. Moreover, we find that the stationary solution for minimizing $H$ exists only in the interior of the triangle defined by the unshared endpoints. In the latter case, the optimal branching angle solution is

$$\cos\theta_0 = \frac{{h_0}^2 - {h_1}^2 - {h_2}^2}{2h_1h_2}, \cos\theta_1 = \frac{{h_1}^2 - {h_0}^2 - {h_2}^2}{2h_0h_2}, \cos\theta_2 = \frac{{h_2}^2 - {h_0}^2 - {h_1}^2}{2h_0h_1} \tag{4.2.1}$$

Note that our branching angles are defined differently than in Zamir [106], so these equations are equivalent but not identical. Recognizing our definitions are relative to the parent rather than centerline extended from the parent, these expressions can be translated into Zamir's solutions by subtracting our angles $\theta_1$ and $\theta_2$ from $\pi$. Moreover, in our 2D (planar) optimization scheme, we use the conventional counter-clockwise direction to define the angles so that the trigonometric functions have consistent signs (Fig. 4.1d). Correctly defining the directionality of the angles is needed for our mathematical derivation, but for comparing to empirical data, we compute only the magnitude of the branching angles. Although it is more challenging to define directionality of angles for the real, empirical data in three dimensions, it is still straightforward to measure the magnitude of the angle between the straight lines defined by the endpoints of vessels (see 4.5 Materials and Methods), allowing us to directly compare with the solutions from the 2D optimization.

Notice that the branching angle solution for the stationary case does not exist when the right side of the above expressions are not in the interval $[-1, 1]$. For instance, when $h_0 = 2.1$ and $h_1 = h_2 = 1$, then $\cos\theta_0$ =1.21 and $\theta_0$ is not defined. Values outside of the allowed interval occur frequently when substituting values from real vasculature, so these equations should not be blindly applied without considering the allowed regions and intervals. Moreover, there are cases for which an optimal branching solution can be computed from the above equations, but the resulting branching junction does not lie inside the triangle defined by the fixed vessel endpoints. In this case, the computed optimum does not correspond to the true optimum, which actually occurs at one of the fixed vessel endpoints (i.e., the vertices of the triangle). Indeed, for both of these cases where the stationary solution either cannot be computed or the computed answer lies outside the pre-defined triangle, the optimal solution is actually attained at one of the singularity points, i.e., the vertices $V_i$.

Based on these observations, we find the conditions on the cost parameters and the geometry of the fixed endpoints that correspond to degenerate branching solutions. For example, when the cost of one vessel exceeds the total cost by the other vessels ($h_i \geq h_j + h_k$), then the optimal branching occurs at the unshared endpoint of the vessel $i$ ($V_i$) to eradicate this particularly costly vessel. On the other hand, when the solution $\theta_i$ defined by (4.2.1) is less than the angle $V_jV_iV_k$ (i.e., $\cos\theta_i > \cos V_jV_iV_k$), which we refer to as the triangle condition, then the branching junction collapses onto the vertex $V_i$. The details of the proof are given in the Appendix D.

These degeneracies are not specified in previous work [105, 106] because vessels are assumed to have volume flow rates that are proportional to $r^3$. With this presumption and by the conservation of volume flow rate across each branching junction, those studies assume a strict relationship between radii of the parent and daughter vessels (Generalized Murray's law: ${r_0}^d = {r_1}^d + {r_2}^d$ , where $d \in [2, 3]$ [89]) that avoids the degeneracy (S2 Text). Moreover, previous work does not explicitly consider cases in which the branching angle solution cannot satisfy the triangle conditions defined above. Importantly, we find that these ignored cases and conditions correspond to the vast majority of values calculated from empirical branching vessels (S2 Fig).

### 4.2.3 Power-cost (PC) optimization for a single branching junction (PC-0)

Another biological principle and property to optimize is the power loss for pumping blood from the heart to the capillaries. This principle is tantamount to minimizing the total power for circulating blood or the total power lost that represents additional power beyond what is used to move the blood. In this way, as much of the additional power as possible is then redistributed and devoted to other needs such as foraging and reproduction [78, 79]. Much of the power that is required to push blood through the parent and daughter vessels is lost due to dissipation, especially in the smaller vessels that dominate the numbers and energetics of the whole vascular network. We calculate the power dissipated by a single vessel in terms of the volume flow rate of the blood ($\dot{Q}$) and the impedance ($Z$) via the formula $P_{loss} = \dot{Q}^2 Z$ [87, 176, 188]. To correctly compute the total power loss of all vessels connected by a single branching junction—a parent and daughter vessels, we must employ rules of fluid dynamics to combine impedances into an equivalent impedance. This equivalent impedance must in turn be used in the cost function for the power minimization (see below), and as we show, the correct version is different than the simple linear addition rule used by Zamir for both structural (correctly) and flow (incorrectly) constraints [106].

For any collection of vessels, total volume flow rate $\dot{Q}_{TOT}$ is defined by flow through a single cross section that cuts through all vessels at the same branching level. Equivalent impedance $Z_{eq}$ for the collection of vessels is defined by $Z = \Delta p / \dot{Q}$, based on fluid dynamics (analogue to Ohm's Law), where $\Delta p$ is the pressure difference across the extreme endpoints through which blood flows in and out of the entire collections of vessels. The total power loss for the collected vessels is then calculated from $P_{loss} = \dot{Q}_{TOT}^2 Z_{eq}$, where all of this is based on standard rules of fluid dynamics.

For a single branching junction, the optimization of power loss is derived for the case that there is a source with a constant rate of flow, $\dot{Q}$, entering the parent vessel. Based on our power loss equation ( $P_{loss} = \dot{Q}_{TOT}^2 Z_{eq} \propto Z_{eq}$), the PC optimization is then equivalent to minimizing the equivalent impedance $Z_{eq}$ of the branching junction. By following the direction of the flow, we calculate the equivalent impedance by noting that vessels at the same level (i.e., sibling vessels) are in a parallel configuration, whereas the vessels across levels (i.e., parent and daughter vessels) are in a series configuration. Pressure drop across sibling vessels may be asymmetric but to simplify the calculation of an equivalent impedance, we further posit that the pressure drop across each daughter vessel is approximately the same, i.e., $\Delta p_1 = \Delta p_2 \coloneqq \Delta p_d$. Representing total volume flow rate of the daughter vessels by $\dot{Q}_{d,\ TOT} \coloneqq \dot{Q}_1 + \dot{Q}_2$ and equivalent impedance of the daughter vessels by $Z_{d,\ eq}$, we have $\Delta p_d / Z_{d,\ eq} = \Delta p_1 / Z_1 + \Delta p_2 / Z_2$. Canceling the pressure terms gives $Z_{d,\ eq} = \left(\frac{1}{Z_1} + \frac{1}{Z_2}\right)^{-1}$. By invoking conservation of fluid, we can combine this expression with the parent vessel in series to obtain $Z_{eq} = Z_0 + \left(\frac{1}{Z_1} + \frac{1}{Z_2}\right)^{-1}$ for the equivalent impedance of all the vessels that connect at a single branching junction.

Assuming smooth, Poiseuille flow, the impedance of a single vessel is given by $Z = \frac{8\mu l}{\pi r^4}$, where $\mu$ is the viscosity of the blood [87,177,189]. Thus, for each vessel we implement a cost function of the form $hl$, where $h$ is the cost per length, i.e., $h \equiv \frac{8\mu}{\pi r^4} \propto \frac{1}{r^4}$. Putting all of this together to find a solution for the PC-0 optimization (power loss at a single branching junction), our goal is to find the position of the branching junction that minimizes

$$Z_{eq} = h_0 l_0 + \left(\frac{1}{h_1 l_1} + \frac{1}{h_2 l_2}\right)^{-1}$$

By numerically calculating $Z_{eq}$ as a function of the junction point and by using high resolution in space, we generate heat maps that illustrate the behavior of $Z_{eq}$. These heat maps reveal that the *branching junction always collapses onto one of the vertices*—unshared vessel endpoints—for *any values* of vessel radii (S3 Fig). Based on our numerical evidence, we show analytically that power loss and equivalent impedance, $Z_{eq}$, attain minima only at a vertex of our original triangle that is defined by the unshared endpoints of the vessel. The specific vertex at which the junction collapses is determined both by the vessel radii and the relative locations of the unshared endpoints of the vessels. The proof follows from two steps. First, we calculate the equivalent impedance at each vertex to see how specific cases of cost parameters $(h_0, h_1, h_2)$ determine which vertex is the best location for the branching junction $j$. Second, we show that when the junction is located within the triangle, $Z_{eq}$ is always greater than the minimum value of the impedances when the junction is at a specific vertex. Together, this proves that the minimum of $Z_{eq}$ is attained at one of the vertices (Appendix E). Therefore, the PC-0 optimization leads to a degenerate branching geometry by completely eliminating the vessel that is most costly.

Thus, minimizing power loss at a single branching junction leads to either no branching at all throughout the entire cardiovascular network or to a single hub at the heart with a long, individual vessel to each terminal tip—the most downstream vessel of the network. This architecture would result in extremely large numbers of vessels directly connected to the heart because terminal tips correspond to capillaries (numbering in the millions or billions) for complete networks. This is unrealistic as sequential branching is the most noticeable and perhaps most important feature of the vascular system or any resource-distribution network. Therefore, we consider how to modify the PC minimization to attain more biologically realistic results that include vascular branching and thus lead to predictions for the branching angles and vessel lengths. In the next section, we describe how to adapt the power-minimization calculation to include larger sections of the network that expand beyond a single branching junction to encompass downstream vessels and branching junctions.

### 4.2.4 Power-cost (PC) optimization beyond a single branching junction (PC-1)

The solutions above thus lead to either a single path or to the heart being a single hub that separately connects to each capillary through a direct and independent vessel. Either configuration for vascular architecture would prevent the vascular system from efficiently distributing blood to all the downstream vessels, capillaries, and cells. To overcome these problems, we include larger sections of the vascular network by incorporating impedances of downstream vessels. To do this generically, we recognize that downstream vessels are in series with each of the daughter vessels, so we can represent the downstream impedance by adding constant terms $c_1$ and $c_2$ to the impedance of the daughter vessels. Thus, the equivalent impedance of the bifurcation becomes

$$\tilde{Z}_{eq} = Z_0 + \left( \frac{1}{Z_1 + c_1} + \frac{1}{Z_2 + c_2} \right)^{-1}$$

For the case of vessels above the capillaries, these constant terms represent the impedance from all of the downstream vessels. For the capillary case, these constant terms are still not zero, however, because they represent the minimum impedance of a capillary, which is not allowed to be zero. We now investigate different geometries for a single branching junction for which the downstream impedances $c_1$ and $c_2$ are constant.

We simplify this problem using two general principles. First, when the impedance of the parent vessel and the branching daughter vessels are matched, no pulsatile reflections occur and the power loss at the bifurcation is minimized [87, 188]. Second, we assume the simple case that the siblings have identical impedances and each sibling has the same number of downstream vessels. From these two assumptions, we find that the equivalent downstream impedance is much larger than single vessel impedances except for vessels close to the capillaries (Appendix F).

Because the number and small surface-areas of capillaries will again likely dominate the power loss for the network, we solve the optimization problem when the downstream impedances are large, i.e., $c_i \gg Z_i$. Consequently, we expand $\tilde{Z}_{eq}$ as a series to first order and obtain the following approximation:

$$\tilde{Z}_{eq} \sim Z_0 + \frac{{c_2}^2}{(c_1+c_2)^2} Z_1 + \frac{{c_1}^2}{(c_1+c_2)^2} Z_2 + \frac{c_1 c_2}{c_1+c_2}$$

We note that the constant term $\frac{c_1 c_2}{c_1+c_2}$ can be ignored because its derivative is zero and hence does not influence the optimization. As a result, we want to find the location of the branching junction that minimizes

$$h_0 l_0 + \frac{{c_2}^2}{(c_1+c_2)^2} h_1 l_1 + \frac{{c_1}^2}{(c_1+c_2)^2} h_2 l_2$$

The coefficients $\frac{{c_2}^2}{(c_1+c_2)^2}$ and $\frac{{c_1}^2}{(c_1+c_2)^2}$ are always less than 1, so the cost per length for the daughter vessels are diminished by these rescaling constants, thus reducing the likelihood the solution will collapse onto a daughter vessel endpoint. Defining the non-dimensionalized ratio $k := c_1/c_2$, the optimization function becomes

$$H := h_0 l_0 + \frac{1}{(k+1)^2} h_1 l_1 + \frac{k^2}{(k+1)^2} h_2 l_2$$

This further implies that the cost of the daughter vessel with the larger downstream impedance is diminished less than the cost of the other daughter vessel. This pushes the optimal branching junction towards the daughter vessel with smaller downstream impedance.

The new optimization function for power loss above (i.e., PC-1) has the same form as the cost function for the material-cost (MC) optimizations, except that the costs per length for daughter vessels are rescaled by terms that depend on $k$. We therefore simplify the notation and define $\tilde{h}_0 = h_0$, $\tilde{h}_1 = \frac{1}{(k+1)^2} h_1$, $\tilde{h}_2 = \frac{k^2}{(k+1)^2} h_2$. With these definitions for $\tilde{h}_i$, we can immediately use our results for Eq. (4.2.1) to obtain the stationary solution for which the branching junction occurs inside the triangle of the unshared endpoints.

As for Eq. (4.2.1) and the MC optimizations, the stationary solution does not exist or does not provide the minimum and the degenerate solution occurs at vertex $V_i$ for the following cases: 1) $\tilde{h}_i \geq \tilde{h}_j + \tilde{h}_k$ or 2) $\cos\theta_i = \frac{\tilde{h}_i^2 - \tilde{h}_j^2 - \tilde{h}_k^2}{2\tilde{h}_j\tilde{h}_k} > \cos V_jV_iV_k$. These two conditions correspond to six inequalities in terms of $k\,(= c_1/c_2)$ if we take all combination of $i$, $j$, and $k$. Solving these, we obtain the values of $k$ that result in solutions within the triangle versus those that collapse on a vertex. Mapping these values into the $c_1c_2$-plane yields predictable lines that separate the plane into regions classified as non-degenerate (collapse onto a vertex) or degenerate (junction within the triangle) solutions. Indeed, by using approximations to solve the above limiting case ($\frac{Z_i}{c_i} \ll 1$), we predict the full solution space. The validity of our approximate solutions for this PC-1 optimization problem is further explored in Results (Analytical solutions for power-cost optimization beyond single branching (PC-1)) by comparing them with numerical solutions.

### 4.2.5 Expanding from local to global constraints for the random placement of branching junctions

The above optimization schemes are based on the local consideration of branching junctions: at each branching the unshared endpoints ($V_i$) are fixed and the branching junction ($j$) is attained within the triangle of these endpoints (Fig. 4.1d). To explore the effects of the size of the constraint region and also to observe the effects of random branching, possibly resulting from developmental processes, at different spatial (regional) constraints, we now consider relaxing the locality assumption to various degrees from fully local to fully global.

We simulate the branching network by randomly placing branching junctions within spatial regions that range from local boundaries (i.e., the positions of adjacent branching junctions) to global boundaries (i.e., within some maximum distance of the center of the network but otherwise unrestricted). For all the simulations, the hierarchical ordering of vessels, the location of the terminal tips, and most upstream branching nodes (i.e., the source) are the same as in the empirical data. We created 100 realizations for each simulation type to get the average behavior of network characteristics. All these different simulation types are illustrated with a simplified example network that has 3 branching levels (Fig. 4.2).

**Figure 4.2: Comparison of real data for vascular networks versus random simulations of branching junctions.** The real and simulated networks (via local to global spatial constraints) are separated by different rows. A schematic small network is given to describe how different simulations are performed. The vessels and the fixed endpoints of the real branching network are represented in red. Vessels that result from random branching simulations are in black. The healthy mouse lung network and the simulated mouse lung networks are shown within a minimum spherical boundary that contains all branching data from the real network. Here, the red nodes for each figure correspond to the real data, whereas the black nodes correspond to the simulated data. Note that the terminal tips and the most upstream node (i.e., the source) are determined from real data and fixed throughout all simulations. The resulting asymmetry ratio distributions for length and branching angles are provided for the real network and for each of the simulations. The statistical comparisons of random branching simulations with empirical data are given in Table 4.1.

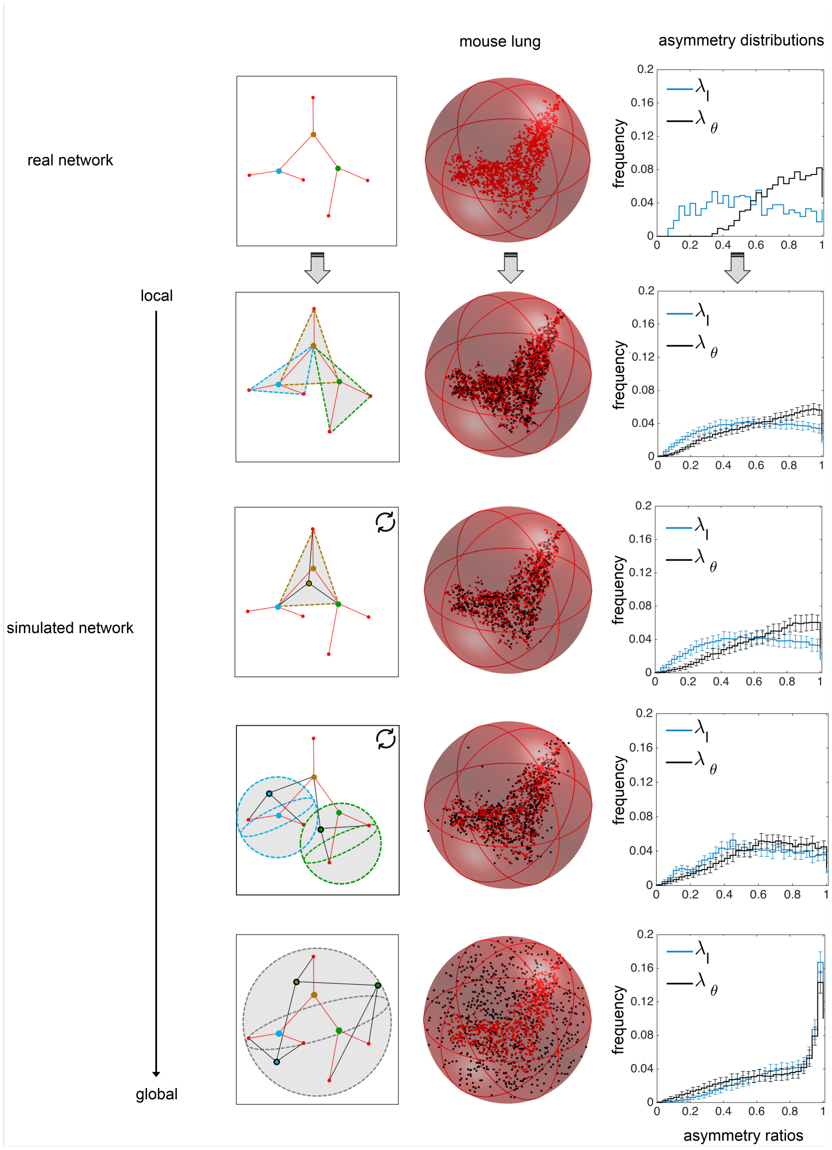

For the fully local case, we randomly place a branching junction inside each triangle of unshared endpoints of three connected vessels, corresponding to the same spatial restriction as in our optimizations above (Fig. 4.2). This random branching model would likely correspond to branchings determined by locations of highest shear stress [181] or local maxima in gradients of vascular endothelial growth factor (VEGF) [104] that signal branching at local and intermediate scales. For the fully global case, we only require that the branching junctions are randomly positioned within a minimum sphere that contains all nodes from the real data [190] (Fig. 4.2) and that the network terminates at the appropriate (most extreme upstream and downstream) endpoints in the network.

For intermediate degrees of spatial constraint between the fully local and fully global cases, we consider two possibilities. These intermediate states are constructed such that they involve sequential updates of the branching junction. The first intermediate randomly branching network simulation (intermediate 1) starts by randomly positioning a branching junction within the local triangle corresponding to the most upstream vessel (i.e., source) of the network and the endpoints of its two daughter vessels. Based on the new location of this branching junction, the endpoints of the daughter vessels are then updated and used to define new triangles in the next step in which the daughters become the parents. The simulation continues this updating process by working down through the network until it reaches the terminal tips (Fig. 4.2, S4 Fig). Notably, this simulation leads to branching junctions that are approximately confined to the plane. The other intermediate randomly branching network (intermediate 2) starts with the terminal tips (most downstream vessels of the network) and builds backwards to the first branching node (i.e., the source). We assign the position of each branching junction by creating a spherical boundary around the two fixed downstream endpoints (i.e., $V_1$, $V_2$, Fig. 4.1d) such that the center of the sphere is at the midpoint of $V_1V_2$ and the sphere has a radius of the length $|V_1V_2|$. We then randomly position the branching junction at a point that can occur anywhere within the volume of this three-dimensional sphere. Thus, for this simulation a branching junction may not always fall within the plane defined by the vessel endpoints, as it does for the first simulation for intermediately-constrained random branching. For this case, the upstream endpoint (i.e.,

$V_0$) does not affect the location of the branching junction, reducing the degree of locality compared with the constraint for the simulation for intermediate 1.

## 4.3 Results

We begin this section with empirical data for asymmetry in the vascular branching of mouse lung and human head and torso. Following this, we present the results of our local optimization schemes. Next, we present results for our exploration of different spatial constraints for randomly placed branching junctions and compare these results with empirical data. Finally, we provide statistical analysis of different optimization schemes and random-branching results as compared with the empirical data. This comparison enables us to quantitatively investigate how well our predictions match the empirical measurements of asymmetry in vasculature, and thus to characterize whether different optimizations or random processes might underlie the systematic patterns we observe.

### 4.3.1 Analysis of asymmetry patterns in vascular data

To characterize the branching asymmetry of the vascular structure, we calculate asymmetry ratios between siblings. In particular, the asymmetry ratios for radius and length are $\lambda_r = r_1/r_2$ and $\lambda_l = l_1/l_2$, respectively, where the value of the sibling with the larger radius or length is always chosen to be in the denominator ($r_1 \leq r_2,\ l_1 \leq l_2$) [87,191]. Thus, a ratio of 1 indicates perfect symmetry, whereas smaller values indicate more asymmetrical branching. We further provide a similar measure to quantify local asymmetry in sibling branching angles as $\lambda_\theta = \theta_1/\theta_2$ again with $\theta_1 \leq \theta_2$ (Fig. 4.1c).

It is easy to see that asymmetry in vessel lengths is related to asymmetry in branching angles. When the downstream ends of the daughter vessels are equidistant from both the upstream and downstream ends of the parent vessel, siblings have identical length and branching angles, resulting in symmetry $\lambda_l = \lambda_\theta = 1$. However, if daughter vessels are not equidistant from the upstream end, even symmetric sibling lengths can result in asymmetric branching angles or vice versa. Therefore, the value of $\lambda_\theta$ represents a combination of the asymmetry in lengths and the asymmetry of the alignment of daughter vessel endpoints.

After executing Angicart on high-quality tomographic images, we quantified the extent to which the analyzed networks are asymmetric by plotting the frequency distributions of $\lambda_r$, $\lambda_l$, and $\lambda_\theta$ (Fig. 4.3a, b). Even though asymmetric radius branching exists, data for both mouse and human show distributions of $\lambda_r$ that are skewed towards 1, meaning that the radius ratio is skewed towards perfect symmetry. In contrast, the length asymmetry ratio ($\lambda_l$) is distributed almost uniformly, suggesting a high degree of asymmetry in sibling lengths. The frequency distribution of branching angle asymmetry ($\lambda_\theta$) is biased towards the right, corresponding to perfect symmetry in both networks and similar to results for asymmetry in radii (statistical calculations are given in Table 4.1). That is, a parent vessel tends to branch into sibling vessels that are separated by equal branching angles. Intriguingly, the similarity of the pattern observed in radius asymmetry might suggest a correlation between the radius and the branching angle, providing motivation to investigate how branching angle depends on radius.

**Figure 4.3: Histograms or frequency distributions of the asymmetry ratios for radius ( $\lambda_r$), length ( $\lambda_l$), and branching angles ( $\lambda_\theta$) of vascular networks.** **(a)** mouse lung (1 individual) and **(b)** human head and torso (18 individuals). Note that radius and branching angle asymmetry ratios are both skewed towards perfect symmetry, whereas the length asymmetry ratio shows no skew and reveals much more asymmetry. **(c)** Histograms of branching angles for combined data of human and mouse networks appear to be unimodal both for $\theta_0$ and for $\theta_1$ & $\theta_2$ with peaks at 1.51 and 2.21 radians, respectively.

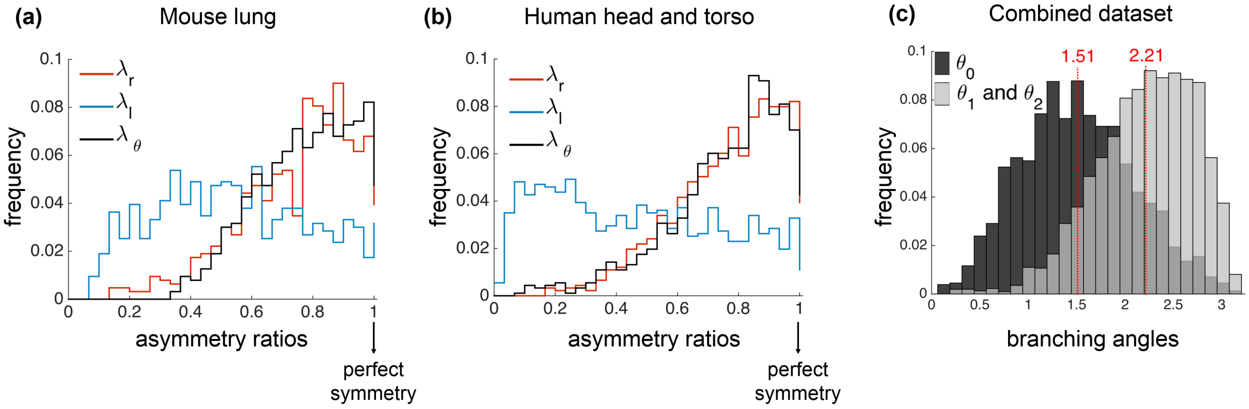

In addition to the asymmetry ratios explored above, we plot the histogram for the raw data on branching angles. Human and mouse networks show similar patterns, so we combine data for these two networks in our histogram plot (Fig. 4.3c). Analyzing the branching angle between the sibling vessels ($\theta_0$) and the branching angle between the parent and daughter vessels ($\theta_1$ and $\theta_2$) separately, we find unimodal distributions that peak at 1.51 and 2.21 radians, respectively. This shows that planar branching [192, 193] with orthogonal daughter vessels is frequent across the networks. Individual branching angle plots for mouse and human networks are given in S5a, b Fig.

Altogether, these network-level patterns for vessel radius, length, and branching angles hold across 18 different human subjects, different species (human and mouse), and different tissues (head and torso versus lung). Moreover, the radius and length asymmetries are consistent with findings in plants [100–102]. These results suggest that very general and ubiquitous selection pressures and developmental processes may shape the architecture of the vascular system across taxa, from humans to mice to plants, as well as across tissues, from lungs to head and torso.

### 4.3.2 Optimal branching patterns for material-cost (MC) optimization

In this section, we introduce the MC optimization results that include surface-area (MC-SA) and volume (MC-V) constraints. Here, we only focus on non-degenerate branching solutions—solutions that do not collapse to a vertex—and compare those with real data. The fraction of the non-degenerate and degenerate cases is provided in the S6 Fig.

#### Network-level comparison

Taking the radii and vessel endpoints from our real human and mouse vascular networks, we use the material-cost (MC) optimization solution provided above (Eq. (4.2.1)) to compute the optimal branching angle and length asymmetry at each branching junction. To compare predicted values to the real network structures presented in the previous section, we plot the distributions of $\lambda_l$ and $\lambda_\theta$ as well as the raw branching angle distributions for $\theta_0$ and $\theta_1$ & $\theta_2$. We find that all these properties are visually consistent across both networks and for both volume and surface-area constraints.

In particular, distributions of optimal $\lambda_l$ are close to uniform, whereas optimal $\lambda_\theta$ distributions are skewed towards perfect symmetry (Fig. 4.4a, b). Both of these match the general patterns of asymmetry in branching observed in Fig. 4.3. However, the degree of skewness in optimal $\lambda_\theta$ is sharper than the real $\lambda_\theta$ distributions, especially for the MC-SA. The statistical analysis of all these plots (including mean, median, skewness) are presented in Table 4.1.

**Figure 4.4: Histograms or frequency distributions of optimal asymmetry ratios for length ( $\lambda_l$) and branching angle ( $\lambda_\theta$) derived from material-cost (MC) optimizations.** Surface-area (MC-SA) results are shown as solid lines and volume (MC-V) results are shown as dashed lines for **(a)** mouse lung and **(b)** human head and torso.

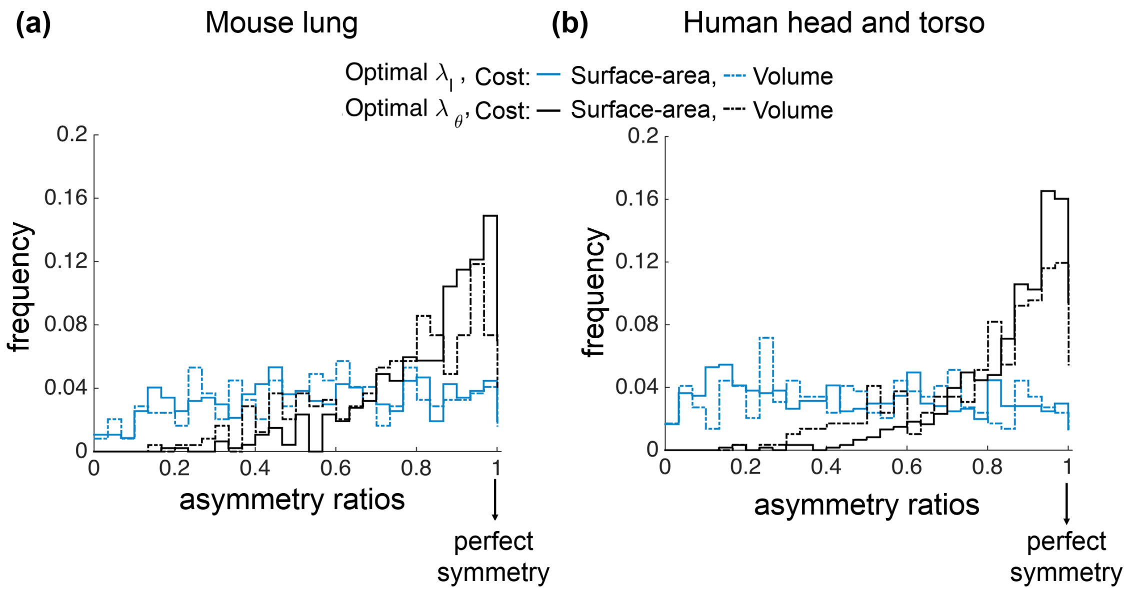

Next, we plot optimal $\theta_0$ and $\theta_1$ & $\theta_2$ histograms for the combined datasets (Fig. 4.5). We observe that optimal calculations yield unimodal distributions as in histograms of the real data. Optimal $\theta_0$ shows a mode around 1.79 radians, hence the optimal calculations are shifted towards larger values compared to the actual $\theta_0$ distribution that have a mode at 1.51 radians. In contrast, the peak for the uniform distribution $\theta_1$&$\theta_2$ at 2.24 radians almost matches the actual peak at 2.21 radians. The separate figures for human and mouse networks for each constraint are given in the S5 Fig. The full statistical analysis of branching angle histograms for the individual networks and the combined datasets are provided in the S3 Table.

**Figure 4.5: Histogram of optimal branching angles for combined data of human and mouse networks for material-cost (MC) optimizations.** All histograms appear to have unimodal characteristics both for $\theta_0$ and for $\theta_1$ & $\theta_2$ with respective peaks at **(a)** 1.79 and 2.25 for the surface-area constraint and **(b)** 1.79 and 2.24 for the volume constraint.

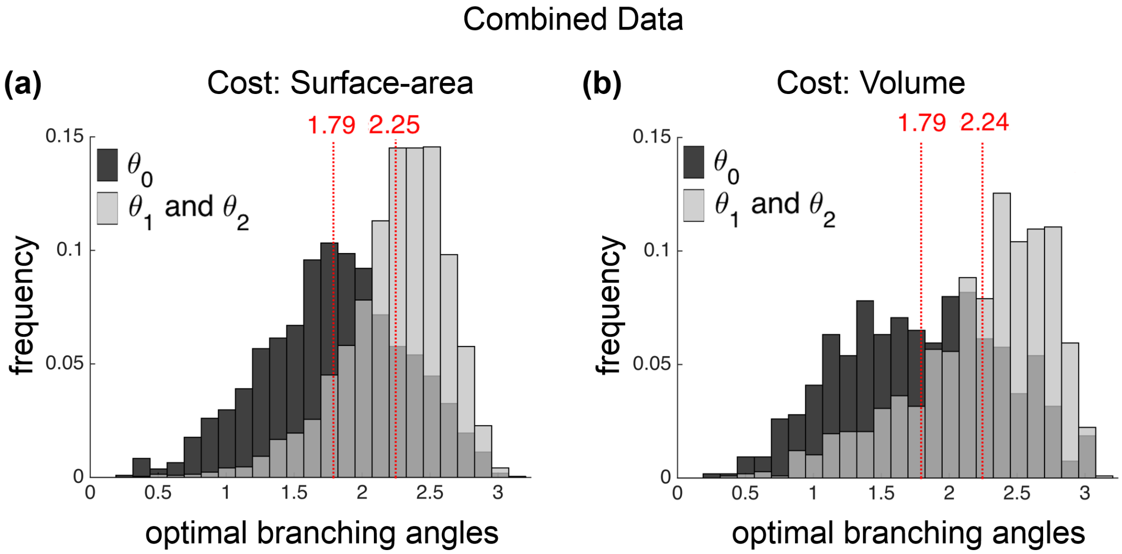

### Junction-level comparison

The previous section compares the network-level patterns of the optimal calculations and the empirical data. Here, we provide comparisons at local branching junctions for the MC optimizations. We plot actual versus optimal branching angles and calculate the Pearson correlation coefficient, which would be 1 if our predictions were always perfect. From the plots of branching angle for MC-V (Fig. 4.6) and MC-SA (S7 Fig) optimizations, we find that the predictions and the empirical data are weakly correlated (p-values <0.01). Moreover, we see that the volume constraint yields better agreement with data than the surface-area constraint at the junction-level. However, the correlation coefficients for both constraints indicate that the predicted optimal branching angles are a weak predictor of the actual branching angles at the local junction level. Consequently, it seems our theory needs further refinement or replacement.

**Figure 4.6: Junction-level comparison of optimal versus actual branching angles for the volume constraint of material-cost optimizations (MC-V). (a)** mouse lung and **(b)** human head and torso. The Pearson correlation coefficients and p-values are calculated for each plot.

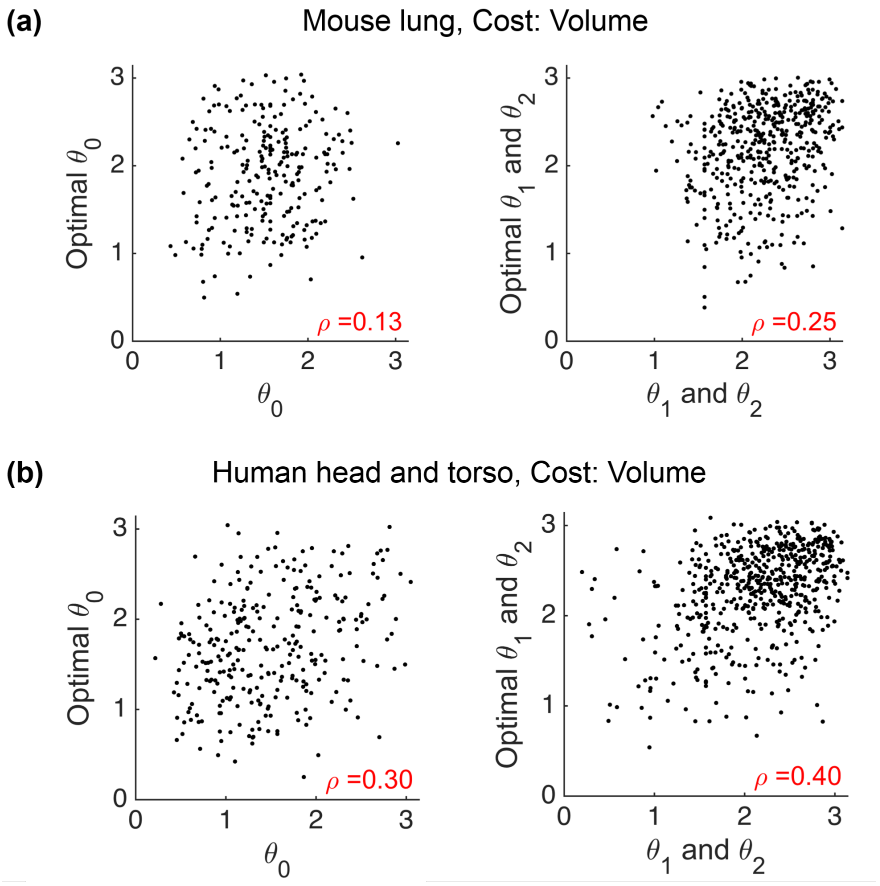

### 4.3.3 Analytical solutions for power-cost optimization beyond single branching (PC-1)

Now, we introduce the results for the solution of the PC-1 optimization. As described in the section presenting the PC-1 optimization scheme, we derive the approximate solution by considering a limiting case of the downstream impedances $c_1$ and $c_2$. With this method our solution predicts regions in the $c_1c_2$-plane separated by lines over most of the range of values. The regions in the $c_1c_2$-plane correspond to combinations of values that lead to branching geometries that are categorized as follows: collapse to daughter endpoint, collapse to parent endpoint, or no-collapse (i.e., a non-degenerate branching point).

Using the vessel endpoint and radius information from the real data, we predict the linear equations that form the boundaries between these regions, and we label them according to the categories of solution described above (Fig. 4.7). As a further check, we compute numerical solutions at each discretized point in the $c_1c_2$-plane and mark different categories of solution by different colors. We examine two examples, corresponding to symmetric (Fig. 4.7a, b) and asymmetric (Fig. 4.7c, d) parameter values. Both show that our approximate analytical solution matches the numerical solution extremely well. On closer inspection, it is clear that the different regions and categories are not separated via purely linear functions across the entire plane, but instead the boundaries are curved for small values of $c_1$ and $c_2$ (Fig. 4.7b, d). This result reveals a mismatch between the analytical and numerical solution at the smallest scales, i.e., vessels close to the capillaries, which is exactly where our solutions should fail based on the limits of our approximation scheme.

**Figure 4.7: Comparison of approximate solutions with numerical solutions for the PC-1 (power-cost (PC) optimization beyond single branching).** Approximate solutions define linear boundaries on the $c_1c_2$-plane between different categories of the solution space: collapse to daughter endpoint, collapse to parent endpoint, and no-collapse. The different categories calculated from numerical simulation are marked by different colors as indicated in the figure. **(a)** An example of symmetric branching in vessel radius with parameter values: $|V_0V_1| = |V_0V_2| = |V_1V_2| = 1$, $r_0 = 1.20$, $r_1 = 1$ and $r_2 = 1$, where $c_1$ and $c_2$ take values in the range $[0, 20]$. **(b)** Zoomed version of (a) into the plane $[0, 2] \times [0, 2]$ with the same resolution as in (a). **(c)** An example of asymmetric branching in vessel radius with parameter values: $|V_0V_1| = 0.8$, $|V_0V_2| = |V_1V_2| = 1$, $r_0 = 1.1$, $r_1 = 0.85$, and $r_2 = 1$, where $c_1$ and $c_2$ take values in the range $[0, 20]$. **(d)** Zoomed version of (c) into the plane $[0, 2] \times [0, 2]$ with the same resolution as in (c).

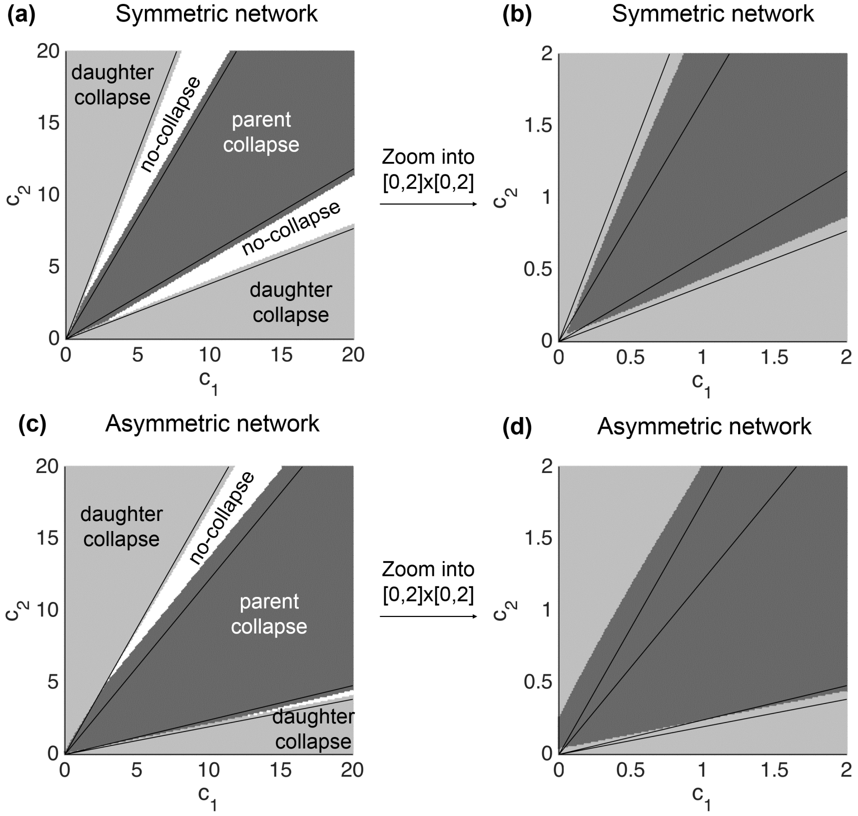

### 4.3.4 Network-level results of randomly branching networks with local to global constraints

Lastly, we compare our empirical results for network-level characteristics of branching angles and length asymmetries to results from simulated randomly branching networks with local to global constraints. Because mouse and human networks yield similar results, we only present results for the mouse in the main text. Random simulation results for the human subjects are given in S8 Fig.

As in the empirical data, random simulations with local to intermediate constraints yield uniform distributions for asymmetric length ratio ($\lambda_l$), whereas the branching-angle asymmetry ratio ($\lambda_\theta$) is skewed towards symmetry (Fig. 4.2). In contrast, the fully global constraint generates branching networks with distributions skewed towards symmetry for both $\lambda_l$ and $\lambda_\theta$, inconsistent with empirical data (Fig. 4.2). Further statistical comparisons with empirical data and optimal branching results are presented in the next section.

### 4.3.5 Comparison of optimal branching, random branching, and empirical data

To provide a rigorous comparison across different MC optimizations (surface-area and volume) and spatial constraints (local to global) with the empirical data, we compute the statistical properties— mean, standard deviation (SD), skewness and standard error for each—of the resulting asymmetry distributions in Table 4.1. Additionally, we use the Kullback-Leibler divergence measure (KL) to quantify the distance between the empirical asymmetry distributions and the optimization or random-simulation asymmetry distributions. We determine p-values by performing bootstrap samples up to half the size of the real data [194]. By definition, a p-value is equal to 1.00 for a comparison of the real data with itself because that implies an exact match in the distributions.

There are several conclusions based on these results. First, the random branching simulations that are globally constrained do not produce results that are statistically similar with mouse lung or human head and torso in terms of length asymmetry. In addition, the intermediate 2 constraint on random branching—where spheres are used to determine the branching locations, Fig. 4.2—poorly matches with real data in terms of both length and branching angle asymmetries for the human head and torso network.

Except for the global constraint, results for the mouse lung network reveal that the random branching simulations perform as well as the MC optimizations in terms of the general

**Table 4.1:** Statistical comparison of material-cost (MC) optimizations and random spatial constraints with empirical data.

| | | length asymmetry ($\boldsymbol{\lambda_l}$) | | | | branching angle asymmetry ($\boldsymbol{\lambda_\theta}$) | | | |
|---|---|---|---|---|---|---|---|---|---|
| | | Mean ± SE | SD ± SE | Skewness ± SE | KL p-val | Mean ± SE | SD ± SE | Skewness ± SE | KL p-val |
| real network | mouse lung | 0.53 ± 0.00 | 0.25 ± 0.00 | 0.13 ± 0.00 | 1.00 | 0.76 ± 0.00 | 0.16 ± 0.00 | -0.43 ± 0.00 | 1.00 |
| Material-cost optimizations | surface-area | 0.54 ± 0.00 | 0.27 ± 0.00 | -0.07 ± 0.00 | 0.01 | 0.82 ± 0.00 | 0.16 ± 0.00 | -1.28 ± 0.00 | 0.00 |
| | volume | 0.54 ± 0.00 | 0.27 ± 0.00 | -0.09 ± 0.00 | 0.00 | 0.74 ± 0.0 | 0.20 ± 0.00 | -0.79 ± 0.00 | 0.01 |
| randomly simulated networks | local | 0.56 ± 0.01 | 0.25 ± 0.00 | -0.10 ± 0.04 | 0.61 | 0.65 ± 0.01 | 0.24 ± 0.00 | -0.43 ± 0.04 | 0.26 |
| | intermediate 1 | 0.56 ± 0.01 | 0.25 ± 0.00 | -0.09 ± 0.05 | 0.59 | 0.68 ± 0.01 | 0.22 ± 0.00 | -0.54 ± 0.07 | 0.64 |
| | intermediate 2 | 0.57 ± 0.01 | 0.24 ± 0.00 | -0.12 ± 0.05 | 0.11 | 0.63 ± 0.01 | 0.23 ± 0.00 | -0.38 ± 0.06 | 0.00 |
| | global | 0.76 ± 0.01 | 0.22 ± 0.01 | -0.85 ± 0.07 | 0.00 | 0.71 ± 0.01 | 0.26 ± 0.01 | -0.65 ± 0.06 | 0.00 |
| real network | human head and torso | 0.46 ± 0.00 | 0.28 ± 0.00 | 0.24 ± 0.00 | 1.00 | 0.75 ± 0.00 | 0.19 ± 0.00 | -1.05 ± 0.00 | 1.00 |
| Material-cost optimizations | surface-area | 0.46 ± 0.00 | 0.29 ± 0.00 | 0.16 ± 0.00 | 0.76 | 0.85 ± 0.00 | 0.14 ± 0.00 | -1.68 ± 0.00 | 0.00 |
| | volume | 0.48 ± 0.00 | 0.28 ± 0.00 | 0.11 ± 0.00 | 0.00 | 0.78 ± 0.00 | 0.19 ± 0.00 | -0.97 ± 0.00 | 0.00 |
| randomly simulated networks | local | 0.54 ± 0.01 | 0.27 ± 0.00 | -0.07 ± 0.03 | 0.00 | 0.63 ± 0.01 | 0.28 ± 0.00 | -0.48 ± 0.03 | 0.00 |
| | intermediate 1 | 0.53 ± 0.01 | 0.26 ± 0.00 | 0.00 ± 0.05 | 0.00 | 0.66 ± 0.01 | 0.26 ± 0.00 | -0.64 ± 0.05 | 0.00 |
| | intermediate 2 | 0.59 ± 0.01 | 0.24 ± 0.00 | -0.24 ± 0.05 | 0.00 | 0.62 ± 0.01 | 0.23 ± 0.00 | -0.34 ± 0.04 | 0.00 |
| | global | 0.75 ± 0.01 | 0.22 ± 0.01 | -0.80 ± 0.05 | 0.00 | 0.70 ± 0.01 | 0.26 ± 0.01 | -0.59 ± 0.05 | 0.00 |

characteristics (i.e., the first few moments—mean, SD, skewness) of the distributions. In contrast, for the human head and torso, the MC optimizations yield overall better agreement with the real data than the random simulations, especially for length asymmetry. This finding is consistent with the KL significance test. Based on the KL p-values, we observe that all of the random branching simulations do not do a good job of matching the real data for human networks. However, it suggests that vascular branching derived from MC-SA does reasonably well at recreating length asymmetry patterns that are similar to real human data. In contrast, the mouse lung compares more favorably with the random-branching simulations at local and intermediate scales than it does with the MC optimizations (Table 4.1).

## 4.4 Discussion

By performing a high-quality analysis of angiographic images from mouse lung and human head and torso via the new software Angicart [5], we identified systematic patterns in the branching asymmetry of the vascular system. Specifically, the radii and branching angles of sibling vessels tend to be symmetric, while the lengths of sibling vessels tend to be asymmetric. These results show that modern allometric theories make core assumptions about symmetric branching—sibling vessels at a single branching junction have identical properties such as radius, length, and flow rate— in the vascular system that do not match empirical data, especially in terms of the asymmetry in vessel lengths. Thus, future work should be done to incorporate levels of asymmetry into theory that are similar to those observed in real data or to determine the best procedure for finding an effective, symmetrically branching network that has the same allometric properties as the asymmetric networks in real systems. Accomplishing this theoretical advance should also prove helpful in resolving the current mismatches between theoretical predictions and empirical measurements of metabolic scaling exponents. Indeed, we are involved in future work to map and compare the space of possible allometric scaling exponents both theoretically and empirically for these asymmetrically branching networks.

Importantly, the observed, systematic patterns in asymmetric vascular branching suggest there may exist underlying biological principles that vary in selection strength and across spatial scales yet effectively constrain the structure of the vascular system. In this study, we focus on MC (material-cost) and PC (power-cost) optimizations that have long been postulated as evolutionary principles that play a critical role in the formation of the vascular system [89, 105, 106]. We provide a consistent and robust framework for studying these optimization principles and for discovering possible associations with the asymmetry patterns observed in the real data.

In this research, we examined local optimization and for the first time presented solutions for the MC optimization that are more complete than formulae from previous studies that are not optimal in every case or can be easily misidentified or misinterpreted. We have further shown that solutions predicted from MC optimizations match the network-level asymmetry patterns for lengths and branching angles observed in the real data but are a weak predictor of vascular branching at the junction-level. Following this, we built a PC optimization scheme that is consistent with the basic rules of fluid dynamics and corrects inconsistencies about fluid mechanics—incorrectly summing impedances in series and parallel—from previous work. Based on the correct fluid mechanics relationship, we find for single branching junctions that one vessel is always sufficiently costly to be completely eliminated and have no branching at all. Of course, repeating this solution at each junction throughout the network will result in a single vessel or a single hub at the heart for the entire cardiovascular network, which is unrealistic because it violates the need to efficiently distribute blood throughout the body [80, 81, 87, 89, 176]. Consequently, based on our new analysis, we conclude that optimization of flow and power loss at a single branching junction (i.e., PC-0 optimization) will always lead to the elimination of branching and thus lead to meaningless predictions of angles and lengths of vessels in branching networks.

We also note that another problem with local optimization is that it is not robust for these more complicated branching architectures. That is, the optimization of the power cost through a whole network (global) would be affected by changes in the flow dynamics at even a single local branching [13]. Hence, obtaining an efficient distribution of flow to optimize energy cost across a whole network would necessitate global changes in network structure if there is even a single change at the local level of a branching junction. This effect is considered by Katifori et al. [25] when deriving optimal leaf venation networks that provide robustness to damage as an evolutionary advantage for leaf survival.

In an attempt to connect vascular branching asymmetry with the efficient flow mechanisms, we included multiple downstream vessels and branching junctions as part of the PC optimization (i.e., PC-1 optimization) to determine the optimal placement of each individual branching junction. This in turn indicates the need to consider constraints beyond just the local spatial and branching junction scale. Although this is additional work, it has the advantage that capillaries are at a uniform pressure so that the full downstream vascular tree below each daughter vessel has a symmetric pressure drop, thus simplifying the optimization problem. Alternatively, the model could be improved by allowing asymmetric pressure drops across sibling vessels that could lead to plausible (i.e., non-degenerate) solutions even when locally optimizing the flow. However, determining these pressure drops would also require considering effects from multiple branching junctions when calculating the placement of a single branching junction. Furthermore, our results from these more intermediate-scale calculations reveal that plausible explanations and predictions for branching angles and length asymmetry can be obtained by incorporating vessels beyond a single branching junction. Thus, from any perspective, we argue that local-scale optimization principles and constraints are insufficient to understand and predict asymmetric branching patterns, which is in strong contrast to many previous results for symmetric branching that can be fully treated at the local scale or at a single branching junction.

Although the MC optimization results match empirical data at the network-level, the junction-level comparisons show that a strictly local constraint is unlikely to be the major driving determinant of the vascular structure. Further evidence for the possible inadequacy of local constraints is the fact that the PC optimization scheme does not lead to any realistic branching at all. Therefore, we enlarged the scale of spatial constraint and the number of branching junctions involved in the optimization in order to incorporate more information.

There is no a priori reason that evolutionary constraints should only apply at local spatial scales, and as just explained, our optimization results suggest that local spatial constraints do not fully explain the existence of the observed asymmetric branching patterns. Moreover, developmental processes likely occur at local to intermediate scales but in a more random manner than evolutionarily programmed branching in response to optimality constraints. Thus, to investigate the role of randomness and of spatial constraints on vascular structure, we considered random simulations of the branching network with spatial constraints that varied from local to global, including two types of constraints at intermediate scales. We found that the global constraint performs poorly, whereas the intermediate or local constraints provided reasonable matches to the network-level observations from real data. Here, the intermediate constraints are especially important to consider because they incorporate the downstream impedance as in our improved PC optimization scheme.

Our statistical analysis compares network-level asymmetry from empirical data to optimal predictions and randomized results. We show that random simulations and MC optimizations capture important features of the vascular branching for the mouse lung network. For the human head and torso, we find that only MC optimizations succeed at capturing the dominant features of asymmetry in vascular branching. This difference as in result from the mouse lung vasculature may arise because the human head and torso data were obtained using MRI and correspond to vessels of larger sizes that must deliver blood from the heart to the rest of the body and thus may be more programmed to follow a defined branching pattern. In contrast, the smaller-sized vessels imaged by micro-CT in the mouse lung may be filling space but with a structure that requires weaker constraints on the patterns of asymmetry in vascular branching. These smaller vessels are also likely formed due to developmental processes with more random spatial constraints such as branching triggered by VEGF signaling or locations determined by the point of the highest gradient in shear stress. Lastly, our results are intriguing because an intermediate spatial scale has been found to be the correct spatial scale for recreating pervasive patterns founds in urban studies on cities [195].

Finally, we note other attempts for understanding the architecture of the vascular systems or other types of transportation networks. In modern allometric theories with symmetric vascular branching, space-filling principles [11, 79]—a simple encapsulation of the need of the vascular system to span the entire body and have capillaries close to all cells—is the core assumption that determines the distribution and scaling of vessel lengths. Algorithms [98] have been proposed that are space filling and reproduce some of the asymmetric patterns described here. These algorithms optimize at both local and global scales within non-spherical spaces. That research does not explicitly include radius information so joining these approaches into a single framework may be a fruitful future direction. Another study by Durand et al. [196] is also noteworthy for its analysis of optimal transport networks that minimize the resistance to flow in a special case of a constant total volume and surface area across the network.

Taken together, our findings suggest that combinations of biological principles that are applied at the intermediate and local level could eventually lead to the systematic patterns for branching angles and length asymmetry observed in real data. We infer that physical constraints, developmental processes, evolution and optimization principles play a role in determining vascular structure, but in contrast to previous work [79–81, 83, 105, 106], we find that the strength and relative importance of these roles likely also depends on the spatial scale, number of branching junctions, vessel sizes, and possibly tissue type. As a result, our work suggests further exploration of optimal branching at local and intermediate spatial scales in a way that combines and integrates multiple optimization principles.

## 4.5 Materials and Methods

### 4.5.1 Processing of angiographic images, vessel extraction with Angicart software, and resolution of data

In our study we analyze the cardiovascular structure of mouse lung and human head and torso by processing the three-dimensional stacks of images via the software Angicart [29]. Mouse lung images are collected through the microtomography (micro-CT) [44], whereas human head and torso images from 18 different subjects are obtained through MRI [29, 43]. The detailed image acquisition for each dataset are given in [44] and [29].

In our study we analyze the cardiovascular structure of mouse lung and human head and torso by processing the three-dimensional stacks of images via the software Angicart [5].

Mouse lung images are collected through the microtomography (micro-CT) [184], whereas human head and torso images from 18 different subjects are obtained through MRI [5]. The detailed image acquisition for each dataset are given in [184] and [5]. Here, we present how these images are processed to extract the vascular geometry. Before processing the tomographic images in Angicart, the images are first downsampled to reduce the noise and decrease the processing time. Angicart relies on the manual input of the intensity threshold parameter between 0 and 1 to identify the set of voxels belonging to the vascular network. For each set of data, the intensity threshold has been chosen by the visual inspection of blood vessels, conducting the sensitivity analysis as well as identifying the percentage of the possibly misclassified vessels as presented in Newberry et al. [5]. All these steps are done to smooth or reduce the noise in the data. The details on the preprocessing steps, set of thresholds, as well as the version of the software in regards to these criterions are given in the Supplementary Material. Performing Angicart on the angiographic images extracts the branching network topology with the vessel characteristics such as positional coordinates, radius, length, number of children. The output of the Angicart for each dataset is available in S1 Dataset.

We also note that different imaging modalities can lead to different imaging qualities and that the level of spatial scales that they can identify varies. Because micro-CT provides higher resolution images than MRI, the vessel sizes identified in the mouse lung are substantially smaller than the vessel sizes identified in the human head and torso data (>10 microns versus >1mm). These differences have the advantage of allowing us to investigate the branching geometries for large versus small vessels as well as pulsatile versus viscous dissipation flow regimes [11,87,176]. Moreover, the difference in the quality of different medical imaging techniques inevitably affects the amount of noise in the data. Possibly misidentified vessels from the Angicart output are characterized by defining non-deformed vessels—more than 10% of the volume of voxels of the vessel lies inside a distance of radius+1 voxel from the centerline of the corresponding vessel. We find that the fraction of carefully classified, non-deformed vessels is greater in the mouse lung data compared to the human head and torso data (S2 Table), meaning it is of higher quality on average, as expected from the image resolution properties of micro-CT and MRI. This realization makes it especially noteworthy that the mouse lung data exhibits the strongest signal of random branching, which we can confidently say is not due to effects of noise but to actual branching patterns (see 4.3 Results, 4.3.5 Comparison of optimal branching, random branching, and empirical data).

### 4.5.2 Computing branching angles from extracted vessel skeleton

To calculate our three branching angles (Fig. 4.1c) using our empirical vessel measurements, we first must specify the three intersecting lines that define the angles. One endpoint is common to all three lines, representing the branching junction ($j$) that connects the parent to the two daughter vessels. Therefore, the remaining choice is in how to define the other endpoint of all three vessels. In principle, this could be done using points along the vessel that are very close to the branching junction ($j$), the midpoint between the branching junction and the other vessel endpoint, or the exact endpoint of the other vessel. For a perfectly straight vessel, this choice will have no effect on the computed branching angle, but for curved or tortuous vessels, which are common in real vascular systems, these choices will lead to different values for the branching angles. For this study, we choose the exact endpoints of the vessels to define the straight lines that define the angles (S9 Fig). We do this for three reasons. First, we relate branching angles to vessel lengths, which are defined relative to the endpoints, so these relations will be most faithful if we use lines corresponding to the full length of the vessel. Second, we argue there is more of a constraint on the endpoints of vessels than the exact path they take to reach those points, which may include more developmental stochasticity. Third, there is no arbitrariness to the choice of vessel endpoints, whereas choosing 1 pixel versus 5 pixels away from the branching junction is more subjective. Using our choice of lines and endpoints, we calculate the magnitude of the angles between the straight lines defined by the positional coordinates—the endpoint coordinates of the vessels $V_0$, $V_1$, $V_2$, and $j$—at the bifurcation as shown in Fig. 4.1c, d.

## 4.6 Acknowledgements

We thank Kristina Bostrom for providing the micro-CT images of mouse lungs used in this study, and Daniel Ennis, J. Paul Finn, and Derek Lohan for providing MRI images of human head and torso used in this study. We also thank Kathryn Burch, Benjamin Demaree, Maya Josyula, Edward Hu, and Quinten Lepak for their work on this topic.

# CHAPTER 5

# Discussion and Conclusions

In the above chapters, we study emergent patterns in drug interactions and cardiovascular system by recognizing them as networks that possess different features. Here, drug interactions provide a subtle framework for the exploration of interaction-based networks—where the whole-system behavior emerges as a consequence of the interaction among its components. On the other hand, the vascular system offers a fine setup for examining the structural properties of the flow-transmitting networks as well as investigating whether certain structural properties of branching structures are driven deterministically or stochastically across different spatial constraints. Below, we provide a concise summary of our findings and present plentiful future directions to proceed in exploring more of the current network categorizations as well as adapting them to broader contexts.

### 5.0.1 Higher-order and Emergent Drug Interactions

Previous considerations of multi-component systems have often disregarded the significance of higher-order (more than two component) interactions, and mainly focused on the pairwise associations as a way to capture the dynamical outcomes of the complex systems. Thus, extensive studies of higher-order interactions, and a decent understanding of higher-order affects have been lacking. In this study, Chapter 2 and 3 are devoted to introducing a conceptual and theoretical framework for the classification of higher-order interactions. In doing so, we primarily present an explicit distinction between the *net interaction*—combined effect relative to independent single component effects—and any *emergent interaction*—combined effect that cannot be predicted from lower-order effects (Fig. 1.4). To uncover emergent interactions, we derive a framework to calculate expectations for three-way interactions based on the measured impact of each individual component and of each pairwise interaction. In Chapter 2, using our framework and the experimental system of drug interactions—where the data consists of *Escherichia coli* treatments with all possible triple combinations of 6 antibiotics—we find that i) emergent antagonisms are more common than emergent synergies, and ii) emergent antagonisms are more common and emergent synergies are more rare than would be inferred from measures of net effects that do not disentangle pairwise interactions from three-way interactions. Moreover, we show that standard statistical methods such as three-way ANOVA are not equivalent to the emergent interaction metric derived in our study, and results obtained by ANOVA on the log-transformed data are consistent with identifying emergent antagonism, but not for emergent synergism (Appendix A, Chapter 2).

With the recent advances in theory and experiment for higher-order drug interactions presented in Chapter 2, we are now able to search for emergent interactions. In regards to detecting synergies and antagonisms—enhanced and diminished effects compared with no-interaction (i.e., additive) effects, respectively—previous work has shown that this classification is easier when a rescaling method is applied to the interaction metric (see Chapter 1). However, no study has carefully examined whether new types of normalization might be needed for emergence. In Chapter 3, we propose several rescaling methods for enhancing the classification of the higher-order drug interactions based on our conceptual framework. To choose the rescaling that best separates synergism, antagonism, and additivity, we conduct bacterial growth experiments in the presence of single, pairwise, and triple-drug combinations among a broader set of antibiotics (14 drugs in total) than Chapter 2. We find one of our rescaling methods is far better at distinguishing synergistic and antagonistic emergent interactions than any of the other methods. Using our new method, we find around 50% of emergent interactions are additive, much less than previous reports of greater than 90% additivity. We conclude that higher-order emergent interactions are much more common than previously believed, and we argue these findings for drugs suggest that appropriate rescaling is crucial to infer higher-order interactions.

Our study covers interactions among higher-order drug combinations that are fixed in their concentrations. Alternatively, one can also define drug interactions based on the pathogen response profile when drug concentrations are varied simultaneously. Interactions over a full concentration gradient can offer more comprehensive assessment of the effect from combination therapies, however it requires a substantial effort in collecting extensive amount of detailed data. Moreover, several studies have considered extending Loewe Additivity by simply adding an effective concentration for the third drug or to all higher-order combinations [70]. For three drugs, this natural extension corresponds to mapping additivity (i.e., no interaction) strictly to a plane defined by $\frac{C_X}{C_{X,\mathrm{MIC}}} + \frac{C_Y}{C_{Y,\mathrm{MIC}}} + \frac{C_Z}{C_{Z,\mathrm{MIC}}} = 1$. This methodology suggests antagonism when the sum of the effective concentration terms across all drugs exceed 1, and synergy when it is the opposite case. However, this approach does not provide information about the emergent behavior as it simply assesses the comparison of the $N$-drug combined effect with respect to the single-drug effects, and hence lacks comparison to pairwise and other levels of effects that are needed for the evaluation for the emergent interaction. Consequently, establishing a measure to quantify concentration dependent emergent interactions offers natural future direction to our emergent interaction framework. Accomplishing this would be highly valuable in deciding useful treatment strategies.

Moreover, the framework developed in this study for the drug interaction networks offers potential application to other biological networks to uncover higher-order, emergent interactions in multi-way component systems. Further applications include protein and gene interaction networks, multiple predator effects, food webs, and social networks. Despite the fact that some similarities exist across different systems, each system has its own characteristics, and the functional forms of the response phenotypes will vary accordingly. Hence, further study is required for developing and revising models so that we can examine higher-order interactions properly in a wide range of systems. Indeed, we are involved in a future work to systematically compile and analyze datasets from different interaction-based network settings. This involves compiling a huge database from stressor interactions and contrasting our findings with the previous reports of interactions. Extending our framework to other complex systems could conceivably make an important contribution towards acquiring comprehensive insights and developing models that realistically represent the dynamics of systems consisting of many different and connected parts.

### 5.0.2 Emergent Properties in Cardiovascular Networks

Modern models that derive allometric relationships between metabolic rate and body mass are based on the architectural design of the cardiovascular system and presume sibling vessels are symmetric in terms of radius, length, flow rate, and pressure. However, these studies have been limited by the lack of extensive, detailed data to test these assumptions. Moreover, predictions from those models infer power-law or second-order concave curvature relationship in log-log space, whereas recent allometric scaling studies with a large set of data yield convex curvature. This suggests the need to test the validity of the model assumptions. In this respect, in Chapter 4, we study the cardiovascular structure of the human head and torso and of a mouse lung based on three-dimensional images processed via our software Angicart. In doing so, we also provide a brief background on ways to collect vascular network data via different imaging data types that vary in their resolution and techniques of extracting the data.

In contrast to modern allometric theories, we find pervasive patterns of asymmetry in vascular branching. In particular, we observe that the level of asymmetry varies across different features, such as vessel lengths that exhibit high levels of asymmetry, whereas radius and branching angles tend towards symmetry. Subsequently, we explore whether these pervasive patterns result due to an optimization of certain properties that are constrained by natural selection or due to successive random branching processes. Consideration of these hypotheses also brings about a question about which spatial or network-level scales are optimized or random. For the optimized network hypothesis, we build a framework to derive predictions based on local, junction-level optimality principles: 1. material-cost optimizations (construction materials or blood volume) and 2. optimization of efficient flow via minimization of power loss. We show that material-cost optimization solutions match with distributions for asymmetric branching across the whole network but do not match well for individual junctions. Moreover, we find that correctly implementing the power-cost optimization at the local spatial scale eliminate one of the branching vessels, leading to a degenerate branching. Thus, we further construct power-cost optimization scheme at the intermediate spatial scale and see that incorporating information beyond the local branching can lead to plausible conclusions. Consequently, we also explore random branching that is constrained at scales that range from local (junction-level) to global (whole network). This allow us to investigate the role of randomness for vascular branching as well as the degree at the spatial scales are important. We find that material-cost optimizations are the strongest predictor of vascular branching in the human head and torso, whereas locally or intermediately constrained random branching is comparable to material-cost optimizations for the mouse lung. These differences could be attributable to developmentally-programmed local branching for larger vessels and constrained random branching for smaller vessels.

In summary, we provide an exploration of spatial scales and constraints that could yield the empirical data patterns we observe in real data, and we find that whether the branching is more stochastically or optimally determined depends on the number of branching junctions involved, vessel sizes, and possibly tissue type. Therefore, we further plan to explore the optimal branching at local and intermediate spatial scales in a way that combines and integrates multiple optimization principles. Moreover, our findings suggest that randomness plays a key role at the local spatial scale, implying that delivering blood flow is mainly fulfilled by filling out the space through random branching. This brings about an interesting question on whether the degree to which optimization or randomness determines vascular branching may differ in genetically identical species, such as clones or monozygotic siblings. In this sense, randomness would be expected to differ more, whereas the optimal constraints would be expected to differ very little. In this sense, a remarkable study of armadillos, which naturally produce four to six monozygotic offspring as littermates in each birth, by Glenny et al. [197] have investigated how much of the variation in the vascular branching is due to non-genetic or environmental factors. By contrasting the spatial distribution of blood flow in the pulmonary vascular system across offspring within the same litter and across different litters, they find that around 67% of the variation is due to genetics. Future work of examining the role of natural selection and randomness across different spatial scales with this experimental setup and our mathematical framework could offer a more rigorous explanation for the structural differences in vascularity between genetically identical species.

Next, going back to the origins of allometric scaling theories, a recent paper [103] has shown that deviation from the perfect symmetry assumption can result in a wide range of metabolic scaling exponents. Moreover, it demonstrates that certain degrees of asymmetry can lead to the 3/4 exponent as in the original WBE allometric scaling theory. These model simulations offer promising research directions to account for the deviations from power-laws by incorporating levels of asymmetry measured from empirical data analysis and computed from theory. Thus, accomplishing this theoretical advance would be helpful in resolving current mismatches between theoretical predictions and empirical measurements of metabolic scaling exponents.

## 5.1 Overall Summary

All in all, this thesis studied systems with different network types, mainly within the context of interaction-based networks and vascular networks. In doing so, we have provided a succinct yet powerful framework to elucidate our rich set of questions and approaches for resolving the emergent patterns in complex systems. In particular, the first part of this work offers a conceptual and theoretical foundation to distinguish net interactions from emergent ones at all levels based on a model system of drugs combined at fixed concentrations. We conclude that emergent interactions are common in three-drug combinations, and that there are abundant antagonistic emergent interactions as compared to emergent synergies. Moreover, we anticipate that the agenda presented here on the higher-order drug interactions will provide a set of abstract mechanisms to explore various systems governed by similar complex dynamics. In the second part, we have characterized pervasive patterns in the structural properties of vascular networks and worked on modelling these patterns based on biological and physical principles, and investigated the randomness of these properties across distinct spatial scales. Our study provides promising advancements as it provides a useful contribution to the field that will guide how to analyze large datasets for vascular branching, to derive predictions for vascular branching by developing mathematical frameworks, to perform simulations to test experiments on random vascular branching, as well as to compare results from different models. All these methods combined, we expect to greatly expand our knowledge about vascular systems and create new insights about vascular branching and allometric scaling.

# APPENDIX A

# Analysis of variance (ANOVA) method for testing interactions

In studies of multi-way interactions among other stressor systems ANOVA has been a prominent method used to analyze and obtain results from empirical datasets [198]. Here, we provide a review of two-way and three-way ANOVA and how they translate into a metric for the prediction of interactions. In doing so, we also present a comparison of ANOVA with the drug interaction metrics that are defined for two- or higher-order drug interactions—deviation from additivity (DA) and emergent three-way interaction (E3) measures (see details in Chapter 1.1, 2, and 3).

### Two-way ANOVA

The simplest form of interactions that involve only two stressors (denoted by $X$ and $Y$ as in our notation in the above chapters (Chapter 2 and 3, where drugs are stressors for the bacterial growth) is quantified by 2x2 factorial design with four different observations. That is, the observations include no stressors, stressor $X$ alone, stressor $Y$ alone, and stressors $X$ and $Y$ together, with corresponding response variable measurements $M_O$, $M_X$, $M_Y$, and $M_{XY}$. In this case, factorial ANOVA (or equivalently two-way ANOVA) tests for an interaction between $XY$ by quantifying the significance of deviation from the additive effects of 2 stressors (or factors). Typically, in factorial ANOVA, a factor $X$ is said to have no interaction with the other factor $Y$, if the linear effect achieved by $X$ as compared to the control (no factors present) on the dependent variable ($M$) is the same as the linear effect when the factor $Y$ is present [14]. This notion is well represented by assigning one factor (say $X$) to the horizontal axis (x-axis), and varying the level of the other factor ($Y$) by different lines on the response plot (Fig A1). As the change in x-axis or the denominator of linear slope are always assumed to be the same, ANOVA reduces to the assumption that the change in y-axis (dependent variable m) is the same between the observations of $O$ to $X$ and $Y$ to $XY$, meaning that

$$M_O - M_X = M_Y - M_{XY} \tag{A.0.1}$$

Consequently, the no-interaction case corresponds to the expectation that the combined stressors yield a response measurement of $M_{XY} = M_X + M_Y - M_O$. By subtracting the response variable for the no stressor case ($M_O$) from both sides of the equation, one can write this as

$$(M_{XY} - M_O) = (M_X - M_O) \ + (M_Y - M_O) \tag{A.0.2}$$

Defining the response variables relative to the response of the control scenario, ANOVA tests for the additive effects of two stressors relative to the no-stressor case (Eq. (A.0.2)). Thus, statistically significant deviation from the null model of additivity suggests interaction between stressors.

**Figure A.1:** **(a)** Two-way ANOVA design. When the linear curves are parallel (Eqs (A.0.1) and (A.0.2) hold), or equivalently when the change in the response variable is independent of the presence or absence of the second factor $Y$, then ANOVA identifies that $Y$ has an additive effect, meaning that $X$ and $Y$ are not interacting. **(b)** Three-way ANOVA design. The graph in the panel (a) is now reproduced with the third factor ($Z$), where it illustrates the two-way interaction between $X$ and $Y$ when the third factor is present. Three-way ANOVA quantifies the statistical significance of change in the amount of two-way interaction across $Z$'s absence (panel (a)) and $Z$'s presence (panel (b)) [14].

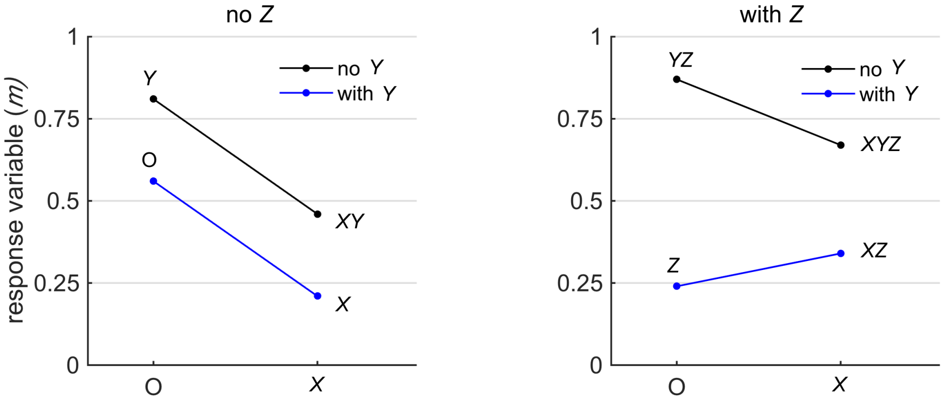

This underlying additive model of ANOVA, however, is not informative when the stressors alone have large impacts on the response variable, hence resulting in an additive expectation that can never be achieved. This argument is nicely outlined in Sih et al. [30] that studied multiple predator systems—where the survival rates of prey species in the presence of multiple predators determines the interactions between predators. When predator $X$ alone, and $Y$ alone kills 60%, and 70% of the prey, respectively, then ANOVA tests for an additive effect corresponding to an expectation that predators $X$, $Y$ together kill 130% of the prey, which can never be true. To overcome this hurdle arising due to the additive model, a multiplicative model is introduced by Soluk and Collins [151] that defines the null model of no-interaction based on the product of prey survival rates. In other words, when predators $X$, $Y$ are independent of each other, then it is expected that the survival rate of prey in the presence of $X$, $Y$ together is simply equal to $M_{XY} = M_X M_Y$. For the above example, where $M_X = 0.40$, and $M_Y = 0.30$, then the surviving proportion of prey population is simply equal to $M_{XY} = 0.40 * 0.30 = 0.12$, hence the expected proportion killed with multiple predator presence is 88%, yielding a plausible expectation value that can be tested. This always holds true because the survival rates take values between 0 and 1. Note that MPE studies assume that there is no mortality when predators are absent meaning that the response for no-predators ($M_O$) is simply equal to 1, hence the parameter $M_O$ is implicitly included in the model. The general multiplicative model used for determining interactions between stressors, in which the measurement of the control (none of the factors are present, i.e. $M_O$) can take any value is defined as

$$M_O M_{XY} = M_X M_Y \tag{A.0.3}$$

Once more, this can be written in terms of relative measurements (denoting with the lowercase $m$) with respect to the control by simply dividing both sides by $M_O^2$. Hence, Eq. (A.0.3) becomes

$$\frac{M_{XY}}{M_O} = \frac{M_X}{M_O}\frac{M_Y}{M_O} \tag{A.0.4}$$

or simply $m_{XY} = m_X m_Y$ with the relative response measurements—defined as absolute measurement divided by the control measurement. Indeed, the multiplicative expectation of no-interaction defined by Eq. (A.0.4) is analogous to Bliss Independence (Eq. (1.1.1)) introduced for drug interactions, where the response variable is fitness measurements defined relative to the no-drug case. Note also that a straightforward extension of this multiplicative model to quantify higher-order interactions has been employed in multiple predator studies (that is also analogous to DA metric (Eq. (2.2.2))) and are based on the comparison of experimental value and the predicted value using a 1-way ANOVA [146]. Taking the logarithm of both sides of the preceding relation, Eq. (A.0.4) is equivalent to

$$(\log M_{XY} - \log M_O) = (\log M_X - \log M_O) + (\log M_Y - \log M_O) \tag{A.0.5}$$

suggesting that the multiplicative model for two-way interactions can be tested by merely applying factorial ANOVA on the log-transformed data (see Eq. (A.0.1)). Using the properties of logarithms, we can write the last equation in a more suggestive form as

$$\log m_{XY} = \log m_X m_Y$$

Hence, if the relative measurement of $XY$ combination is equal to the product of the relative measurements when single stressors alone, then we have no interaction. On the contrary, if $m_{XY}$ is significantly different then the expectation from the null model or equivalently, when the deviation from the multiplicative model is significantly non-zero, then ANOVA suggests an interaction between $X$ and $Y$.

Note that following the same logic of additive and multiplicative models, alternative measures to two-way ANOVA (namely Hedge's d and log response ratio (LnRR), respectively) have been proposed to determine interactions based on the deviation from the corresponding model expectation standardized to the effect size [72, 199].

### Three-way ANOVA

In this section, we introduce a translation of three-way ANOVA into a measure within the same framework as above. This way, we also provide a rigorous comparison to our higher-order interaction metrics—DA and E3 that are defined for the characterization of net and emergent interactions(see Chapter 2 and Chapter 3). In the ANOVA framework, three-way interaction is quantified by 2x2x2 factorial design with eight different observations based on the presence and absence of each factor (Fig. A1). Therefore, the observations include no stressors, three stressors alone by themselves ($X$, $Y$, $Z$), all two-way combinations of stressors ($XY$, $XZ$, $YZ$), and all stressors together ($XYZ$). This corresponds to response measurements of $M_O$, $M_X$, $M_Y$, $M_Z$, $M_{XY}$, $M_{XZ}$, $M_{YZ}$, $M_{XYZ}$. In this case, ANOVA determines how two-way interaction between the components $X$ and $Y$ is affected by the addition of a third factor $Z$ [14]. In this case, the third factor ($Z$) is represented by different graphs, and a comparison of the change in the linear effects across these two instances (one with the absence of $Z$, and the other with the presence of $Z$) defines underlying model of three-way ANOVA (Fig. A.1).

From the above discussion and Eq. (A.0.1), the deviation from the no-interaction when $Z$ is not present (denoted by $\text{DEV}_{XY,\text{ no }Z}$) is simply given by

$$\text{DEV}_{XY,\text{ no }Z} = (M_{XY} - M_O) - (M_X - M_O) - (M_Y - M_O) \tag{A.0.6}$$

Likewise, the following expression measures the deviation from the no-interaction case when $Z$ is present

$$\text{DEV}_{XY,\text{ with }Z} = (M_{XYZ} - M_O) - (M_{XZ} - M_O) - (M_{YZ} - M_O) + (M_Z - M_O) \tag{A.0.7}$$

Now, subtracting these two quantities, the difference between these two-way interaction effects becomes

$$\begin{aligned} \text{DEV}_{XY,\text{ no Z}} - \text{DEV}_{XY,\text{ with }Z} = {} & (M_{XYZ} - M_O) - (M_{XY} - M_O) - (M_{XZ} - M_O) - (M_{YZ} - M_O) \\ & + (M_X - M_O) + (M_Y - M_O) + (M_Z - M_O) \end{aligned} \tag{A.0.8}$$

This last relation implies that when $\text{DEV}_{XY,\text{ no }Z} - \text{DEV}_{XY,\text{ with }Z}$ is zero, or equivalently the changes in the slopes across these two graphs are equal, there is no three-way interaction.

On the other hand, if this difference is significantly away from zero, three-way interaction is present. Here, all the derivations are done with respect to the factor $Z$, but one could repeat the same logic with respect to the other factors, and conclude that the same measure as the above expression is symmetric in each factor.

Recalling that the multiplicative model is evaluated by two-way ANOVA on the log-transformed data [151], we now consider applying three-way ANOVA on the log-transformed response measurements. Using properties of logarithm and setting the above equation (Eq. (A.0.8)) to zero—corresponding to the no-interaction case—Eq. (A.0.8) becomes

$$0 = \log m_{XYZ} - \log m_{XY} - \log m_{XZ} - \log m_{YZ} + \log m_X + \log m_Y + \log m_Z$$

Reorganizing this equation by combining each single term with the remaining pairwise combination term (such as $m_X$ with $m_{YZ}$) we get

$$0 = \log m_{XYZ} - log m_{XY} m_Z - \log m_{XZ} m_Y - \log m_{YZ} m_X + 2 \log m_x m_Y m_Z$$

We can draw several conclusions based on the above functional form of three-way ANOVA. First, it is clear that log-transforming the response variable does not help evaluating for the multiplicative model of MPE studies (Eq. (A.0.4)) or equivalently DA measure from the drug interaction studies (Eq. (2.2.2)) for three- or higher-order combinations. Next, three-way ANOVA differs from our emergent three-way measure (Eq. (2.2.4)), but functional form is similar as all the terms in E3 are simply log-transformed. More discussion on three-way ANOVA together with the three-way ANOVA analysis of our bacterial growth data is given in the corresponding online Supplementary Material of Chapter 2.

# APPENDIX B

# Derivation of length asymmetry ratio given branching angles

Here, we relate the length asymmetry ratio ($\lambda_l$) to the optimal branching solutions ($\theta_i$) and the geometry of the unshared endpoints (i.e., the vertices $V_i$). We denote the lengths of the sides of the triangle that correspond to $V_1V_2$, $V_0V_2$, and $V_0V_1$ as $v_0, v_1$, and $v_2$, respectively (Fig. B.1). We first prove two Lemmas that lead to the derivation of the asymmetric length ratio.

**Figure B.1: (a)** Schematic of the branching geometry **(b)** Illustration of degenerate cases where the branching junction coincides with one of the vertices.

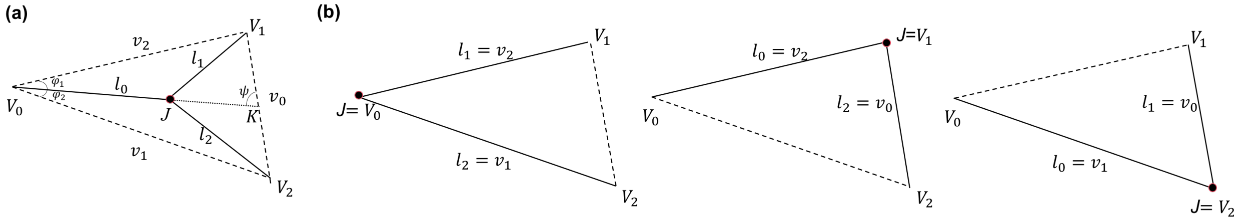

**Lemma B.0.1.** *Let the intersection of the line between the points $V_0$ and $J$ with the line $V_1V_2$ be called $K$ and the angle defined by the three points $\widehat{V_0KV_1}$ be called $\psi$ (Fig. B.1). Using these definitions and the other labeling in Fig. B.1, the following relationships holds*

$$\frac{|V_1K|}{|V_2K|} = \frac{l_1\sin\theta_2}{l_2\sin\theta_1} = \frac{v_2\sin\varphi_1}{v_1\sin\varphi_2}$$

*Proof.* By the law of sines applied to the triangles $V_0V_1K$ and $V_0V_2K$, we have:

$$\frac{\sin\psi}{v_2} = \frac{\sin\varphi_1}{|V_1K|}, \quad \frac{\sin(\pi-\psi)}{\mathrm{v}_1} = \frac{\sin\varphi_2}{|\mathrm{V}_2\mathrm{K}|}$$

Since $\sin(\pi - \psi) = \sin\psi$, dividing these equations yields $\frac{|V_1K|}{|V_2K|} = \frac{v_2 \sin\varphi_1}{v_1 \sin\varphi_2}$. Applying a similar approach to triangles $JV_1K$ and $JV_2K$, we have $\frac{|V_1K|}{|V_2K|} = \frac{l_1 \sin\theta_2}{l_2 \sin\theta_1}$, as desired. □

**Lemma B.0.2.** *The length asymmetry ratio ($\lambda_l = \frac{l_1}{l_2}$) can be calculated purely in terms of the lengths of the sides of $v_1$ and $v_2$ along with the angle $\widehat{V_1V_0V_2}$ and the branching angles $\theta_1$* and *$\theta_2$ as*

$$\lambda_l = \frac{v_2}{v_1}\frac{\sin\theta_1}{\sin\theta_2}\left(-\cos\widehat{V_1V_0V_2} + \sin\widehat{V_1V_0V_2}\,\cot\left(\widehat{V_1V_0V_2} + \gamma - \theta_2\right)\ \right)$$

*where* $\gamma = \cot^{-1}\left[\frac{\frac{v_2}{v_1}\frac{\sin\theta_1}{\sin\theta_2} + \cos\left(\theta_1+\theta_2-\widehat{V_1V_0V_2}\right)}{\sin\left(\theta_1+\theta_2-\widehat{V_1V_0V_2}\right)}\right]$

*Proof.* By Lemma B.0.1, we have

$$\lambda_l = \frac{l_1}{l_2} = \frac{v_2}{v_1}\frac{\sin\theta_1}{\sin\theta_2}\frac{\sin\varphi_1}{\sin\varphi_2}$$

Then, by applying law of sines in a specific, successive order and also using sine addition formulas, we express $\frac{\sin\varphi_1}{\sin\varphi_2}$ in terms of known quantities and branching angles:

$$\frac{\sin\varphi_1}{\sin\varphi_2} = \left(-\cos\widehat{V_1V_0V_2} + \sin\widehat{V_1V_0V_2}\,\cot\left(\widehat{V_1V_0V_2} + \gamma - \theta_2\right)\ \right)$$

proving the lemma. □

With Lemma B.0.2, we show that the branching angle solution—obtained by optimizing certain structural principles—also predicts the optimal value for the asymmetric length ratio.

# APPENDIX C

## Coordinate-free framework for material-cost (MC) optimization solutions

In this section, we introduce a coordinate-free framework for the minimization of the objective function, defined as $H = \sum_i h_i l_i$. We have not seen this approach in the literature, and other references have used methods that rely on specific choices of coordinate systems and complicated algebra [105, 106, 182]. The solution is obtained via finding the stationary and singular points of the cost function $H$ with respect to $l_0$ (the parent vessel length) and $\varphi_1$ (the angle of the parent vessel relative to its unshared endpoint $V_0$) (Fig. B.1). Below, we provide two lemmas that will be used to determine $\frac{\partial H}{\partial l_0}$ and $\frac{\partial H}{\partial \varphi_1}$.

**Lemma C.0.1.** *Given fixed endpoints $V_0$, $V_1$, and $V_2$, the length $|V_0V_1|$ and the angle $\varphi_1$ are fixed in the triangle $V_0JV_1$, (Fig. C.1), the derivative of a daughter vessel length with respect to the parent vessel length is*

$$\frac{\partial l_1}{\partial l_0} = \cos\theta_2$$

*Proof.* Draw a perpendicular line passing through $V_1$ and intersecting with the extension of $V_0J$ at $O$. Denote $|V_0V_1| = v_2$, $|V_1O| = y$, and $|JO| = x$. When $J$ is on the right side of $V_0$, we have $v_2 \cos\varphi\ = x + l_0$. Since $v_2 \cos\varphi_1$ is fixed because $v_2$ and $\varphi_1$ are fixed, it follows that $\partial\left(v_2 \cos\varphi\ \right) = \partial(x + l_0) = 0$, or equivalently

$$\frac{\partial x}{\partial l_0} = -1 \tag{C.0.1}$$

Notice however that the derivative $\frac{\partial x}{\partial l_0}$ is discontinuous when the branching junction collapses on the parent endpoint (i.e., $l_0 = 0$) as the right and left derivatives of $x$ with respect to $l_0$ are opposite in sign: $\partial_+ x\left(0\right) = \frac{\partial\left(v_2 \cos\varphi_1 \ - l_0\ \right)}{\partial l_0} = -1$, $\partial_- x\left(0\right) = \frac{\partial\left(v_2 \cos\varphi_1 \ + l_0\right)}{\partial l_0} = 1$ (Fig. C.1).

Applying the Pythagorean Theorem to the triangle $V_1 J O$, we have $l_1 = \sqrt{x^2 + y^2}$, hence

$$\frac{\partial l_1}{\partial x} = \frac{x}{\sqrt{x^2 + y^2}} = \frac{x}{l_1} \tag{C.0.2}$$

Using the chain rule along with equations (C.0.1) and (C.0.2) gives

$$\frac{\partial l_1}{\partial l_0} = \frac{\partial l_1}{\partial x}\frac{\partial x}{\partial l_0} = -\frac{\partial l_1}{\partial x} = -\frac{x}{l_1} = -\cos\left(\pi - \theta_2\right) \ = \cos\theta_2$$

as desired. ☐

**Figure C.1: (a)** The branching geometry of a parent and one of the daughter vessels. **(b)** When the vertex $J$ approaches the vertex $V_0$ from the right, $x = v_2 cos\varphi_1 \ - l_0$. **(c)** When the vertex $J$ approaches the vertex $\mathrm{V}_0$ from the right, $x = v_2 cos\varphi_1 \ + l_0$.

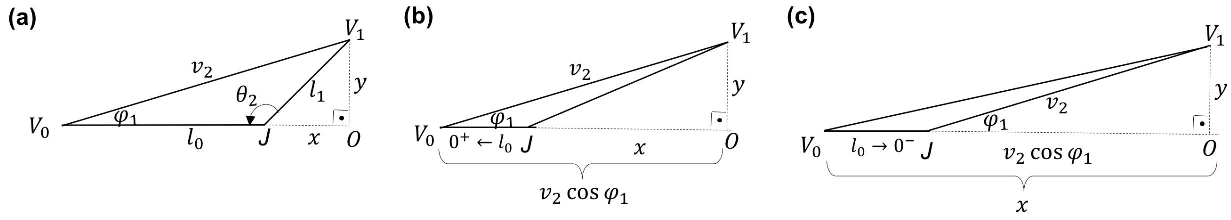

**Lemma C.0.2.** *Given fixed lengths* $|V_0 V_1| = v_2$ *and* $l_0$ *in the triangle* $V_0 J V_1$*, then*

$$\frac{\partial l_1}{\partial \varphi_1} = -l_0 \sin\theta_2$$

*Proof.* As in Lemma B.0.1, we have $\cos\theta_2 \ = -\cos\left(\pi - \theta_2\right) = -\frac{\mathrm{x}}{\mathrm{l}_1}$ and $\mathrm{l}_1 = \sqrt{\mathrm{x}^2 + \mathrm{y}^2}$. From the triangle $V_0 V_1 O$, we further have $y = v_2 \sin\varphi_1$ and $x = v_2 \cos\varphi_1 \ - l_0$. Substituting these into the expression for $l_1$ yields $l_1 = \sqrt{\left(v_2 \cos\varphi_1 \ - l_0\right)^2 + \left(v_2 \sin\varphi_1 \ \right)^2}$. As $v_2$ and $l_0$ are fixed, differentiating $l_1$ with respect to $\varphi_1$ gives:

$$\frac{\partial l_1}{\partial \varphi_1} = \frac{1}{2}\frac{2\left(v_2 \cos\varphi_1 \ - l_0\right)\left(-v_2 \sin\varphi_1 \ \right) + 2 v_2^2 \sin\varphi_1 \cos\varphi_1}{\sqrt{\left(v_2 \cos\varphi_1 \ - l_0\right)^2 + \left(v_2 \sin\varphi_1 \ \right)^2}}$$

This expression simplifies by cancelling the $2v_2^2 \sin\varphi_1 \cos\varphi_1$ terms in the numerator and by recognizing the denominator is equal to $l_1$. Therefore, we obtain $\frac{\partial l_1}{\partial \varphi_1} = \frac{l_0 v_2}{l_1} \sin\varphi_1$ . Since $\sin\varphi_1 = \frac{y}{v_2}$ and $\sin(\pi - \theta_2) = \frac{y}{l_1}$, this equation becomes

$$\frac{\partial l_1}{\partial \varphi_1} = \frac{l_0 v_2}{l_1} \sin\varphi = l_0 \frac{y}{l_1} = -l_0 \sin\theta_2$$

□

With these two lemmas proven, we now return to the original optimization problem. Unless $J$ coincides with the unshared endpoints $V_0, V_1$ or $V_2$, substituting Lemma 1 and Lemma 2 into the equality, we have

$$\nabla H = \left( \frac{\partial H}{\partial l_0}, \frac{\partial H}{\partial \varphi_1} \right) = \overrightarrow{0},$$

leads to two equations

$$h_0 = -h_1 \cos\theta_2 - h_2 \cos\theta_1 \tag{C.0.3}$$

$$h_1 sin\theta_2 = h_2 sin\theta_1 \tag{C.0.4}$$

Solving these equations yields the previously reported branching angle solutions (Eq. (1) in our paper and from Zamir et. al. (1, 2)).

Dividing both sides of the equations (C.0.3) and (C.0.4) by $h_2$ and combining them, we have

$$\frac{h_0}{h_2} = -\frac{\sin\theta_1 cos\theta_2 + \sin\theta_2 cos\theta_1}{\sin\theta_2} = \frac{-\sin(\theta_1 + \theta_2)}{\sin\theta_2}$$

Realizing that $\theta_1 + \theta_2 = 2\pi - \theta_0$, or equivalently $-\sin(\theta_1 + \theta_2) = \sin\theta_0$ , and combining the above equations (C.0.3) and (C.0.4) yields $h_0 sin\theta_2 = h_2 sin\theta_0$. Thus, in order for the equations that follow from $\nabla H = \overrightarrow{0}$ to be soluble, the expressions $\sin\theta_0$ , $\sin\theta_1$, and $\sin\theta_2$ must all have the same sign because the length scales $h_i$ are all positive. This sign criterion can only be satisfied when the branching junction is inside of the triangle defined by $V_0$, $V_1$ and $V_2$. Consequently, this implies $\nabla H = \overrightarrow{0}$ cannot be satisfied when the branching junction is outside of the triangle or on the boundary of the triangle. Therefore, in order for the previously reported formula for the branching-angle solutions to be valid, we need to check first if $-1 \leq \cos\theta_i \ \leq 1$, and if it does not, we must conclude that $\nabla H = \overrightarrow{0}$ does not have a solution. Previous studies were not explicit about this criterion or distinction in finding solutions. Solving the inequalities $-1 \leq \cos\theta_i \ \leq 1$ for each branching angle yields necessary conditions for the existence of solutions of $\nabla H = \overrightarrow{0}$. These conditions reduce to the simple statement, $h_i < h_j + h_k$, about the weightings of the terms in the cost function for any combination of $(i,\ j,\ k)$. If any of these three conditions fail, then the branching junction will be degenerate, meaning that the optimal branching junction, $J$, will collapse to one of the vertices.

Moreover, the angles of the triangle $V_0V_1V_2$ further confine the range of branching angles that can be realized within the triangle, i.e. $\widehat{V_jV_iV_k} < \theta_i$. Hence, if branching angle solutions defined by Eq. (4.2.1) violate any of these conditions, the optimization solution will be a collapse of the branching junction onto one of the unshared endpoints.

# APPENDIX D

# Degeneracy solutions of material-cost (MC) optimization

We now derive which particular vertex the branching junction will collapse onto for the degeneracy cases.

**Lemma D.0.1.** *When the triangle conditions and inequalities do not hold (i.e.,* $h_i \geq h_j + h_k$*), the vertex* $V_i$ *associated with the largest cost parameter (i.e.,* $h_i$*) is the solution for the material cost optimization.*

*Proof.* By symmetry and without loss of generality, we assume that the cost per parent length is greater than the sum of the costs per length for the daughter vessels, i.e. $h_0 \geq h_1 + h_2$. To identify the vertex that yields the minimum cost, we will calculate the total cost corresponding to all three degenerate cases (Fig. B.1). Total costs at the corresponding vertices are given by $H_{V_0} = h_1 v_2 + h_2 v_1,\ H_{V_1} = h_0 v_2 + h_2 v_0$, and $H_{V_2} = h_0 v_1 + h_1 v_0$, where $v_0$, $v_1$, and $v_2$ are lengths of sides $V_1V_2,\ V_0V_2,\ V_0V_1$ respectively. From our assumption and triangle inequality applied to the sides of the triangle $V_0V_1V_2$, we have $H_{V_1} = h_0 v_2 + h_2 v_0 \geq (h_1 + h_2) v_2 + h_2 v_0 = h_2 (v_0 + v_2) + h_1 v_2 > h_2 v_1 + h_1 v_2 = H_{V_0}$. In a symmetric way, one can also prove that $H_{V_2} > H_{V_1}$, implying that $J$ collapses on $V_0$. □

**Lemma D.0.2.** *For any triangle with vertices X, Y, Z, and a point P inside this triangle we have the following inequality*

$$|XY| + |YZ| > |XP| + |PZ|$$

*Proof.* The set of points Y' on the plane for which

$$|XY'| + |Y'Z| = |XY| + |YZ|$$

forms an ellipse as illustrated in Fig. D.1. Therefore, for any point $P'$ in the interior of the ellipse

$$|XP'| + |P'Z| < |XY| + |YZ|$$

proving the claim. □

**Figure D.1:** Ellipse formed by the points $X$, $Y$, and $Z$. By definition, the sum of the distances from any point on the ellipse to $X$ and $Z$ is fixed.

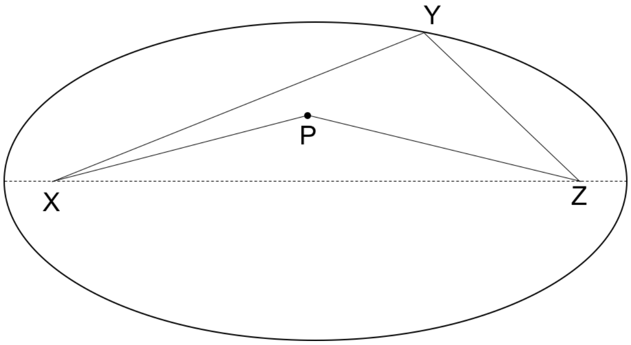

**Lemma D.0.3.** *When optimal branching angle solutions (Eq. 4.2.1) result in a case where the triangle condition ($\widehat{V_jV_iV_k} \geq \theta_i$) fails, then the vertex associated with $\theta_i$ for which the inequality fails also provides the minimum of $H$.*

*Proof.* Without loss of generality, let us assume that the optimal solution of $\theta_0$ is less than the angle $\widehat{V_1V_0V_2}$. As ${h_0}^2 = {h_1}^2 + {h_2}^2 - 2h_1h_2\cos(\pi - \theta_0)$ , we can form a triangle OAB with side-lengths $h_0, h_1, h_2$ that has the angle $\pi - \theta_0$ at the vertex A (Fig. D.2). Now, let us construct a triangle ABC similar to the triangle $V_0V_1V_2$. Drawing a line segment AC of length $h_2\frac{v_1}{v_2}$ , so that the angle $\widehat{CAB}$ equals $\widehat{V_0} := \widehat{V_2V_0V_1}$, yields such a triangle with similarity ratio $\frac{h_2}{v_2}$. Hence, the side BC has length $h_2\frac{v_0}{v_2}$ (Fig. D.2). Then, the side inequality applied to the concave quadrilateral OBCA (Lemma 6) leads to $h_0 + h_2\frac{v_0}{v_2} > h_1 + h_2\frac{v_1}{v_2}$. Multiplying both sides by $v_2$ provides $H_{V_1} = h_0v_2 + h_2v_0 > h_2v_1 + h_1v_2 = H_{V_0}$. In a similar manner, we can show that $H_{V_2} > H_{V_0}$, demonstrating that $V_0$ gives the optimal position for $J$. By symmetry, when $\theta_1 < \widehat{V_0V_1V_2}$ this implies the branching junction $J$ collapses to $V_1$, and when $\theta_2 < \widehat{V_1V_2V_0}$, this implies that $J$ collapses to $V_2$. □

**Figure D.2:** The diagram of the proof to show showing that when $\theta < \widehat{V_0}$, the branching junction J will collapse on $V_0$

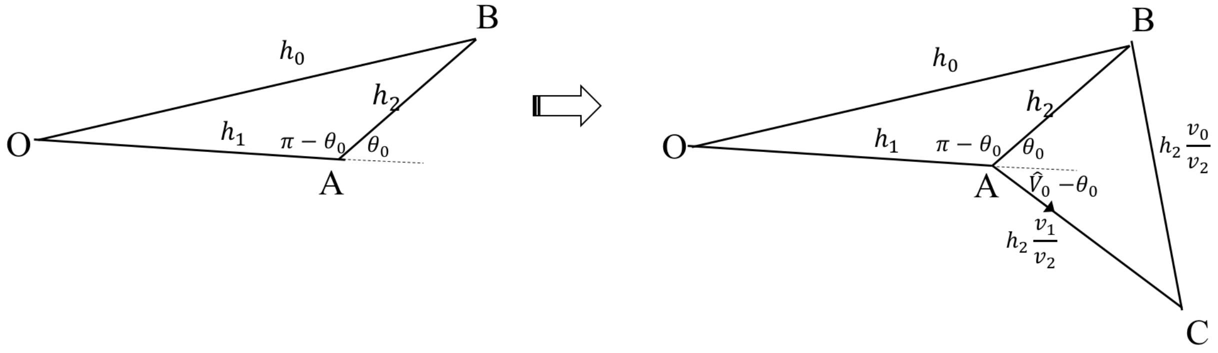

# APPENDIX E

# Power-cost optimization for a single branching junction (PC-0) solutions

Here, we show that power cost optimization always leads to degenerate branching geometry. To do this, we first calculate the equivalent impedances when the branching junction $J$ occurs at the vertex $V_i$ (Fig. B.1)—denoted by $Z_{V_i}$—for each $i$ .

$$Z_{V_0} = \left(\frac{1}{h_1 v_2} + \frac{1}{h_2 v_1}\right)^{-1}, \quad Z_{V_1} = h_0 v_2 \ , \quad Z_{V_2} = h_0 v_1$$

Now, if we show that $Z_{eq} \geq \min\left(Z_{V_0}, Z_{V_1}, Z_{V_2}\right)$ , it follows that $Z_{eq}$ attains its minimum at one of the vertices. Without loss of generality, we assume that $v_1 \leq v_2$, so $Z_{V_2} \leq Z_{V_1}$ and $\min\left(Z_{V_0}, Z_{V_1}, Z_{V_2}\right) = \min\left(Z_{V_0}, Z_{V_2}\right)$. The following lemmas verify our claim that one of the vertices is always optimal for the branching junction.

**Lemma E.0.1.** *Let $Z_{V_0} < Z_{V_2}$. Then,* $\min\left(Z_{eq}\right) = Z_{V_0}$

*Proof.* To prove the lemma, we need to show that $Z_{eq} \geq Z_{V_0}$ for all possible locations of the branching junction, $J$. Because $Z_{V_0} < Z_{V_2}$, we have $h_0 > \frac{1}{v_1}\left(\frac{1}{h_1 v_2} + \frac{1}{h_2 v_1}\right)^{-1}$, so we can form the following inequality by replacing $h_0$ by $\left(\frac{1}{h_1 v_2} + \frac{1}{h_2 v_1}\right)^{-1} \frac{1}{v_1}$ $Z_{eq} = h_0 l_0 + \left(\frac{1}{h_1 l_1} + \frac{1}{h_2 l_2}\right)^{-1} > \left(\frac{1}{h_1 v_2} + \frac{1}{h_2 v_1}\right)^{-1} \frac{l_0}{v_1} + \left(\frac{1}{h_1 l_1} + \frac{1}{h_2 l_2}\right)^{-1}$

To prove $Z_{eq} \geq Z_{V_0} = \left(\frac{1}{h_1 v_2} + \frac{1}{h_2 v_1}\right)^{-1}$, it suffices to prove

$$\left(\frac{1}{h_1 v_2} + \frac{1}{h_2 v_1}\right)^{-1} \frac{l_0}{v_1} + \left(\frac{1}{h_1 l_1} + \frac{1}{h_2 l_2}\right)^{-1} \geq \left(\frac{1}{h_1 v_2} + \frac{1}{h_2 v_1}\right)^{-1}$$

Rearranging terms, the proof of the Lemma boils down to proving the inequality

$$\left(\frac{1}{h_1 l_1}+\frac{1}{h_2 l_2}\right)^{-1}>\left(1-\frac{l_0}{v_1}\right)\left(\frac{1}{h_1 v_2}+\frac{1}{h_2 v_1}\right)^{-1} \tag{E.0.1}$$

Taking the reciprocal of both sides of (E.0.1) and factoring out the terms with $\frac{1}{h_1}$ and $\frac{1}{h_2}$, this inequality is equivalent to

$$\frac{1}{h_1}\left(\frac{1}{l_1}-\frac{1}{v_2}\left(1-\frac{l_0}{v_1}\right)^{-1}\right)+\frac{1}{h_2}\left(\frac{1}{l_2}-\frac{1}{v_1}\left(1-\frac{l_0}{v_1}\right)^{-1}\right)<0$$

Hence, if we show that both of the terms in the above expression are negative, then their sum would also be negative, and the proof will be complete. In other words, it suffices to show two inequalities

$$\frac{1}{l_1}-\frac{1}{v_2}\left(1-\frac{l_0}{v_1}\right)^{-1}<0 \tag{E.0.2}$$

$$\frac{1}{l_2}-\frac{1}{v_1}\left(1-\frac{l_0}{v_1}\right)^{-1}<0 \tag{E.0.3}$$

Observe that the triangle inequality applied to the triangle $V_0JV_1$ gives $l_0+l_1>v_2$, hence $\frac{l_1}{v_2}>1-\frac{l_0}{v_2}>1-\frac{l_0}{v_1}$, proving (E.0.2). Moreover, the triangle inequality applied to the triangle $V_0JV_2$ yields $l_0+l_2>v_1$, implying that $\frac{l_2}{v_1}>1-\frac{l_0}{v_1}$, which proves (E.0.3). □

The next lemma takes care of the complementary case.

**Lemma E.0.2.** *Let* $Z_{V_0}>Z_{V_2}$*, then* $\min Z_{eq}=Z_{V_2}$

*Proof.* Following the same idea as in the proof of Lemma E.0.1, we want to show that $Z_{eq}\geq Z_{V_2}$, or equivalently

$$\left(\frac{1}{h_1 l_1}+\frac{1}{h_2 l_2}\right)^{-1}>h_0(v_1-l_0)$$

By the inequality (E.0.1), we proved in Lemma E.0.1, we have

$$\left(\frac{1}{h_1 l_1}+\frac{1}{h_2 l_2}\right)^{-1}>\left(1-\frac{l_0}{v_1}\right)\left(\frac{1}{h_1 c}+\frac{1}{h_2 v_1}\right)^{-1}$$

The assumption $\left(\frac{1}{h_1 v_2} + \frac{1}{h_2 v_1}\right)^{-1} > h_0 v_1$ further yields that

$$\left(\frac{1}{h_1 l_1} + \frac{1}{h_2 l_2}\right)^{-1} > \left(1 - \frac{l_0}{v_1}\right) h_0 v_1 = h_0(v_1 - l_0)$$

as desired. $\square$

With Lemmas E.0.1 and E.0.2, we proved that the branching junction collapses onto one of the vertices for any choice of cost parameters $h_0$, $h_1$, and $h_2$.

# APPENDIX F

# Enlarged consideration of the power-cost optimization to go beyond a single branching (PC-1)

In this section, we add terms $c_1$ and $c_2$ to the calculation of $\tilde{Z}_{eq}$ to respectively represent the impedance of all of the vessels are downstream from each daughter vessel at that branching junction. Furthermore, we consider the special case that impedance matching—the impedance of the parent vessel is matched by the equivalent impedances of the daughter vessels—is satisfied throughout the whole network. By requiring that siblings have identical impedances and that each sibling has the same number of downstream vessels, we show that the ratio $\frac{c_i}{Z_i}$ is larger for vessels that are near to the first branching level (i.e., the heart). To simplify the calculations, we enumerate the levels such that the level number increases from capillary (level 0) to the heart (level $N$). This is the reverse of the labeling used in most models.

By applying impedance matching successively from level 0 to level $k$, we first recognize that the impedance of the vessel at the $k^{th}$ level is given by $Z_0/2^k$, where $Z_0$ denotes the impedance of the capillary. Moreover, for the first few levels above the capillary level (when $k = 0,\ 1,\ 2$), we find that the downstream impedance at level $k$ follows the form $\frac{kZ}{2^k}$ (Fig. F.1). The next Lemma generalizes this formula for all levels $k$.

**Figure F.1:** **(a)** Perfectly-balanced branching network with identical daughter impedances and **(b)** inclusion of impedances for downstream vessels in entire branching network and thus beyond just the branching level $k$.

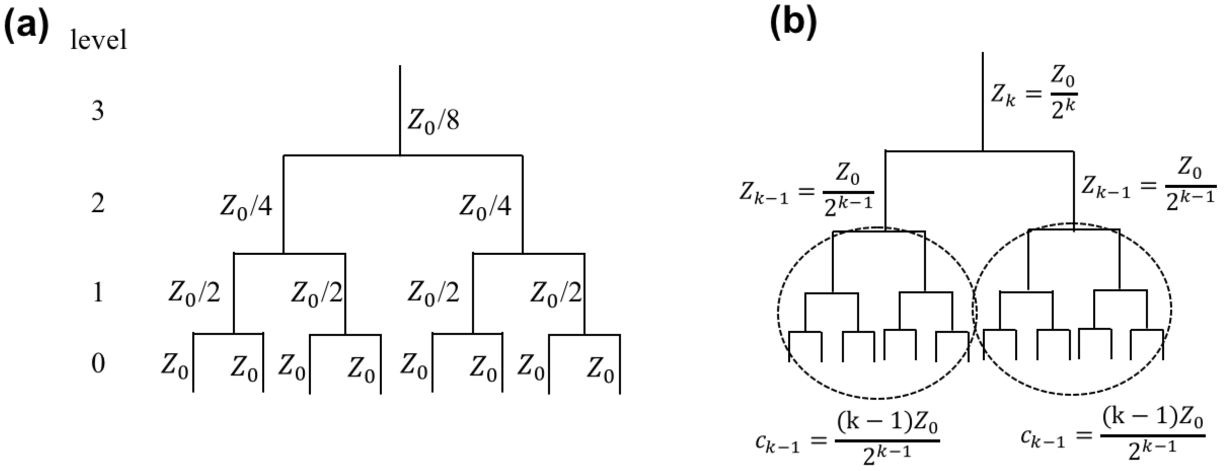

**Lemma F.0.1.** *The downstream impedance from a daughter vessel at level $k$ is given by*

$$c_k = \frac{kZ_0}{2^k}$$

*Proof.* We prove this claim by induction. Note that a vessel at level $k-1$ is in series with the downstream vessels as illustrated in the Fig. F.1. If the downstream impedance at level $(k-1)$ is equal to $\frac{(k-1)Z}{2^{k-1}}$, then by rules of fluid mechanics, the downstream impedance at level $k$ is given by

$$c_k = \frac{1}{\frac{1}{\frac{Z_0}{2^{k-1}}+\frac{(k-1)Z_0}{2^{k-1}}} + \frac{1}{\frac{Z_0}{2^{k-1}}+\frac{(k-1)Z_0}{2^{k-1}}}} = \frac{kZ_0}{2^k}.$$

□

Hence, by Lemma F.0.1, we have that the value of $c_k/Z_k$ at level $k$ is equal to

$$\frac{\frac{kZ_0}{2^k}}{\frac{Z_0}{2^k}} = k$$

so that the value of this ratio increases with the level (i.e., increase from the capillaries to the heart). Therefore, near the heart, the constants ($c_i$) representing the downstream impedances in the optimization scheme are relatively large compared to the impedances ($Z_i$)

of the daughter vessels at that branching junction.

# References

[1] Madhavi K Ganapathiraju, Mohamed Thahir, Adam Handen, Saumendra N Sarkar, Robert A Sweet, Vishwajit L Nimgaonkar, Christine E Loscher, Eileen M Bauer, and Srilakshmi Chaparala. Schizophrenia interactome with 504 novel proteinprotein interactions. *npj Schizophrenia*, 2:16012, 2016.

[2] S. Pawar, A.I. Dell, and V.M. Savage. Dimensionality of consumer search space drives trophic interaction strengths. *Nature*, 486(7404):485–489, 2012.

[3] P Yeh, AI Tschumi, and R Kishony. Functional classification of drugs by properties of their pairwise interactions. *Nature Genetics*, 38(4):489–494, 2006.

[4] Zhuo Wang, Larry Millet, Mustafa Mir, Huafeng Ding, Sakulsuk Unarunotai, John Rogers, Martha U Gillette, and Gabriel Popescu. Spatial light interference microscopy (slim). *Optics express*, 19(2):1016–1026, 2011.

[5] Mitchell G Newberry, Daniel B Ennis, and Van M Savage. Testing foundations of biological scaling theory using automated measurements of vascular networks. *PLoS Comput Biol*, 11(8):e1004455, 2015.

[6] Elif Tekin, David Hunt, Mitchell G Newberry, and Van M Savage. Do vascular networks branch optimally or randomly across spatial scales? *PLoS computational biology*, 12(11):e1005223, 2016.

[7] Fei Xiao and James D McCalley. Power system risk assessment and control in a multiobjective framework. *IEEE Transactions on Power Systems*, 24(1):78–85, 2009.

[8] Remy Chait, Allison Craney, and Roy Kishony. Antibiotic interactions that select against resistance. *Nature*, 446(7136):668–671, 2007.

[9] Axel Marius Hemmingsen. Energy metabolism as related to body size and respiratory surfaces, and its evolution. *Reports of the Steno Memorial Hospital and Nordisk Insulin Laboratorium*, 9:1–110, 1960.

[10] T. Kolokotrones, E. J. Deeds, V. M. Savage, and W. Fontana. Curvature in metabolic scaling. *Nature*, 464(7289):753756, 2010.

[11] V. M. Savage, E. J. Deeds, and W. Fontana. Sizing up allometric scaling theory. *PLoS Comp. Biol.*, 4(9):e1000171, 2008.

[12] R. S. Etienne, M. E. F. Apol, and H. Olff. Demystifying the west, brown, & enquist model of the allometry of metabolism. *Functional Ecology*, 20:394–399, 2006.

[13] Kevin Wood, Satoshi Nishida, Eduardo D Sontag, and Philippe Cluzel. Mechanism-independent method for predicting response to multidrug combinations in bacteria. *Proceedings of the National Academy of Sciences*, 109(30):12254–12259, 2012.

[14] Barry H Cohen. *Explaining psychological statistics.* John Wiley & Sons, 2008.

[15] Mark EJ Newman. The structure and function of complex networks. *SIAM review*, 45(2):167–256, 2003.

[16] D Segre, A DeLuna, GM Church, and R Kishony. Modular epistasis in yeast metabolism. *Nature Genetics*, 37(1):77–83, 2005.

[17] D. L. Turcotte, J. D. Pelletier, and W. I. Newman. Networks with side branching in biology. *J. Theor. Biol.*, 193(4):577–592, 1998.

[18] Albert-Lszl Barabsi and Rka Albert. Emergence of scaling in random networks. *science*, 286(5439):509–512, 1999.

[19] Paul Erdos and Alfrd Rnyi. On the evolution of random graphs. *Publ. Math. Inst. Hung. Acad. Sci*, 5(1):17–60, 1960.

[20] Bla Bollobs. Random graphs. In *Modern Graph Theory*, pages 215–252. Springer, 1998.

[21] Howard T Odum. Self-organization, transformity, and information. *Science*, 242(4882):1132, 1988.

[22] Gary A. Polis and Donald R. Strong. Food web complexity and community dynamics. *The American Naturalist*, 147(5):813–846, 1996.

[23] Robert T Paine. Food webs: linkage, interaction strength and community infrastructure. *Journal of animal ecology*, 49(3):667–685, 1980.

[24] Reuven Cohen, Keren Erez, Daniel Ben-Avraham, and Shlomo Havlin. Resilience of the internet to random breakdowns. *Physical review letters*, 85(21):4626, 2000.

[25] E. Katifori, G. J. Szollosi, and M. O. Magnasco. Damage and fluctuations induce loops in optimal transport networks. *Physical Review Letters*, 104:048704, 2010.

[26] Casey Beppler, Elif Tekin, Zhiyuan Mao, Cynthia White, Cassandra McDiarmid, Emily Vargas, Jeffrey H Miller, Van M Savage, and Pamela J Yeh. Uncovering emergent interactions in three-way combinations of stressors. *Journal of The Royal Society Interface*, 13(125):20160800, 2016.

[27] Elif Tekin, Casey Beppler, Cynthia White, Zhiyuan Mao, Van M Savage, and Pamela J Yeh. Enhanced identification of synergistic and antagonistic emergent interactions among three or more drugs. *Journal of The Royal Society Interface*, 13(119):20160332, 2016.

[28] C. I. Bliss. The toxicity of poisons applied jointly. *Annals of applied biology*, 26(3):585–615, 01 1939.

[29] S Loewe. The problem of synergism and antagonism of combined drugs. *Arzneimittelforschung*, 3(6):285–290, 1953.

[30] Andrew Sih, Goran Englund, and David Wooster. Emergent impacts of multiple predators on prey. *Trends in Ecology & Evolution*, 13(9):350–355, 1998.

[31] Anna I Podgornaia and Michael T Laub. Pervasive degeneracy and epistasis in a protein-protein interface. *Science*, 347(6222):673–677, 2015.

[32] Takayuki Ohgushi, Oswald Schmitz, and Robert D Holt. *Trait-mediated indirect interactions: ecological and evolutionary perspectives.* Cambridge University Press, 2012.

[33] Mirta Galesic, Astrid Kause, and Wolfgang Gaissmaier. A sampling framework for uncertainty in individual environmental decisions. *Topics in cognitive science*, 8(1):242–258, 2016.

[34] Daniel M Weinreich and Jennifer L Knies. Fisher's geometric model of adaptation meets the functional synthesis: data on pairwise epistasis for fitness yields insights into the shape and size of phenotype space. *Evolution*, 67(10):2957–2972, 2013.

[35] Daniel Barrios-O'Neill, Jaimie TA Dick, Mark C Emmerson, Anthony Ricciardi, Hugh J MacIsaac, Mhairi E Alexander, and Helene C Bovy. Fortune favours the bold: a higher predator reduces the impact of a native but not an invasive intermediate predator. *Journal of Animal Ecology*, 83(3):693–701, 2014.

[36] Tobias Bollenbach, Selwyn Quan, Remy Chait, and Roy Kishony. Nonoptimal microbial response to antibiotics underlies suppressive drug interactions. *Cell*, 139(4):707–718, 2009.

[37] PJ Yeh, MJ Hegreness, AP Aiden, and R Kishony. Drug interactions and the evolution of antibiotic resistance. *Nature Reviews Microbiology*, 7(6):460–466, 2009.

[38] Matthew Hegreness, Noam Shoresh, Doris Damian, Daniel Hartl, and Roy Kishony. Accelerated evolution of resistance in multidrug environments. *Proceedings of the National Academy of Sciences*, 105(37):13977–13981, 2008.

[39] Mark P. Brynildsen, Jonathan A. Winkler, Catherine S. Spina, I. Cody MacDonald, and James J. Collins. Potentiating antibacterial activity by predictably enhancing endogenous microbial ros production. *Nature Biotechnology*, 31(2):160–165, 2013.

[40] Veronica L. Cavera, Anna Volski, and Michael L. Chikindas. The natural antimicrobial subtilosin a synergizes with lauramide arginine ethyl ester (lae), -poly-l-lysine (polylysine), clindamycin phosphate and metronidazole, against the vaginal pathogen gardnerella vaginalis. *Probiotics and Antimicrobial Proteins*, 7(2):164–171, 2015.

[41] Benjamin M. Geilich, Anne L. van de Ven, Gloria L. Singleton, Liuda J. Sepulveda, Srinivas Sridhar, and Thomas J. Webster. Silver nanoparticle-embedded polymersome nanocarriers for the treatment of antibiotic-resistant infections. *Nanoscale*, 7(8):3511–3519, 2015.

[42] Shankar Thangamani, Waleed Younis, and Mohamed N Seleem. Repurposing clinical molecule ebselen to combat drug resistant pathogens. *PloS one*, 10(7):e0133877, 2015.

[43] Theodouli Stergiopoulou, Joseph Meletiadis, Tin Sein, Paraskevi Papaioannidou, Thomas J Walsh, and Emmanuel Roilides. Synergistic interaction of the triple combination of amphotericin b, ciprofloxacin, and polymorphonuclear neutrophils against aspergillus fumigatus. *Antimicrobial agents and chemotherapy*, 55(12):5923–5929, 2011.

[44] Joseph Meletiadis, Vidmantas Petraitis, Ruta Petraitiene, Pengxin Lin, Theodouli Stergiopoulou, Amy M Kelaher, Tin Sein, Robert L Schaufele, John Bacher, and Thomas J Walsh. Triazole-polyene antagonism in experimental invasive pulmonary aspergillosis: in vitro and in vivo correlation. *Journal of Infectious Diseases*, 194(7):1008–1018, 2006.

[45] Alexander J Lepak and David R Andes. Antifungal pk/pd considerations in fungal pulmonary infections. In *Seminars in respiratory and critical care medicine*, volume 32, pages 783–794. Thieme Medical Publishers, 2011.

[46] Vidmantas Petraitis, Ruta Petraitiene, William W Hope, Joseph Meletiadis, Diana Mickiene, Johanna E Hughes, Margaret P Cotton, Theodouli Stergiopoulou, Miki Kasai, and Andrea Francesconi. Combination therapy in treatment of experimental pulmonary aspergillosis: in vitro and in vivo correlations of the concentration-and dose-dependent interactions between anidulafungin and voriconazole by bliss independence drug interaction analysis. *Antimicrobial agents and chemotherapy*, 53(6):2382–2391, 2009.

[47] Na Guo, Jingbo Liu, Xiuping Wu, Xingming Bi, Rizeng Meng, Xuelin Wang, Hua Xiang, Xuming Deng, and Lu Yu. Antifungal activity of thymol against clinical isolates of fluconazole-sensitive and-resistant candida albicans. *Journal of medical microbiology*, 58(8):1074–1079, 2009.

[48] Wenna Shi, Zuozhong Chen, Xu Chen, Lili Cao, Ping Liu, and Shujuan Sun. The combination of minocycline and fluconazole causes synergistic growth inhibition against candida albicans: an in vitro interaction of antifungal and antibacterial agents. *FEMS yeast research*, 10(7):885–893, 2010.

[49] William D Bradley, Shilpi Arora, Jennifer Busby, Srividya Balasubramanian, Victor S Gehling, Christopher G Nasveschuk, Rishi G Vaswani, Chih-Chi Yuan, Charlie Hatton, and Feng Zhao. Ezh2 inhibitor efficacy in non-hodgkins lymphoma does not require suppression of h3k27 monomethylation. *Chemistry & biology*, 21(11):1463–1475, 2014.

[50] Sigrid Nachtergaele, Laurel K Mydock, Kathiresan Krishnan, Jayan Rammohan, Paul H Schlesinger, Douglas F Covey, and Rajat Rohatgi. Oxysterols are allosteric activators of the oncoprotein smoothened. *Nature chemical biology*, 8(2):211–220, 2012.

[51] Donavon C Hiss, Gary A Gabriels, and Peter I Folb. Combination of tunicamycin with anticancer drugs synergistically enhances their toxicity in multidrug-resistant human ovarian cystadenocarcinoma cells. *Cancer cell international*, 7(1):1, 2007.

[52] Jeffrey J. Wallin, Jane Guan, Wei Wei Prior, Leslie B. Lee, Leanne Berry, Lisa D. Belmont, Hartmut Koeppen, Marcia Belvin, Lori S. Friedman, and Deepak Sampath.

Gdc-0941, a novel class i selective pi3k inhibitor, enhances the efficacy of docetaxel in human breast cancer models by increasing cell death ¡em¿in vitro¡/em¿ and ¡em¿in vivo¡/em¿. *Clinical Cancer Research*, 18(14):3901–3911, 2012.

[53] Raffaella Soldi, Adam Louis Cohen, Luis Cheng, Ying Sun, PJ Moos, and Andrea H Bild. A genomic approach to predict synergistic combinations for breast cancer treatment. *The pharmacogenomics journal*, 13(1):94–104, 2013.

[54] M Axelrod, Z Ou, LK Brett, L Zhang, ER Lopez, AT Tamayo, V Gordon, RJ Ford, ME Williams, and LV Pham. Combinatorial drug screening identifies synergistic co-targeting of bruton's tyrosine kinase and the proteasome in mantle cell lymphoma. *Leukemia*, 28(2):407, 2014.

[55] Gregory M Laird, C Korin Bullen, Daniel IS Rosenbloom, Alyssa R Martin, Alison L Hill, Christine M Durand, Janet D Siliciano, and Robert F Siliciano. Ex vivo analysis identifies effective hiv-1 latencyreversing drug combinations. *The Journal of clinical investigation*, 125(5):1901–1912, 2015.

[56] Benjamin L Jilek, Melissa Zarr, Maame E Sampah, S Alireza Rabi, Cynthia K Bullen, Jun Lai, Lin Shen, and Robert F Siliciano. A quantitative basis for antiretroviral therapy for hiv-1 infection. *Nature medicine*, 18(3):446–451, 2012.

[57] Xu Tan, Long Hu, Lovelace J Luquette III, Geng Gao, Yifang Liu, Hongjing Qu, Ruibin Xi, Zhi John Lu, Peter J Park, and Stephen J Elledge. Systematic identification of synergistic drug pairs targeting hiv. *Nature biotechnology*, 30(11):1125–1130, 2012.

[58] Guochun Jiang, Erica A Mendes, Philipp Kaiser, Daniel P Wong, Yuyang Tang, Ivy Cai, Anne Fenton, Gregory P Melcher, James EK Hildreth, and George R Thompson. Synergistic reactivation of latent hiv expression by ingenol-3-angelate, pep005, targeted nf-kb signaling in combination with jq1 induced p-tefb activation. *PLoS Pathog*, 11(7):e1005066, 2015.

[59] Tomoko Kobayashi, Yoshiki Koizumi, Junko S Takeuchi, Naoko Misawa, Yuichi Kimura, Satoru Morita, Kazuyuki Aihara, Yoshio Koyanagi, Shingo Iwami, and Kei Sato. Quantification of deaminase activity-dependent and-independent restriction of hiv-1 replication mediated by apobec3f and apobec3g through experimental-mathematical investigation. *Journal of virology*, 88(10):5881–5887, 2014.

[60] X-M Xu, Peter Jeffries, M Pautasso, and Michael J Jeger. Combined use of biocontrol agents to manage plant diseases in theory and practice. *Phytopathology*, 101(9):1024–1031, 2011.

[61] LK Otto-Hanson, Z Grabau, C Rosen, CE Salomon, and LL Kinkel. Pathogen variation and urea influence selection and success of streptomyces mixtures in biological control. *Phytopathology*, 103(1):34–42, 2013.

[62] Rafael Sanjun and Santiago F Elena. Epistasis correlates to genomic complexity. *Proceedings of the National Academy of Sciences*, 103(39):14402–14405, 2006.

[63] Jason H Moore. A global view of epistasis. *Nature genetics*, 37(1):13–14, 2005.

[64] Alexander DeLuna, Kalin Vetsigian, Noam Shoresh, Matthew Hegreness, Maritrini Coln-Gonzlez, Sharon Chao, and Roy Kishony. Exposing the fitness contribution of duplicated genes. *Nature genetics*, 40(5):676–681, 2008.

[65] Xionglei He, Wenfeng Qian, Zhi Wang, Ying Li, and Jianzhi Zhang. Prevalent positive epistasis in escherichia coli and saccharomyces cerevisiae metabolic networks. *Nature genetics*, 42(3):272–276, 2010.

[66] Lukasz Jasnos and Ryszard Korona. Epistatic buffering of fitness loss in yeast double deletion strains. *Nature genetics*, 39(4):550–554, 2007.

[67] S. M. Hammer, D. A. Katzenstein, M. D. Hughes, H. Gundacker, R. T. Schooley, R. H. Haubrich, W. K. Henry, M. M. Lederman, J. P. Phair, M. Niu, M. S. Hirsch, and T. C. Merigan. A trial comparing nucleoside monotherapy with combination therapy in hiv-infected adults with cd4 cell counts from 200 to 500 per cubic millimeter. aids clinical trials group study 175 study team. *N Engl J Med*, 335(15):1081–90, 1996.

[68] Andreas H Diacon, Rodney Dawson, Florian von Groote-Bidlingmaier, Gregory Symons, Amour Venter, Peter R Donald, Christo van Niekerk, Daniel Everitt, Helen Winter, and Piet Becker. 14-day bactericidal activity of pa-824, bedaquiline, pyrazinamide, and moxifloxacin combinations: a randomised trial. *The Lancet*, 380(9846):986–993, 2012.

[69] Rafael Sanjun and Miguel R Nebot. A network model for the correlation between epistasis and genomic complexity. *PLoS One*, 3(7):e2663–e2663, 2008.

[70] MC Berenbaum. A method for testing for synergy with any number of agents. *Journal of Infectious Diseases*, 137(2):122–130, 1978.

[71] Anat Zimmer, Itay Katzir, Erez Dekel, Avraham E Mayo, and Uri Alon. Prediction of multidimensional drug dose responses based on measurements of drug pairs. *Proceedings of the National Academy of Sciences*, 113(37):10442–10447, 2016.

[72] Caitlin Mullan Crain, Kristy Kroeker, and Benjamin S Halpern. Interactive and cumulative effects of multiple human stressors in marine systems. *Ecology letters*, 11(12):1304–1315, 2008.

[73] Celia Y Chen, Kevin M Hathaway, Dean G Thompson, and Carol L Folt. Multiple stressor effects of herbicide, ph, and food on wetland zooplankton and a larval amphibian. *Ecotoxicology and environmental safety*, 71(1):209–218, 2008.

[74] Ian Billick and Ted J Case. Higher order interactions in ecological communities: what are they and how can they be detected? *Ecology*, 75(6):1529–1543, 1994.

[75] Suzanne Jane Welham, Salvador Alejandro Gezan, SJ Clark, and Andrew Mead. *Statistical methods in biology: Design and analysis of experiments and regression.* CRC Press, 2014.

[76] M. Kleiber. Body size and metabolic rate. *Physiological Reviews*, 27(4):511–541, 1947.

[77] J. H. Brown, J. F. Gillooly, A. P. Allen, V. M. Savage, and G. B. West. Toward a metabolic theory of ecology. *Ecol.*, 85(7):1771–1789, 2004.

[78] J. H. Brown and G. B. West, editors. *Scaling in Biology.* Oxford University Press, New York, 2000.

[79] G. B. West, J. H. Brown, and B. J. Enquist. A general model for the origin of allometric scaling laws in biology. *Science*, 276:122–126, 1997.

[80] Jayanth R Banavar, Todd J Cooke, Andrea Rinaldo, and Amos Maritan. Form, function, and evolution of living organisms. *Proceedings of the National Academy of Sciences*, 111(9):3332–3337, 2014.

[81] J. R. Banavar, A. Maritan, and A. Rinaldo. Size and form in efficient transportation networks. *Nature*, 399:130–132, 1999.

[82] Peter Sheridan Dodds. Optimal form of branching supply and collection networks. *Physical review letters*, 104(4):048702, 2010.

[83] Yunlong Huo and Ghassan S Kassab. Intraspecific scaling laws of vascular trees. *Journal of The Royal Society Interface*, 9(66):190–200, 2012.

[84] R. E. Horton. Erosional development of streams and their drainage basins: hydrophysical approach to quantitative morphology. *Geological Society of America Bulletin*, 56:275–370, 1945.

[85] A. N. Strahler. Quantitative analysis of watershed geomorphology. *Transactions of the American Geophysical Union*, 8:913–920, 1957.

[86] G. B. West, J. H. Brown, and B. J. Enquist. A general model for the structure and allometry of plant vascular systems. *Nature*, 400(6745):664–667, 1999.

[87] M. Zamir. *The Physics of Coronary Blood Flow.* Springer, New York, 2005.

[88] Y. C. Fung. *Biomechanics: Circulation.* Springer Verlag, New York, 1996.

[89] Cecil D Murray. The physiological principle of minimum work applied to the angle of branching of arteries. *The Journal of general physiology*, 9(6):835–841, 1926.

[90] A. Krogh. The rate of diffusion of gases through animal tissues, with some remarks on the coefficient of invasion. *Journal of Physiology*, 52(6):391–408, 1919.

[91] V. M. Savage, J. F. Gillooly, E. L. Charnov, J. H. Brown, and G. B. West. Effects of body size and temperature on population growth. *Am. Nat.*, 163(3):429–441, 2004.

[92] P. S. Dodds, D. H. Rothman, and J. S. Weitz. Re-examination of the “3/4-law” of metabolism. *J. Theor. Biol.*, 209:9–27, 2001.

[93] Andrew Clarke, Peter Rothery, and Nick JB Isaac. Scaling of basal metabolic rate with body mass and temperature in mammals. *Journal of Animal Ecology*, 79(3):610–619, 2010.

[94] Shigeta Mori, Keiko Yamaji, Atsushi Ishida, Stanislav G. Prokushkin, Oxana V. Masyagina, Akio Hagihara, A.T.M. Rafiqul Hoque, Rempei Suwa, Akira Osawa, Tomohiro Nishizono, Tatsushiro Ueda, Masaru Kinjo, Tsuyoshi Miyagi, Takuya Kajimoto, Takayoshi Koike, Yojiro Matsuura, Takeshi Toma, Olga A. Zyryanova, Anatoly P. Abaimov, Yoshio Awaya, Masatake G. Araki, Tatsuro Kawasaki, Yukihiro Chiba, and Marjnah Umari. Mixed-power scaling of whole-plant respiration from seedlings to giant trees. *Proceedings of the National Academy of Sciences*, 107(4):1447–1451, 2010.

[95] G. S. Kassab, K. Imoto, F. C. White, C. A. Rider, Y. C. Fung, and C. M. Bloor. Coronary arterial tree remodeling in right ventricular hypertrophy. *Am. J. Physiol.*, 265:H366–H375, 1993.

[96] M. Zamir and H. Chee. Segment analysis of human coronary arteries. *Journal of Vascular Research*, 24(1-2):7684, 1987.

[97] M. R. T. Yen, F. Y. Zhuang, Y. C. Fung, H. H. Ho, H. Tremer, and S. S. Sobin. Morphometry of the cats pulmonary arteries. *J. Biomech. Eng.*, 106:131–136, 1984.

[98] David Hunt and Van M Savage. Asymmetries arising from the space-filling nature of vascular networks. *Physical Review E*, 93(6), 2015.

[99] M. Zamir. On fractal properties of arterial trees. *J. Theor. Biol.*, 197(4):517–526, 1999.

[100] C. A. Price, O. Symonova, Y. Mileyko, T. Hilley, and J. S. Weitz. Leaf extraction and analysis framework graphical user interface: Segmenting and analyzing the structure of leaf veins and areoles. *Plant Physiology*, 155(1):236, 2011.

[101] Y. Mileyko, H. Edelsbrunner, C.A. Price, and J. S. Weitz. Hierarchical ordering of reticular networks. *PLoS One*, in press, 2012.

[102] C. Scoffoni, M. Rawls, A. McKown, H. Cochard, and L. Sack. Decline of leaf hydraulic conductance with leaf hydration: relationship to leaf size and venation architecture. *Plant Physiology*, 156:832–843, 2011.

[103] A. B. Brummer, V. M. Savage, and B. J. Enquist. A general model for metabolic scaling in self-similar asymmetric networks. *In review*, 2017.

[104] Napoleone Ferrara and Terri Davis-Smyth. The biology of vascular endothelial growth factor. *Endocrine Reviews*, 18(1):4–25, 1997.

[105] C. D. Murray. The physiological principle of minimum work. i. the vascular system and the cost of blood volume. *Proc. Natl. Acad. Sci.*, 12(3):207–214, 1926.

[106] M Zamir. Optimality principles in arterial branching. *Journal of Theoretical Biology*, 62(1):227–251, 1976.

[107] Rachel Carson. Silent spring, (2002). *Boston, MA: Houghton Mifflin*, 1962.

[108] L Kalan and GD Wright. Antibiotic adjuvants: multicomponent anti-infective strategies. *Expert Reviews in Molecular Medicine*, 13, 2011.

[109] Matthew A Cooper and David Shlaes. Fix the antibiotics pipeline. *Nature*, 472(7341):32–32, 2011.

[110] William R Greco, Gregory Bravo, and John C Parsons. The search for synergy: a critical review from a response surface perspective. *Pharmacological reviews*, 47(2):331–385, 1995.

[111] Ting-Chao Chou. Theoretical basis, experimental design, and computerized simulation of synergism and antagonism in drug combination studies. *Pharmacological reviews*, 58(3):621–681, 2006.

[112] Scott M Hammer, Kathleen E Squires, Michael D Hughes, Janet M Grimes, Lisa M Demeter, Judith S Currier, Joseph J Eron Jr, Judith E Feinberg, Henry H Balfour Jr, and Lawrence R Deyton. A controlled trial of two nucleoside analogues plus indinavir in persons with human immunodeficiency virus infection and cd4 cell counts of 200 per cubic millimeter or less. *New England Journal of Medicine*, 337(11):725–733, 1997.

[113] Jean-Baptiste Michel, Pamela J Yeh, Remy Chait, Robert C Moellering, and Roy Kishony. Drug interactions modulate the potential for evolution of resistance. *Proceedings of the National Academy of Sciences*, 105(39):14918–14923, 2008.

[114] Camilo Mora, Rebekka Metzger, Audrey Rollo, and Ransom A Myers. Experimental simulations about the effects of overexploitation and habitat fragmentation on populations facing environmental warming. *Proceedings of the Royal Society of London B: Biological Sciences*, 274(1613):1023–1028, 2007.

[115] Rebecca L Cramp, Stefanie Reid, Frank Seebacher, and Craig E Franklin. Synergistic interaction between uvb radiation and temperature increases susceptibility to parasitic infection in a fish. *Biology letters*, 10(9):20140449, 2014.

[116] CL Folt, CY Chen, MV Moore, and J Burnaford. Synergism and antagonism among multiple stressors. *Limnology and Oceanography*, 44(3):864–877, 1999.

[117] Karen A Ross, Jennifer E Taylor, Marilyn D Fox, and Barry J Fox. Interaction of multiple disturbances: importance of disturbance interval in the effects of fire on rehabilitating mined areas. *Austral Ecology*, 29(5):508–529, 2004.

[118] Michael R Christensen, Mark D Graham, Rolf D Vinebrooke, David L Findlay, Michael J Paterson, and Michael A Turner. Multiple anthropogenic stressors cause ecological surprises in boreal lakes. *Global Change Biology*, 12(12):2316–2322, 2006.

[119] Rick A Relyea. Predator cues and pesticides: a double dose of danger for amphibians. *Ecological Applications*, 13(6):1515–1521, 2003.

[120] Michelle D Boone, Raymond D Semlitsch, Edward E Little, and Meaghan C Doyle. Multiple stressors in amphibian communities: effects of chemical contamination, bullfrogs, and fish. *Ecological Applications*, 17(1):291–301, 2007.

[121] Andrea Dávalos, Victoria Nuzzo, and Bernd Blossey. Demographic responses of rare forest plants to multiple stressors: the role of deer, invasive species and nutrients. *Journal of Ecology*, 102(5):1222–1233, 2014.

[122] Margaret R Metz, J Morgan Varner, Kerri M Frangioso, Ross K Meentemeyer, and David M Rizzo. Unexpected redwood mortality from synergies between wildfire and an emerging infectious disease. *Ecology*, 94(10):2152–2159, 2013.

[123] Robert M Pringle, Duncan M Kimuyu, Ryan L Sensenig, Todd M Palmer, Corinna Riginos, Kari E Veblen, and Truman P Young. Synergistic effects of fire and elephants on arboreal animals in an african savanna. *Journal of Animal Ecology*, 84(6):1637–1645, 2015.

[124] Poppy Lakeman-Fraser and Robert M Ewers. Untangling interactions: do temperature and habitat fragmentation gradients simultaneously impact biotic relationships? *Proceedings of the Royal Society of London B: Biological Sciences*, 281(1787):20140687, 2014.

[125] Nick T Shears and Philip M Ross. Toxic cascades: multiple anthropogenic stressors have complex and unanticipated interactive effects on temperate reefs. *Ecology letters*, 13(9):1149–1159, 2010.

[126] Rebecca A Gooding, Christopher DG Harley, and Emily Tang. Elevated water temperature and carbon dioxide concentration increase the growth of a keystone echinoderm. *Proceedings of the National Academy of Sciences*, 106(23):9316–9321, 2009.

[127] Emily S Darling and Isabelle M Côté. Quantifying the evidence for ecological synergies. *Ecology letters*, 11(12):1278–1286, 2008.

[128] Anne M Treasure and Steven L Chown. Antagonistic effects of biological invasion and temperature change on body size of island ectotherms. *Diversity and Distributions*, 20(2):202–213, 2014.

[129] Sacha M O'Regan, Wendy J Palen, and Sean C Anderson. Climate warming mediates negative impacts of rapid pond drying for three amphibian species. *Ecology*, 95(4):845–855, 2014.

[130] Jennifer J Vowels and James H Thomas. Genetic analysis of chemosensory control of dauer formation in caenorhabditis elegans. *Genetics*, 130(1):105–123, 1992.

[131] Shoshanna Gottlieb and Gary Ruvkun. daf-2, daf-16 and daf-23: genetically interacting genes controlling dauer formation in caenorhabditis elegans. *Genetics*, 137(1):107–120, 1994.

[132] Marco Gagiano, Dewald Van Dyk, Florian F Bauer, Marius G Lambrechts, and Isak S Pretorius. Msn1p/mss10p, mss11p and muc1p/flo11p are part of a signal transduction pathway downstream of mep2p regulating invasive growth and pseudohyphal differentiation in saccharomyces cerevisiae. *Molecular microbiology*, 31(1):103–116, 1999.

[133] Lei Dai, Kirill S Korolev, and Jeff Gore. Slower recovery in space before collapse of connected populations. *Nature*, 496(7445):355–358, 2013.

[134] Kirill A Datsenko and Barry L Wanner. One-step inactivation of chromosomal genes in escherichia coli k-12 using pcr products. *Proceedings of the National Academy of Sciences*, 97(12):6640–6645, 2000.

[135] Tomoya Baba, Takeshi Ara, Miki Hasegawa, Yuki Takai, Yoshiko Okumura, Miki Baba, Kirill A Datsenko, Masaru Tomita, Barry L Wanner, and Hirotada Mori. Construction of escherichia coli k12 inframe, singlegene knockout mutants: the keio collection. *Molecular systems biology*, 2(1), 2006.

[136] Geoffrey M Scott and May S Kyi. *Handbook Essential Antibiotics.* CRC Press, 2001.

[137] JN Darroch. Multiplicative and additive interaction in contingency tables. *Biometrika*, 61(1):207–214, 1974.

[138] Pieter M Kroonenberg and Carolyn J Anderson. Additive and multiplicative models for three-way contingency tables: Darroch (1974) revisited. *Multiple correspondence analysis and related methods*, pages 455–486, 2006.

[139] Frank C Odds. Synergy, antagonism, and what the chequerboard puts between them. *Journal of Antimicrobial Chemotherapy*, 52(1):1–1, 2003.

[140] Vanessa M D'Costa, Katherine M McGrann, Donald W Hughes, and Gerard D Wright. Sampling the antibiotic resistome. *Science*, 311(5759):374–377, 2006.

[141] Fiona Walsh and Brion Duffy. The culturable soil antibiotic resistome: a community of multi-drug resistant bacteria. *PLoS One*, 8(6):e65567, 2013.

[142] Guozhi Yu, Desiree Y Baeder, Roland R Regoes, and Jens Rolff. Combination effects of antimicrobial peptides. *Antimicrobial agents and chemotherapy*, 60(3):1717–1724, 2016.

[143] Martijs J Jonker, Claus Svendsen, Jacques JM Bedaux, Marina Bongers, and Jan E Kammenga. Significance testing of synergistic/antagonistic, dose level-dependent, or dose ratio-dependent effects in mixture dose-response analysis. *Environmental toxicology and chemistry*, 24(10):2701–2713, 2005.

[144] Lauge Sokol-Hessner and Oswald J Schmitz. Aggregate effects of multiple predator species on a shared prey. *Ecology*, 83(9):2367–2372, 2002.

[145] MS Gunzburger and J Travis. Effects of multiple predator species on green treefrog (hyla cinerea) tadpoles. *Canadian journal of zoology*, 83(7):996–1002, 2005.

[146] Thijs Christiaan Son and Martin Thiel. Multiple predator effects in an intertidal food web. *Journal of Animal Ecology*, 75(1):25–32, 2006.

[147] Michael W McCoy, Adrian C Stier, and Craig W Osenberg. Emergent effects of multiple predators on prey survival: the importance of depletion and the functional response. *Ecology letters*, 15(12):1449–1456, 2012.

[148] Hongyan Cheng, Nan Yao, Zi-Gang Huang, Junpyo Park, Younghae Do, and Ying-Cheng Lai. Mesoscopic interactions and species coexistence in evolutionary game dynamics of cyclic competitions. *Scientific reports*, 4, 2014.

[149] Alan Stuart, Maurice G Kendall, et al. The advanced theory of statistics. *Charles Griffin*, 1968.

[150] James Glimm and Arthur Jaffe. Quantum physics: a functional integral point of view. *Springer Science & Business Media*, 2012.

[151] Daniel A Soluk and Nicholas C Collins. Synergistic interactions between fish and stoneflies: facilitation and interference among stream predators. *Oikos*, pages 94–100, 1988.

[152] Razan Hamoud, Stefan Zimmermann, Jrgen Reichling, and Michael Wink. Synergistic interactions in two-drug and three-drug combinations (thymol, edta and vancomycin) against multi drug resistant bacteria including e. coli. *Phytomedicine*, 21(4):443–447, 2014.

[153] Carmel J Cohen, Howard W Bruckner, Gunter Deppe, John A Blessing, Howard Homesley, James H Lee, and Watson Watring. Multidrug treatment of advanced and recurrent endometrial carcinoma: a gynecologic oncology group study. *Obstetrics & Gynecology*, 63(5):719–726, 1984.

[154] Jonathan B Fitzgerald, Birgit Schoeberl, Ulrik B Nielsen, and Peter K Sorger. Systems biology and combination therapy in the quest for clinical efficacy. *Nature chemical biology*, 2(9):458–466, 2006.

[155] Christopher Walsh. Molecular mechanisms that confer antibacterial drug resistance. *Nature*, 406(6797):775–781, 2000.

[156] Carl Nathan. Antibiotics at the crossroads. *Nature*, 431(7011):899–902, 2004.

[157] Curtis T Keith, Alexis A Borisy, and Brent R Stockwell. Multicomponent therapeutics for networked systems. *Nature Reviews Drug Discovery*, 4(1):71–78, 2005.

[158] Thomas R. Fraser. Lecture on the antagonism between the actions of active substances. *British Medical Journal*, 2(618):485–487, 1872.

[159] Anna L Tyler, Folkert W Asselbergs, Scott M Williams, and Jason H Moore. Shadows of complexity: what biological networks reveal about epistasis and pleiotropy. *Bioessays*, 31(2):220–227, 2009.

[160] Daniel A Soluk. Multiple predator effects: predicting combined functional response of stream fish and invertebrate predators. *Ecology*, pages 219–225, 1993.

[161] Alice Zhou, Tina Manzhu Kang, Jessica Yuan, Casey Beppler, Caroline Nguyen, Zhiyuan Mao, Minh Quan Nguyen, Pamela Yeh, and Jeffrey H Miller. Synergistic interactions of vancomycin with different antibiotics against escherichia coli: Trimethoprim and nitrofurantoin display strong synergies with vancomycin against wild-type e. coli. *Antimicrobial agents and chemotherapy*, 59(1):276–281, 2015.

[162] Viktria Lzr, Gajinder Pal Singh, Rka Spohn, Istvn Nagy, Balzs Horvth, Mnika Hrtyan, Rbert BusaFekete, Balzs Bogos, Orsolya Mhi, and Blint Csrg. Bacterial evolution of antibiotic hypersensitivity. *Molecular systems biology*, 9(1):700, 2013.

[163] Paolo S Ocampo, Viktria Lzr, Balzs Papp, Markus Arnoldini, Pia Abel zur Wiesch, Rbert Busa-Fekete, Gergely Fekete, Csaba Pl, Martin Ackermann, and Sebastian Bonhoeffer. Antagonism between bacteriostatic and bactericidal antibiotics is prevalent. *Antimicrobial agents and chemotherapy*, 58(8):4573–4582, 2014.

[164] Chintan Jagdishchandra Joshi and Ashok Prasad. Epistatic interactions among metabolic genes depend upon environmental conditions. *Molecular BioSystems*, 10(10):2578–2589, 2014.

[165] Florian Klein, Ariel Halper-Stromberg, Joshua A Horwitz, Henning Gruell, Johannes F Scheid, Stylianos Bournazos, Hugo Mouquet, Linda A Spatz, Ron Diskin, and Alexander Abadir. Hiv therapy by a combination of broadly neutralizing antibodies in humanized mice. *Nature*, 492(7427):118–122, 2012.

[166] John A Bartlett, Michael J Fath, Ralph Demasi, Ashwaq Hermes, Joseph Quinn, Elsa Mondou, and Franck Rousseau. An updated systematic overview of triple combination therapy in antiretroviral-naive hiv-infected adults. *Aids*, 20(16):2051–2064, 2006.

[167] Roy M Gulick, Heather J Ribaudo, Cecilia M Shikuma, Stephanie Lustgarten, Kathleen E Squires, William A Meyer III, Edward P Acosta, Bruce R Schackman, Christopher D Pilcher, and Robert L Murphy. Triple-nucleoside regimens versus efavirenz-containing regimens for the initial treatment of hiv-1 infection. *New England Journal of Medicine*, 350(18):1850–1861, 2004.

[168] Pablo Barreiro, Vincent Soriano, Francisco Blanco, Csar Casimiro, Juan Jos de la Cruz, and Juan Gonzlez-Lahoz. Risks and benefits of replacing protease inhibitors by nevirapine in hiv-infected subjects under long-term successful triple combination therapy. *Aids*, 14(7):807–812, 2000.

[169] Joseph Peter Torella, Remy Chait, and Roy Kishony. Optimal drug synergy in antimicrobial treatments. *PLoS Comput Biol*, 6(6):e1000796, 2010.

[170] Hyejin Youn, Michael T Gastner, and Hawoong Jeong. Price of anarchy in transportation networks: efficiency and optimality control. *Physical review letters*, 101(12):128701, 2008.

[171] V. M. Savage, A. P. Allen, J. F. Gillooly, A. B. Herman, J. H. Brown, and G. B. West. Scaling of number, size, and metabolic rate of cells with body size in mammals. *Proc. Natl. Acad. Sci.*, 104(11):4718–4723, 2007.

[172] M. Kleiber. *The Fire of Life: An Introduction to Animal Energetics.* Wiley, New York, 1961.

[173] Charles A Price, Joshua S Weitz, Van M Savage, James Stegen, Andrew Clarke, David A Coomes, Peter S Dodds, Rampal S Etienne, Andrew J Kerkhoff, and Katherine McCulloh. Testing the metabolic theory of ecology. *Ecology Letters*, 15(12):1465–1474, 2012.

[174] M.F. Schroeder. *Fractals, chaos, power laws.* W.H. Freeman and Company, New York, 1991.

[175] E.I. Allmen, J.S. Sperry, D.D. Smith, V.M. Savage, B.J. Enquist, P.B. Reich, and L.P. Bentley. A species-level model for metabolic scaling of trees ii. testing in a ring- and diffuse-porous species. *Functional Ecology*, pages doi: 10.1111/j.1365–2435.2012.02021.x, 2012.

[176] M. Zamir. Vascular system of the human heart: some branching and scaling issues. In *Scaling in Biology*, page 129143. Oxford University Press, USA, 2000.

[177] C. G. Caro, T. J. Pedley, R. C. Schroter, and W. A. Seed. *The Mechanics of Circulation.* Oxford University Press, Oxford, UK, 1978.

[178] Ghada Kalsho and Ghassan S Kassab. Bifurcation asymmetry of the porcine coronary vasculature and its implications on coronary flow heterogeneity. *American Journal of Physiology-Heart and Circulatory Physiology*, 287(6):H2493–H2500, 2004.

[179] C Guiot, T Todros, PG Piant, A Sciarrone, G Kosanke, and P Kaufmann. The diameter distribution of the stem villi arteries does not discriminate between normal and intra uterine growth restricted placentas. *Computational and Mathematical Methods in Medicine*, 1(4):263–273, 1999.

[180] Peter A. Galie, Duc-Huy T. Nguyen, Colin K. Choi, Daniel M. Cohen, Paul A. Janmey, and Christopher S. Chen. Fluid shear stress threshold regulates angiogenic sprouting. *Proceedings of the National Academy of Sciences*, 111(22):7968–7973, 2014.

[181] Sarah L. Tressel, Ruo-Pan Huang, Nicholas Tomsen, and Hanjoong Jo. Laminar shear inhibits tubule formation and migration of endothelial cells by an angiopoietin-2dependent mechanism. *Arteriosclerosis, thrombosis, and vascular biology*, 27(10):2150–2156, 2007.

[182] M Zamir. Nonsymmetrical bifurcations in arterial branching. *The Journal of general physiology*, 72(6):837–845, 1978.

[183] John A Adam. Blood vessel branching: beyond the standard calculus problem. *Mathematics Magazine*, 84(3):196–207, 2011.

[184] Yucheng Yao, Medet Jumabay, Anthony Wang, and Kristina I Bostrm. Matrix gla protein deficiency causes arteriovenous malformations in mice. *The Journal of clinical investigation*, 121(8):2993–3004, 2011.

[185] Irwin Greenberg and Raymond A Robertello. The three factory problem. *Mathematics Magazine*, 38(2):67–72, 1965.

[186] WJ Van de Lindt. A geometrical solution of the three factory problem. *Mathematics Magazine*, 39(3):162–165, 1966.

[187] Yujin Shen and Juan Tolosa. The weighted fermat triangle problem. *International Journal of Mathematics and Mathematical Sciences*, 2008, 2008.

[188] Y. C. Fung. *Biodynamics.* Springer Verlag, New York, 1984.

[189] Y. C. Fung. *Biomechanics: Motion, Flow, Stress, and Growth.* Springer-Verlag, New York, 1990.

[190] Jack Ritter. An efficient bounding sphere. *Academic Press Professional, Inc.*, pages 301–303, 1990.

[191] M. Zamir, S. M. Wrigley, and B. L. Langille. Arterial bifurcations in the cardiovascular system of a rat. *J. Gen. Physiol.*, 81:325–335, 1983.

[192] Yina Guo, TingHsuan Chen, Xingjuan Zeng, David Warburton, Kristina I Bostrm, ChihMing Ho, Xin Zhao, and Alan Garfinkel. Branching patterns emerge in a mathematical model of the dynamics of lung development. *The Journal of physiology*, 592(2):313–324, 2014.

[193] R. J. Metzger, O. D. Klein, G. R. Martin, and M. A. Krasnow. The branching programme of mouse lung development. *Nature*, 453:745–751, 2008.

[194] Aleks Jakulin and Ivan Bratko. Testing the significance of attribute interactions. In *Proceedings of the twenty-first international conference on Machine learning*, page 52. ACM, 2004.

[195] Lus M. A. Bettencourt, Joe Hand, and Jos Lobo. Spatial selection and the statitistics of neighborhoods. *Santa Fe Institute Working Papers*, 2015.

[196] Marc Durand. Architecture of optimal transport networks. *Physical Review E*, 73(1):016116, 2006.

[197] R. Glenny, S. Bernard, B. Neradilek, and N. Polissar. Quantifying the genetic influence on mammalian vascular tree structure. *Proc. Natl. Acad. Sci. USA*, 104(16):6858–6863, 2007.

[198] Joseph Travis, W Hubert Keen, and John Juilianna. The effects of multiple factors on viability selection in hyla gratiosa tadpoles. *Evolution*, pages 1087–1099, 1985.

[199] Jessica Gurevitch, Janet A Morrison, and Larry V Hedges. The interaction between competition and predation: a meta-analysis of field experiments. *The American Naturalist*, 155(4):435–453, 2000.